UNIVERSITY OF OKLAHOMA

GRADUATE COLLEGE

A SUPERVISED MACHINE LEARNING APPROACH TO DISCRIMINATE RESERVOIR FLUID PRESENCE AND SATURATION IN THE GULF OF MEXICO USING FREQUENCY AND SPECTRAL SHAPE ATTRIBUTES

A THESIS

SUBMITTED TO THE GRADUATE FACULTY

in partial fulfillment of the requirements for the

Degree of

MASTER OF SCIENCE

By

Mario Ricardo Ballinas Rondón

Norman, Oklahoma

2023

A SUPERVISED MACHINE LEARNING APPROACH TO DISCRIMINATE RESERVOIR FLUID PRESENCE AND SATURATION IN THE GULF OF MEXICO USING FREQUENCY AND SPECTRAL SHAPE ATTRIBUTES

A THESIS APPROVED FOR THE

SCHOOL OF GEOSCIENCES

BY THE COMMITTEE CONSISTING OF

Dr. Heather Bedle, Chair

Dr. Matthew J. Pranter

Dr. Deepak Devegowda

To Mom & Dad, My Sister, and My Love

For helping me get this far, and more

ACKNOWLEDGEMENTS

I would like to start by expressing my biggest thanks to my mom Osglayt, dad Mario, and sister Mariana for their unwavering love and support throughout my academic journey. Their encouragement and motivation have been instrumental in my success, and I couldn't have done it without them. I would also like to thank Audrey Schmitt for her love, patience, and hours she spent proofreading my thesis. Her support and understanding have been invaluable during this time.

I am also deeply grateful to my advisor Dr. Heather Bedle for believing in me and giving me the opportunity to be a part of her program. Her guidance and encouragement have helped me stay on track and remain focused, even during the most challenging times. I would like to thank Dr. Deepak Devegowda for helping me shape my thesis project and taking my Python coding and machine learning skills to the next level. Additionally, I want to thank Dr. Matthew J. Pranter for sharing his wealth of geological knowledge and teaching me new tricks in Petrel that I use every day.

I would also like to express my appreciation to the friends I have made at this university, for their camaraderie and support during this stressful time. Special thanks to Marcus Maas, Karelia La Marca, Emily Jackson, David Lubo-Robles, Laura Ortiz, Bobby Buist, Diana Salazar, Jacob Clements, Pamela Blanco, Raymond Ng, Grace Barber, Vanesa Rios Perez, John Mcknight, Patience Emuobosa, Alex Vera and Britney Stroud. Their assistance and insights have helped me to make my research more impactful and meaningful. I am grateful for their friendship and the joy they have brought to my life.

Furthermore, I want to extend a special thank you to my mentor Mr. Allen Bertagne for taking me on after my bachelor's graduation and igniting my passion for seismic interpretation and

geophysics. Without his teachings, I would not be where I am today. A special thanks also goes to my second mentor Carlos Eduardo Moreno Elcure, who provided me unvaluable knowledge during my internship with Lumina Geophysical. Both of these professionals believed in me before I knew that seismic amplitudes had polarities and frequencies. Jesus Nevarez, although my peer, deserve a big thanks for reaffirming geophysical principles that I did not have the courage to ask my mentors about again.

Finally, I would like to thank the American Chemical Society Petroleum Research Fund for providing the funding that made my graduate research possible. Their support has been integral to my success, and I am deeply grateful for their generosity.

In conclusion, I would like to thank everyone who has played a part in my academic journey. Your support, encouragement, and guidance have been invaluable, and I am deeply grateful for everything you have done for me

TABLE OF CONTENTS

Key words: gas saturation, Gulf of Mexico, frequency attributes, spectral decomposition, machine learning

THESIS ABSTRACT

The first chapter in this research aims to define reliable attributes to differentiate subsurface fluids and measure their attenuation to provide insights into reservoir properties. The study investigates the effects of fluids and saturations on seismic data by analyzing a frequency-related suite of attributes using post-stack seismic field data from stacked reservoirs in Ursa Well #1 in the Gulf of Mexico. The results show that high attenuation reduces higher frequencies, resulting in a spectrum skewed towards lower frequencies with high kurtosis and low roughness, slope, and bandwidth. The attribute analysis presents that low amounts of gas saturation exhibit more attenuation than a fully saturated gas reservoir. Chapter 1 highlights the importance of spectral analysis, especially the spectrum's shape, in interpreting gas saturation and attenuation effects on post-stack seismic data allowing successful discrimination of water, oil, and high or low gas saturations.

Furthermore, the second chapter presents a new workflow that applies supervised machine learning algorithms to predict the presence of hydrocarbon fluids and their economic viability using the frequency suite of seismic attributes. K-nearest neighbors, decision tree and random forest algorithms are tested on datasets for their robustness in classifying the fluid types. The SHAP values analysis is used to gather information on the importance of each attribute for the classification of each fluid class. The machine learning models are trained with the Ursa dataset and subsequentially predict in an expanded area around the training well. The King Kong and Lisa Anne fields, belonging to a different seismic survey, are used as a validation test for the machine learning models.

The study concludes that the machine learning models, using the frequency suite of attributes, can predict water, oil, and high or low gas saturations within clastic reservoirs of the Miocene Gulf of Mexico. The decision tree and random forest models correctly predicted the fluid class in three out of four King Kong and Lisa Anne Field wells. The model predictions in the Ursa blind test expressed reliability in the models after observation of flat spots with correct density stacking orders. The promising results convey that using supervised machine learning algorithms for reservoir fluid identification and gas saturation predictions can revolutionize the field of hydrocarbon exploration and production by providing a more robust way to risk prospects using exclusively post-stack seismic data and frequency attributes.

CHAPTER 1: ANALYSIS OF SPECTRAL SHAPE AND DISCRETE FREQUENCY MAGNITUDE ATTRIBUTES FOR THE DISCRIMINATION OF RESERVOIR FLUID PRESENCE AND SATURATION

ABSTRACT

Researchers have used seismic reflection data and theoretical models to differentiate the effects of high and low gas saturation reservoirs, but no practical method has consistently achieved reliable results. The study analyzes the fluid and saturation effects on a frequency-related suite of attributes, including independent frequency magnitudes and spectral shape attributes. The attributes statistically measure the entire frequency waveform and allow interpretation of the attenuation produced by variable gas saturations, oil, and water presence in reservoirs. Ursa Well #1 presents an opportunity to study these changes in attribute responses since it contains multiple stacked reservoirs with similar geological properties but different fluids and saturations.

The Ursa deepwater field is located in the Mississippi Canyon protraction and consists of amalgamated channels and sheet sands of Pliocene to Miocene age. Each of the well's reservoirs are characterized by a single fluid class which comprises gas at low and high saturations, oil, and water. A shale section was added as a fifth fluid class to analyze the frequency responses of non-reservoir areas. A data frame is created of all the voxels in each reservoir and their fluid class. This study analyzes the range of frequency attribute values in the presence of each fluid class. The goal is to define reliable attributes to differentiate the fluid classes and measure their attenuation.

The results show that high attenuation reduces higher frequencies, resulting in a spectrum skewed towards lower frequencies with high kurtosis and low roughness, slope, and bandwidth. The water and non-reservoir fluid classes exhibit the lowest attenuation, while the oil class exhibits a range of values that make it difficult to interpret. The analysis of the spectral shape attributes

indicates that low gas saturation has higher attenuation than high gas saturation, consistent with previous theoretical models. However, the attenuation relationship of varying gas saturation in reservoirs is more complex, as evidenced by low gas saturation exhibiting consistently higher magnitudes of all frequencies despite high gas saturation having higher mean and average frequencies.

The findings of this study highlight the importance of spectral analysis in interpreting gas saturation and attenuation effects on seismic data. The observed relationships between different fluid classes and their spectral attributes can help define attenuation and provide insights into reservoir properties. The thorough analysis of all the frequency attributes indicates that successful discrimination of the five fluid classes is possible, despite being limited to post-stack seismic attributes.

INTRODUCTION

Many traditional hydrocarbon prospects are drilled based on the observation of 'bright spots' or high amplitudes in seismic data. However, bright spot identification does not guarantee economic success, as low gas saturations (1%-15% gas-to-water ratio) also results in seismic bright spots. Researchers have used seismic reflection data and theoretical models to improve methods for the differentiation and discrimination of the seismic effects of low gas saturation (LGS) and high gas saturation (HGS) reservoirs. However, no practical method has consistently achieved reliable results to aid in reliable risk assessment of identifying bright spots related to uneconomic low gas saturations.

To date, minimal research has been performed in characterizing seismic attribute relationships to varying gas saturations outside of the creation of synthetic fluid substitution models. One reason this issue remains unsolved is that many LGS reservoirs are officially reported as dry holes due to their uneconomical success, reducing the public knowledge of their locations and exact reasons why they were considered uneconomic. A second reason is that where such LGS reservoirs exist, a fully saturated gas reservoir with similar geological properties is missing from the same seismic survey, which does not allow for the analysis and comparison of LGS to more fully saturated gas reservoirs in the same seismic dataset. The Ursa Well #1 in the Gulf of Mexico does not have either of these issues, and presents an opportunity to more fully study gas saturation changes with the aid of seismic attribute responses.

As the Ursa Well #1 contains multiple stacked reservoirs with similar geological properties but different fluids and saturations, this research utilizes the well and seismic data to understand the effects of LGS, HGS, and oil reservoirs in the seismic frequency spectrum. The analysis also includes observations of a water reservoir and non-reservoir (shale) in contrast with the hydrocarbon-bearing reservoirs. Limitations include post-stack seismic data, meaning that no amplitude versus offset (AVO) attributes will be analyzed in this study due to a lack of available angle stack data. Additionally, the fluid and saturation effects on a frequency-related suite of attributes are investigated, resulting in an attribute suite that includes independent frequency magnitudes and spectral shape attributes that statistically measure the entire frequency waveform. While previous theoretical models have presented that attenuation effects are perceived at discrete frequencies of near-angle stacks (Jin et al., 2017), the benefits of the spectral shape attributes for fluid characterization have not been previously fully utilized. The attribute analysis results of this

study suggest that post-stack seismic data can achieve similar results at discriminating fluids and saturations after analyzing the frequency attributes' values from the Ursa reservoirs.

Previous work

Many studies on the effects of LGS reservoirs focus on post-drilling investigations using the acquired well data. Sonic and density logs are used in these cases to prove the existence of LGS in the reservoir by observing the decrease in p-wave velocities that produced the uneconomical bright spots (O'Brien, 2004). The same study used amplitude ratios of background/reservoir and on-prospect/off-prospect between high and low gas reservoirs to quantify the amplitude anomalies. O'Brien's results indicated that the amplitude ratios were nearly identical despite the difference in gas saturation. O'Brien's study suggests that seismic amplitude data cannot be used to ensure gas saturations. Using well logs to confirm the saturations is impractical because they are acquired after the significant economic investment of drilling the well.

An effort is made to rely on seismic data alone to avoid drilling uneconomical wells. Researchers have continued to use more complex amplitude interpretation methods to characterize fluids and saturations better. The current standard method used for hydrocarbon detection is the AVO technique which takes advantage of the elastic properties effects of the gas. This method lets the interpreter observe amplitude variations in potential reservoirs with varying reflection angles, indicating reservoir fluid type and saturation. Unfortunately, AVO interpretations are not foolproof and can still lead to the drilling of non-economical gas reservoirs (Zhang and Hilterman, 2007). This lack of effective methodologies has led researchers to develop various synthetic models and techniques to test consistent methods to estimate reservoir gas saturations.

One theoretical model based on seismic attenuation, the energy loss of the seismic waves due to the elastic properties of the reservoir, has been found to show distinct differences with varying amounts of gas saturation (Wu et al., 2014). Wu's model point to the highest attenuation occurring at 20% gas saturation, which can be classified as LGS. The attenuation can be measured by analyzing the spectral shape of the frequency spectrum. Analyzing the independent frequency magnitudes at various reflection angles has shown a relationship that distinguishes gas saturations (Jin et al., 2017). Despite the promising results of Jin's and Wu's models, their reliability has not been extensively tested with field data. The pre-stack data required to apply Wu's and Jin's methods are not commonly available in areas with known LGS reservoirs. Despite that, this study uses their findings to analyze post-stack frequency attributes and observe their responses to varying gas saturations, among other fluid classes, within the Ursa reservoirs.

Geologic Setting

The Gulf of Mexico (Figure 1-1) is a large prolific oil and gas basin covering 600,000 square miles. It borders Florida, Alabama, Mississippi, Louisiana, and Texas to the north and Mexico to the west and south. It began forming around 200 million years ago in the Late Triassic Period when the North American plate started drifting apart from the South American and African plates (Elshahawi, 2014). Subsequent north-south rifting in the Middle Jurassic allowed seawater to fill the basin from the east, precipitating the Louann Salt (Elshahawi, 2014).

Galloway (2008) reports that the North American portion of the Gulf of Mexico had a large sediment influx from the Late Jurassic to Early Cretaceous, followed by a mix of clastic and carbonate aggradation up to the Late Cretaceous. The stretching and cooling of the crust allowed for a starved basin that subsided faster relative to the sediment supplied at the coast. The

sedimentary loading through the Late Mesozoic caused much of the Louann Salt to mobilize and form canopies and stocks throughout much of the basin; most of the salt is now allochthonous. The central crust of the Gulf of Mexico now sits 10 to 20 km below sea level. It has allowed for resurgent clastic deposition in the form of turbidites and sheets sands to deposit in stages, mainly in the north-west basin during the Paleogene and in the central and north-east basin in the Neogene. Today, the United States portion of the Gulf of Mexico can have around 60,000 feet thick strata in the deep ocean.

The geologic and tectonic history of the North American Gulf of Mexico basin has made it one of the world's longest produced and proliferous oil and gas basins (Elshahawi, 2014). The extreme subduction-related temperatures allowed the carbon-rich Middle to Late Mesozoic sands, shales, and carbonate platforms to become rich source rocks across the basin. The highly porous Cenozoic clastic sequences have proven to be great reservoirs with excellent mud/shale seals. Much of the Cenozoic sheet sands and turbidites were deposited along mini basins formed along the edges of the allochthonous salt. The salt edges serve as structural traps and seals for the hydrocarbons. Extensive fault systems formed due to the large-scale subsidence, a ridged basement, and extreme salt movement serve as the primary migration pathway connecting the gulf's petroleum system.

Nearly 100 years of production of more than 22 billion barrels of oil and 190 trillion tons of gas (BOEM, 2019) across the basin (Figure 1-1) has allowed for continued exploration interest with newer seismic technologies. Much of the exploration from the 1960s onwards was driven by using bright spots as direct hydrocarbon indicators (DHI) (Galloway, 2008). Exploration moved into the Gulf of Mexico's deepwater at the onset of 3D seismic acquisition in the late 1970s (Elshahawi,2014). In the 1980s, anomalous amplitudes were being studied based on how their

values changed in relation to source and receiver offset (Galloway, 2008). One problem of DHIs is that they only indicate the possible presence of hydrocarbons, and can often be caused by other factors, such as lower saturation gas, which creates an inherent risk for energy companies.

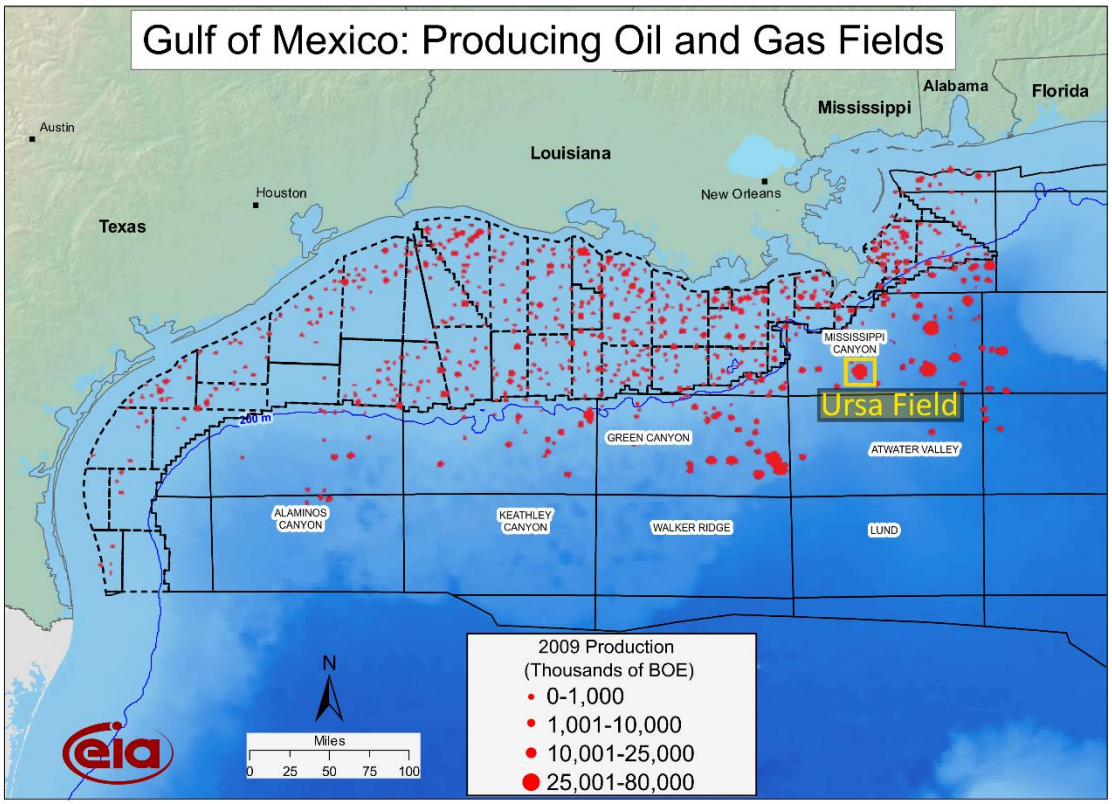

Source: Energy Information Administration based on data from MMS, HPDI, CA Dept of Oil , Gas & Geothermal
Updated: April 8, 2009

Figure 1-1: Gulf of Mexico cumulative production map. The yellow box indicates the location of the Ursa Field. Modified from U.S Energy Information Administration and Elshahawi, 2014.

The Ursa deepwater field is located 130 miles south of New Orleans in the Mississippi Canyon protraction area Block 809 (Figure 1-1). Shell, BP, Conoco, and Exxon currently own the lease in this area. The Ursa Field is in the same deepwater salt-bounded mini-basin as Shell's and BP's Mars discovery. The reservoirs are amalgamated channels and sheets sands of Pliocene to Miocene age with an average of 25% porosity (Batzle, 2006). The hydrocarbon reservoirs are

separated into two intervals around 12,000 feet and 18,500 feet subsea depth and occur at salt-bounded three-way anticlinal structures (Hilterman, 2001). The vertical Ursa #1 well, was selected as the investigation site due to the lithological similarities between reservoirs, differing only in the fluids present. Each reservoir contains one fluid, which includes gas in low and high saturations, oil, and water. AVO research on a 2D seismic line performed by Hilterman in 2001, along with production history, proved the presence of the fluids within each reservoir. Figure 1-2 shows the synthetic seismic trace from Hilterman overlain over inline 2844 from a newer 3D acquisition.

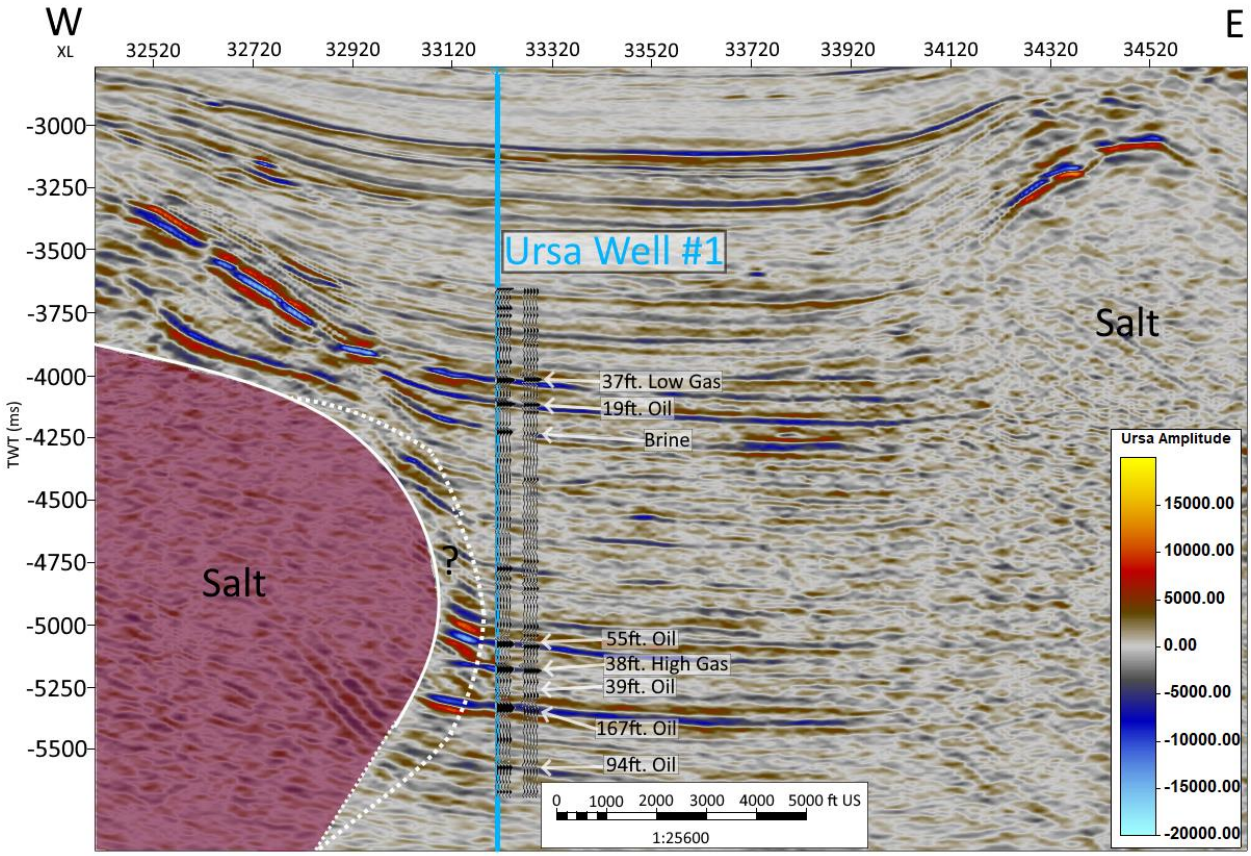

Figure 1-2: Inline 2844 of the Ursa Seismic Survey highlights the sequence of hydrocarbon-filled reservoirs interpreted from the synthetic seismic and AVO study by Hilterman,2001. The purple polygon highlights the known extent of the salt body, while the dashed line represents its uncertain extent.

DATA

The Ursa Well #1 includes data such as the top and bottom hole locations, deviation surveys, checkshots, production history, and a complete suite of logs; producing intervals contained digital logs, while uneconomical intervals contained raster logs. The density and chromatograph analysis logs were used to prove the presence of hydrocarbons. In addition, the Enverus final well reports and production history were used to confirm the lack of economic saturation in one reservoir of Ursa Well #1.

The G3D1304-002 3D full-stack seismic data set collected in 1988 encompasses the Ursa Field. It covers approximately 420 square miles (1089 km^2) of the Mississippi Canyon protraction area. It is SEG positive polarity and has a bin spacing of 100 ft by 100 ft with a sampling rate of 4 ms. This data cube representing 100 ft^2 of aerial extent and 4 ms of depth is defined as one voxel for the Ursa dataset. The voxel represents the location in the seismic volume and has one value for every attribute.

METHODS

This research analyses the reservoirs' frequency-related attribute values in the presence of each fluid class. The fluid classes that are analyzed are LGS, HGS, Oil, Water, and Non-Reservoir. The area of investigation is limited to 14 lines and 9 crossline centered around the Ursa well, keeping the reservoirs' depth change to a minimum. The limited area avoids the salt dome to the west while ensuring the presence of only one fluid per reservoir interval, reducing uncertainty that would result if seismic is analyzed too far away from the well, as extending the area of investigation could include fluids not observed by the well logs.

The frequency suite of attributes is created for the cropped seismic volume. The fluids in each reservoir along the well path are interpreted from the available well log data and previous research. The top and base of each reservoir are mapped along with a 100 ms thick shale section. A discrete volume is created that groups all voxels within each reservoir, subsequently giving them one of the five fluid class labels. A data frame is created with all the reservoirs' voxels, including their fluid class and frequency attribute values. The data frame is used to create a series of plots whose analyses will highlight the reliability of each attribute for fluid identification and gas saturation discrimination. This methodology is summarized in Figure 1-3.

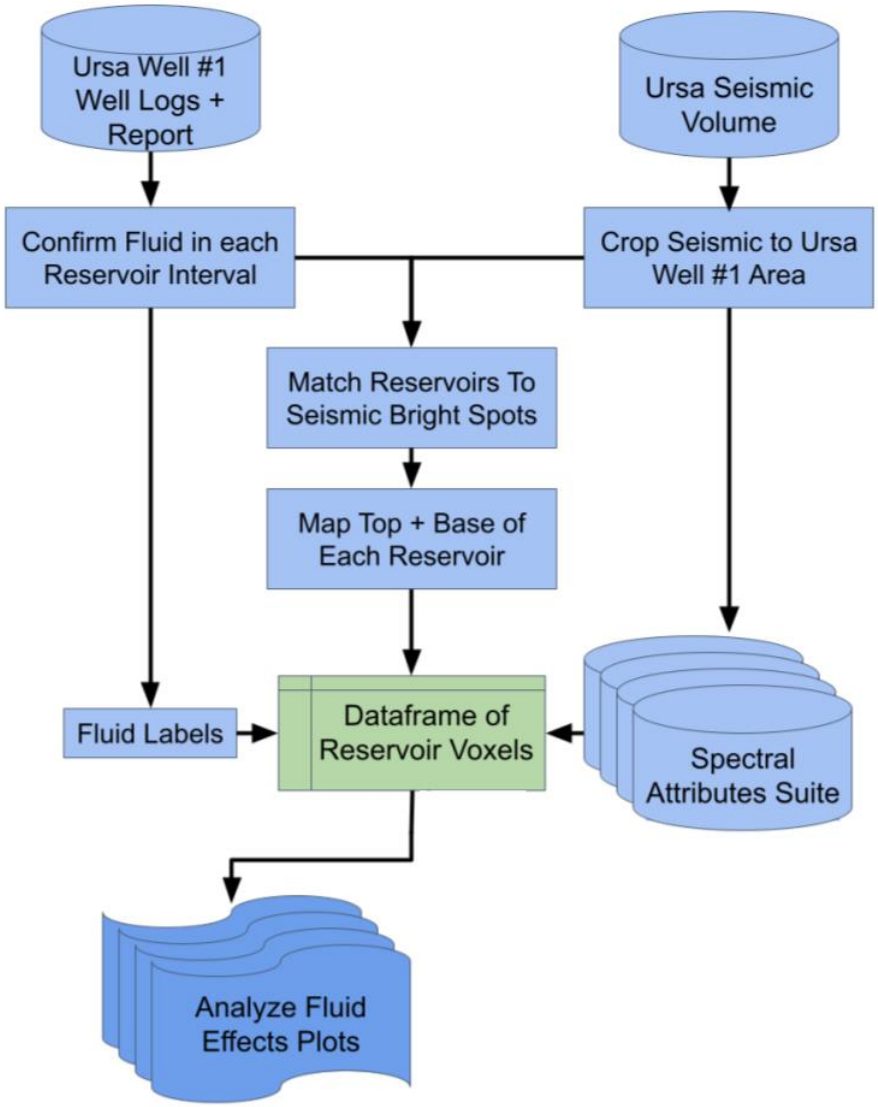

Figure 1-3: Workflow of the attribute analysis performed in this chapter.

Step 1: Seismic cropping

The reliability of the attribute analysis is contingent on the accurate interpretation of each fluid class within the reservoirs. Well logs and production data from Ursa Well #1 are the only data source used to interpret fluids within the reservoir. For this reason, the area of investigation is limited to the surrounding area of the well. An assumption is made that only one fluid exists per reservoir in the investigation area.

The selected investigation area that encompasses the 14 lines and 9 crosslines, totals 1,260,000 ft^2 (yellow dashed area in Figure 1-4a). As seen in Figure 1-4, the Ursa Well #1 is located at the intersection of seismic line 2844 and crossline 33220. The northern extent of the investigation area is extended to include more data points at the same time depth as the well, with the expectation that no fluid change occurs in this area (Figure 1-4a). The western extent is limited by the salt dome that acts as the seal and trap of the reservoirs. Figure 1-4b illustrates how the bright western amplitudes are avoided, as they are interpreted as salt contact. The south and eastern extents are limited by the time-depth and dip angle change. The attributes will be created for the mapped extent (red dashed area), but only the voxels inside the investigation area (yellow dashed area) will be used for the attribute analysis.

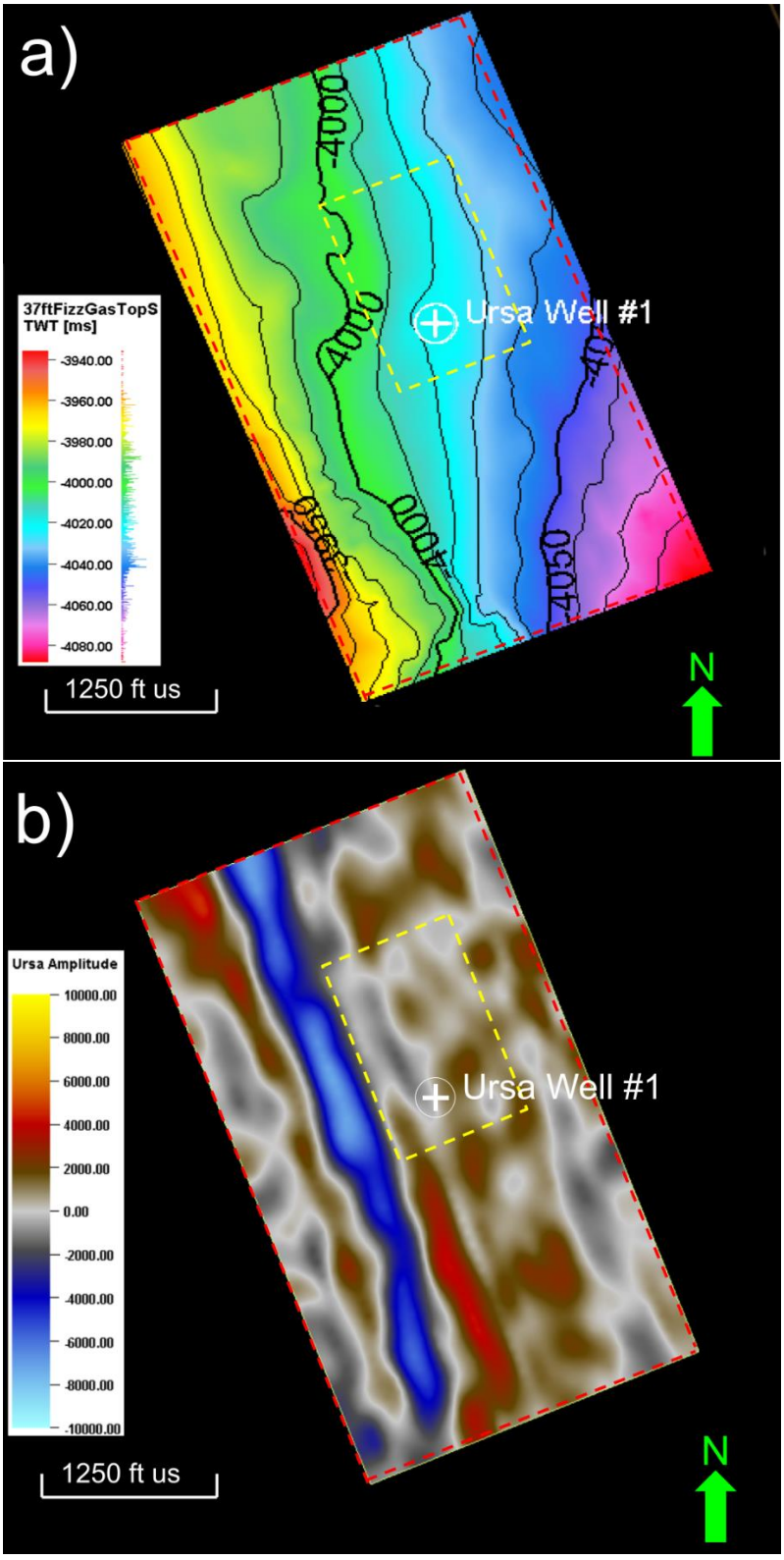

Figure 1-4: Amplitude map and structure contour map of two different reservoirs in the Ursa Field. The location of Ursa Well #1 is highlighted in white. The smaller dashed yellow area represents the boundaries of the area of investigation of the attribute analysis volume, while the more extensive red dashed area shows the extent of the horizon mapping.

a) Structure contour map of the uppermost reservoir (LGS). Notice that the northern extent of the area of investigation (yellow dashed box) is slightly longer to cover more area at the same time-depth as the well.

b) Time slice at 4956 of Ursa Amplitude. Notice that the western extent of the area of investigation (yellow dashed box) stops at the edge of the strong amplitudes, likely created by the salt diapir.

Step 2: Attribute creation

This research reveals how the full spectrum of frequencies is affected by variable gas saturations or the presence of other fluids. The frequency magnitudes and spectral shape attributes used in this study are summarized in Table 1-1, along with the expected response based on the literature. One can interpret the frequency response of hydrocarbons in two ways: by examining the magnitudes of discrete frequencies or by performing an analysis of the full frequency waveform. Complex matching pursuit spectral decomposition (SD) is performed to extract both sets of attributes mentioned. Only two other attributes are extracted using instantaneous techniques (instantaneous frequency and average frequency).

To reduce the vertical smearing produced by spectral decomposition of high magnitudes in the frequencies, the complex matching pursuit (CMP) SD algorithm was chosen over the continuous wavelet transform algorithm (CWT). This was particularly important due to the proximity of the stacked reservoirs, which caused the CWT volumes to have increased magnitudes from adding the responses of stacked reservoirs. The CMP algorithm uses "atomic decomposition" to reconstruct the signal using small "atom-sized" signals, resulting in reduced vertical smearing (Mallat, S. and Z. Zhang, 1993). With the CMP method, frequency volumes from 4 Hz to 50 Hz can be reliably extracted. The SD also extracts several attributes from the frequency waveform, including peak frequency, mean frequency, bandwidth, slope, roughness, skewness, and kurtosis, which statistically analyzes the full frequency waveform.

Keeping in mind that seismic attributes are simply a mathematical representation of one or more aspects of the original seismic data, the ones used in the study focus primarily on the frequency aspects of the seismic data. The peak frequency attribute indicates the frequency at the peak magnitude of the spectrum. The mean frequency attribute calculates the mean frequency

value based on the full frequency range. The bandwidth attribute measures the width of the frequency spectrum based on the spectral distance between the two half-power points. The slope attribute measures the angle of the linear regression line fitted to the two ends of the bandwidth. A positive slope would indicate that higher frequencies have higher magnitudes than lower frequencies, and a negative slope indicates the contrary. Roughness is a measure of the variability in the frequency spectrum and is calculated by taking the standard deviation of the first derivative of the slope. A high roughness value indicates more variable magnitudes in the spectrum, while a low roughness value indicates smoother magnitudes. A representation of bandwidth, slope, and roughness using the entire length of the cropped Ursa volume is shown in Figure 1-5a.

The skewness attribute is a measure of the asymmetry of the frequency spectrum and is calculated by taking the third standardized moment of the spectrum. A positively skewed spectrum has a longer tail to the high frequencies, while a negatively skewed spectrum has a longer tail to the lower frequencies (Figure 1-5b). In magnitude terms, positive skewness has a higher magnitude in the lower frequencies, and negative skewness has a higher magnitude in the higher frequencies. Kurtosis is a measure of the peakedness, and broadness, of the frequency spectrum and is calculated by taking the fourth standardized moment of the spectrum. A high kurtosis value indicates a thinner and peakier spectrum, while a low kurtosis value indicates a broader and shallow spectrum (Figure 1-5c). This research categorizes spectral shape attributes as slope, roughness, skewness, and kurtosis. The spectral shape attributes have only moderately been studied despite spectral decomposition algorithm availability for decades. Previous studies have shown that they can help identify channels (Zhang et al., 2008) and seismic sequences (Steeghs and Drijkoningen, 2001).

Instantaneous frequency and average frequency are also included in this study, exhibiting different results to the comparable peak frequency and mean frequency, respectively. Instantaneous frequency differs from mean frequency because it normalizes the frequency based on the instantaneous envelope. In practice, this leads to lower frequencies than the SD-based mean frequency, making the range of frequencies observed smaller than those in peak frequency. The average frequency also exhibits normalization based on the original amplitude, showing a smaller range of frequencies than the mean frequency.

Previous research has shown evidence for specific observations that we expect to see in the frequency attributes as a response to specific fluids. Seismic frequency is highly associated with varying amounts of gas saturation (Jin et al., 2017). Attenuation effects due to hydrocarbon presence have been continuously studied and proven to produce stronger lower frequencies than the rest of the spectrum (Odebeatu et al., 2006). The spectral shape attributes, skewness, kurtosis, roughness, and slope have been the basis for measuring attenuation (Li et al., 2016). The spectral bandwidth is wider in HGS than in LGS (Moreno et al., 2009). Wu's theoretical model indicated that LGS saturations produce the most attenuation (Wu et al., 2014).

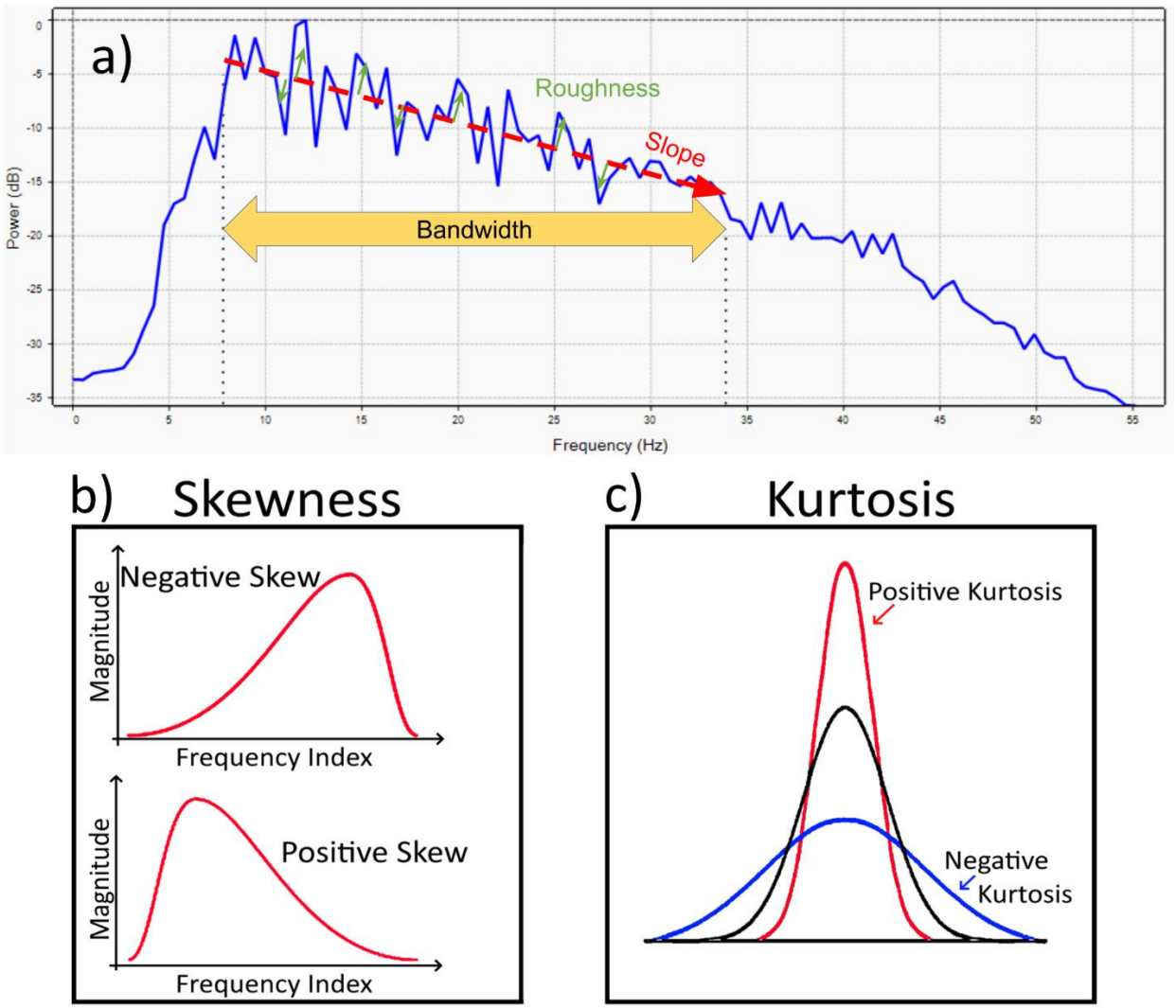

Figure 1-5: Spectral shape attributes illustrated. The horizontal axis represents the frequency index from zero to the maximum value, and the vertical axis shows the magnitude of each frequency index.

a) Frequency spectrum of the entire investigation area as an example. The width of the frequency index denotes the bandwidth attribute within two half-power frequencies (J-Low and J-High) indicated by the yellow double arrow. The slope (in red) is the best-fit straight line between the frequency spectrum from J-Low to J-High. The roughness (blue arrows) is the deviation from the slope.

b) Illustration of positive and negative skewness. Notice how positive skewness has high magnitudes in the low frequencies, and the tail skews to the higher frequencies. Negative skewness has high magnitudes in the high frequencies, and the tail skews to the lower frequencies.

c) Illustration of positive and negative kurtosis. Positive kurtosis (red) has a thinner range and higher frequency magnitudes, while negative kurtosis (blue) has a broader range and lower frequency magnitudes.

Attribute	Created for	References:	Understood Relationship to High Attenuation
Skewness	Spectral shape analysis - Attenuation	Zhang (2010)	Higher
Kurtosis	Spectral shape analysis - Attenuation	Zhang (2010)	Higher
Roughness	Spectral shape analysis - Attenuation	Zhang (2010)	Lower
Slope	Spectral shape analysis - Attenuation	Zhang (2010)	Lower
Spectral Bandwidth	Frequency Analysis of Seismic Data	Zhang (2010)	Lower
Mean Frequency	Frequency Analysis of Seismic Data	Zhang (2010)	Lower
Peak Frequency	Frequency Analysis of Seismic Data	Zhang (2010)	lower
Frequency Magnitudes (2 Hz interval)	Frequency Analysis of Seismic Data	Partyka et al., (1999), Castagna and Sun (2006)	Decreased magnitudes of the higher frequencies
Instantaneous Frequency	Frequency Analysis of Seismic Data	Liu and Marfurt (2007)	lower
Average Frequency	Frequency Analysis of Seismic Data	Liu and Marfurt (2007)	lower

Table 1-1: Table illustrating the attributes analyzed. Columns include information on the common use of attributes and expected values changes with increasing attenuation.

Step 3: Confirmation of reservoir fluids with well logs and reports

Previous research has been conducted in the Ursa reservoirs in search of a more accurate way to distinguish LGS. In 2001, Hilterman (2001) confirmed the presence of a LGS reservoir (high water saturation with gas) and a HGS reservoir (low water saturation with gas) among the strong reflectors of Ursa Well #1 using AVO and fluid substitution models with well log data. (Figure 1-2). He also confirmed the presence of a water-charged reservoir (fully water saturated) within a moderate amplitude reflector and oil (with variable water saturation and low gas oil ratios) in the remaining strong reflectors (Hilterman, 2001). A thick shale section is also interpreted from gamma ray logs separating the two reservoir sets.

Ursa Well #1 was ideal for the frequency attributes analysis because it encountered our five fluid classes of interest with minimal reservoir properties differences (Hilterman, 2001), excluding the shale section used as a control. Although digital logs were not available for this well, using a time-depth relationship from another well nearby made matching the seismic amplitudes to the gas-show logs and reports relatively straightforward. The vertical path of the borehole keeps the interpretation honest, ensuring with higher certainty that the area of investigation for the attribute analyses is representative of the production and other well data.

Step 4: Interpretation and mapping

Mapping the top and base of the reservoirs and 100 ms thick shale section was performed in a seismic interpretation software with a 90° phase rotated amplitude (Hilbert transform) volume to better observe the interfaces. The mapping (red dashed area in Figure 1-4) was extended beyond the investigation area (yellow dashed area in Figure 1-4) to illustrate better the extent of the data

used for the attribute analysis. The extended mapping also aids in selecting the investigation area by observing the reservoirs' depth changes, as discussed in Step 1.

A Hilbert transform cross-section of line 2844 is presented in Figure 1-6a, displaying the top and base of each reservoir color-coded to the interpreted fluid classes of Step 3. The dashed yellow box in Figure 1-6 coveys the extent of the investigation area. Notice how the western extent of the investigation area stops before the inclusion of the bright spots interpreted as the salt dome contact. This exclusion avoids the possibility of adding salt or mixed fluids in the attribute analysis.

Step 5: Labeling and extraction of reservoir voxels

The next step is to extract the voxels in each reservoir interval. This task is accomplished by creating a discrete reservoir value volume where the value increases by one after passing through each mapped horizon. The discrete value volume is observed in Figure 1-6b. The values of the frequency attributes suite and discrete value volumes are exported from the interpretation software and loaded into a Python coding notebook.

The volumes are now represented in a data frame where each row represents one voxel, and each column represents attribute values. The discrete reservoir values are used to eliminate all voxels that do not represent this research's geologic layers of interest (even numbered values in Figure 1-6b). The Oil-3 and Oil-5 layers (Figure 1-6a) were also removed as they did not exhibit representative bright spot amplitudes that this research intends to characterize. The remaining voxels are labeled with their respective fluid class (LGS, HGS, Oil, Water, and Non-Reservoir), as represented in Figure 1-6a. The oil reservoirs had variable water saturation and gas oil ratios but were simplified under a single “oil” class for this study.

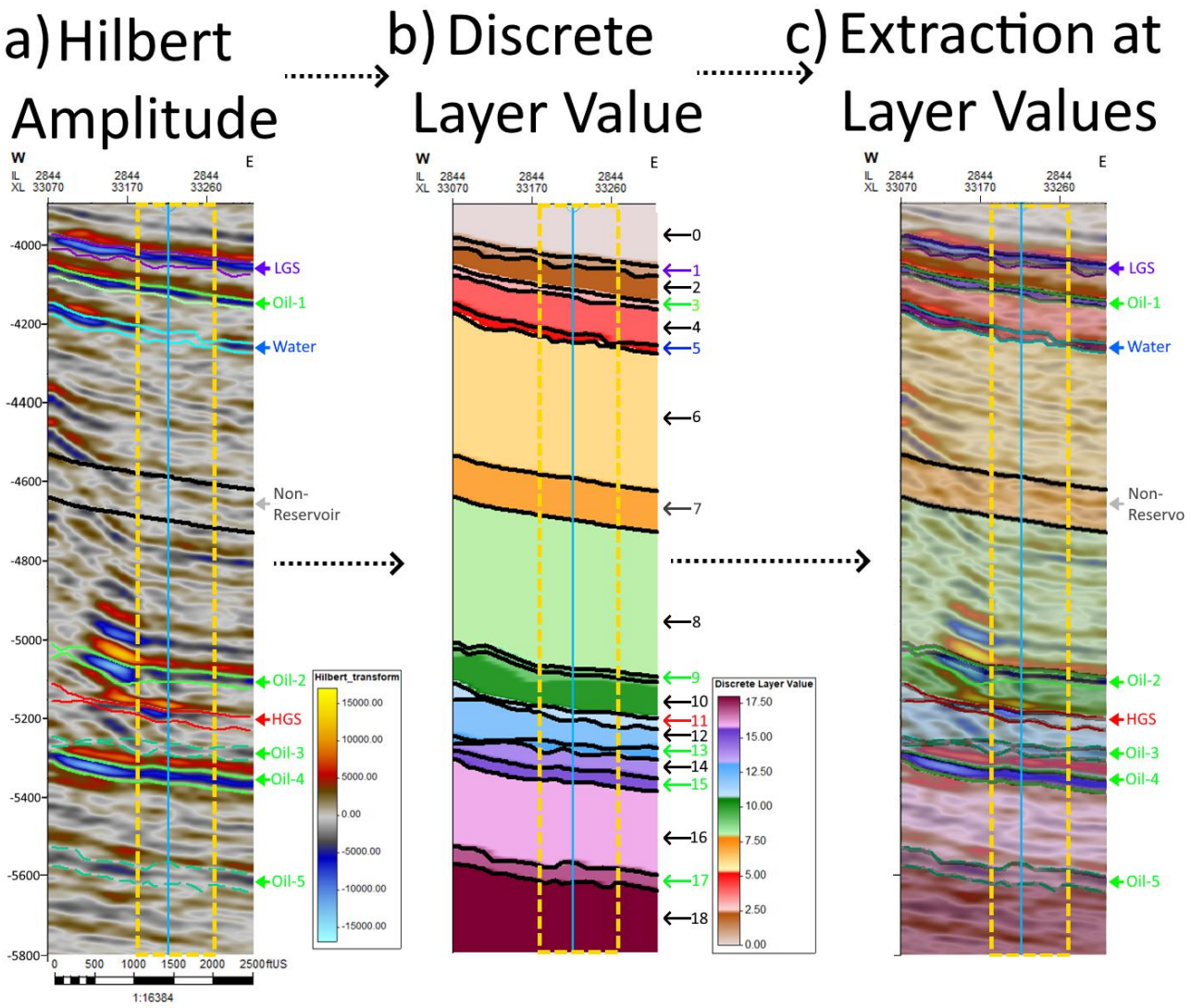

Figure 1-6: line 2844 cross sections showing Ursa Well #1 in cyan and a dashed yellow box highlighting the extent of the attribute analysis investigation area.

a) The 90° phase rotated amplitude (Hilbert transform attribute) and mapped horizons for the top and bottom of the reservoirs. This attribute was used to aid in the interpretation of the vertical extent of the reservoirs. Colored fluid class labels are presented on the right side, indicating the fluid class attributed to each.

b) Discrete layer value volume where every voxel in a reservoir holds a single value.

c) Overlayed a and b images to illustrate the method used to extract the frequency attribute values for each reservoir correctly. This example uses the Hilbert transform attribute not included in the attribute analysis.

Step 6: Plot creation and analyses

The data frame now allows for various attribute analyses where their value variability is examined within the context of the fluid classes. Various plots and graphs are created to ease the interpretation of fluid-related changes in the frequency attribute suite. The first plot examined is the covariance between the attributes without filtering by fluid class. The covariance matrix (Figure 1-7) shows the degree to which changes in one attribute are associated with changes in another. Box plots (appendix) and histograms (Figure 1-8) are used to observe the distribution of attribute values and how they differ between fluid classes. The final plot adds an extra dimension by cross-plotting two attributes and having each data point be colored by the fluid class (Figures 1-9 and 1-10). Cross plots are the best tools to analyze which attributes can reliably differentiate fluid classes. Discrete fluid clusters in the cross plot would indicate that those attributes can be used to distinguish fluid classes in seismic data.

RESULTS

The results presented in this section describe the covariance matrix, distribution histograms, and cross-plots of attribute values. The histograms and cross-plots are color-coded to represent the five fluid classes studied. Analyzing the attribute value distribution leads to a better understanding of the attenuation effects of each fluid class. Successful discrimination of the fluid classes is achievable when using the entire frequency attribute suite.

Covariance matrix of attributes

The attribute covariance for the reservoir voxels is presented in Figure 1-7. Both axes display the full frequency suite, and their intersection represents the heatmap color of their

covariance. Positive (blue) covariance indicates that as one attribute's value increases, the other attribute's value also increases. Negative (red) covariance indicates the opposite. High covariance will indicate that the attributes' values are related and that it might be redundant to observe both simultaneously as they exhibit some level of a linear relationship. Zero covariance would indicate that the attributes are independent, and observing both attributes simultaneously could exhibit a scatter plot where fluid classes can easily be distinguished.

The axes start at the top and left with the spectral shape attributes, followed by the two statistical measurements from the SD computation, continuing with the independent frequency magnitudes from low to high, and ending with the instantaneous statistical measurements. High covariance can be observed in 3 groups; spectral shape attributes among each other, roughness, slope, and mean frequency against <18 Hz frequencies and frequency magnitudes with low-frequency differences.

The SD statistical measurements (mean and peak frequency) have significant covariance with the spectral shape attributes and the low frequency magnitudes that are not observed with the Instantaneous statistical measurements. The significantly high covariance between the spectral shape attributes and frequencies magnitudes below 18 Hz is not observed for the higher frequencies. This observation indicates that the spectral shape attributes and statistical SD attribute values are highly dependent on the magnitudes of the lower frequencies.

The distribution histograms and cross plot presented next will prove the need to use the frequency attribute suite when discriminating between fluid types despite the high covariance between attributes.

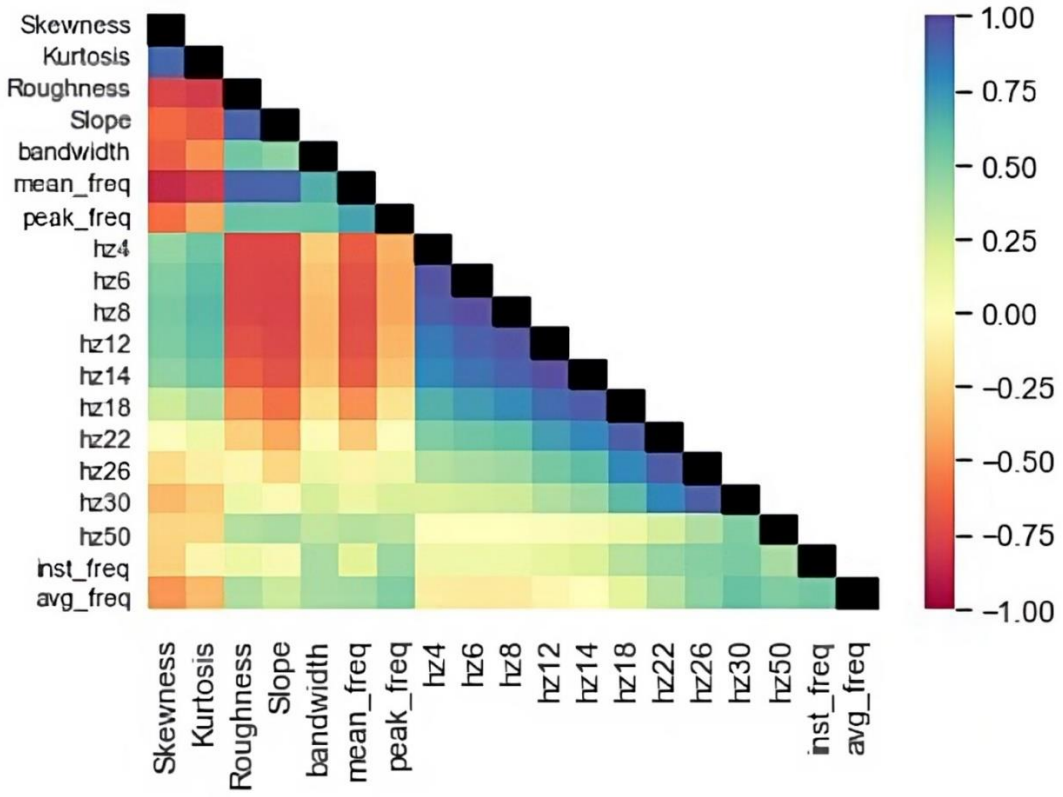

Figure 1-7: Color-coded covariance matrix illustrating the frequency attribute suite. Covariance measures the relationship between the values of the attributes. Positive covariance (blue-colored values) indicates that as the values of one attribute increase, the values of the second attribute increase at the same rate. Negative covariance (red-colored values) indicates that as the values of one attribute increase, the attributes of the second attribute decrease. Zero covariance (yellow-colored values) indicates that the attributes share no linear relationship.

Distribution histogram plot of attributes

Distribution histograms present a simple visualization method to analyze the range of values of each attribute against the fluid classes (Figure 1-8). Each histogram is colored to the fluid class they represent; LGS- purple, HGS- red, Oil- green, Water- blue, and Non-Reservoir- grey. The horizontal axis indicates the attribute value, while the vertical axis represents the number of data points. Figure 1-8 separates the frequency attribute suite into three groups to ease the analysis. The top group represents the spectral shape attributes. The center group represented the independent frequency magnitudes from low to high frequencies. While the last group is composed

of the four statistical measurements: mean and peak frequencies from the SD computation and instantaneous and average frequencies from the instantaneous computation.

None of the spectral shape attributes show isolated histograms for any fluid class, but some insightful observations can be made. Skewness is slightly more positive in LGS than in HGS, while some oil data points exhibit the maximum amounts of skewness. Negative skewness is only observed in a subset of the non-hydrocarbon fluid class, meaning they exhibit stronger magnitudes in the higher frequencies than in the rest of the spectrum. A similar relationship is observed in the kurtosis values, with higher kurtosis in LGS than in HGS. Close observations indicate that LGS is the only fluid class with no negative kurtosis. Oil is the only fluid class whose kurtosis values exceed the value of 7. The higher kurtosis in LGS indicates a more narrow and defined frequency spectrum than the other fluid classes. The narrower frequency spectrum of LGS is evident by observing that its maximum bandwidth is 18, a value that is exceeded by all other fluid classes.

Observing the histogram distribution of the fluid classes exemplifies the negative covariance of roughness and slope with skewness and kurtosis. The non-hydrocarbon fluids classes exhibited the minimum skewness and kurtosis values in contrast to the maximum values in roughness and slope. The positive slope for the non-hydrocarbon classes is consistent with the negative skewness as the magnitudes are more substantial in the higher frequencies. In contrast, the hydrocarbon classes have higher magnitudes in the lower frequencies that quickly decline at the higher frequencies defining their extremely negative slope values. Very few hydrocarbon data points have a roughness higher than a value of 2000, indicating that the hydrocarbon presence produces a smoother frequency spectrum.

The independent frequency magnitudes present the highest potential for hydrocarbon fluid class discrimination as the mean values of each fluid class exhibit the longest distance between

them. The most significant separation of LGS and HGS occurs at the intermediate frequency magnitudes (14 Hz – 22 Hz), with LGS having significantly higher magnitudes than HGS and oil. The separation from the LGS and HGS becomes near indistinguishable at the 4 Hz and 50 Hz frequencies. Oil has the highest magnitudes at this frequency extremes, observed in the low frequencies (4 Hz – 8 Hz) and the 50 Hz frequency.

The statistical attributes histograms at the bottom of Figure 1-8 highlight that HGS present higher mean and average frequencies than LGS. This observation is counterintuitive to the previous observation of their magnitudes. LGS has higher magnitudes across the frequency spectrum than HGS, yet LGS has lower statistical mean and average frequencies than HGS.

The effects of the normalization present in the calculation of the instantaneous attributes (instantaneous and average frequency) are observed when comparing the frequency ranges of mean and average frequency. The dominant mean frequency is 20 Hz, while the dominant average frequency is 15 Hz. This reduction of dominant frequency in the average frequency attribute causes the non-hydrocarbon classes to be shifted down/left more than the hydrocarbon classes. This shift is highlighted with the green and gray arrows, showing how the oil and non-reservoirs classes superimpose each other in the average frequency attribute but not in the mean frequency attribute.

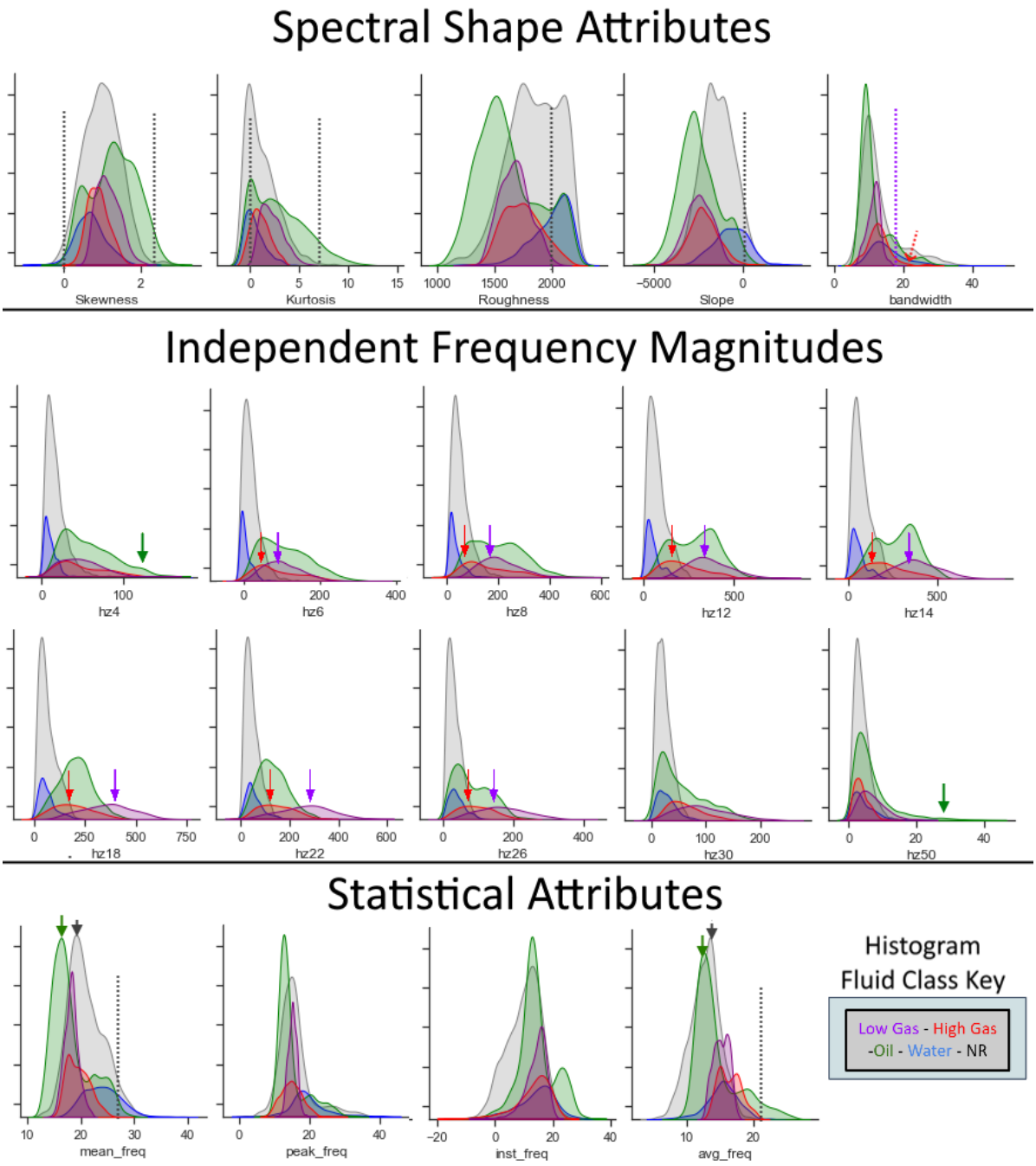

Figure 1-8: Value distribution histograms for all attributes used. The horizontal axis indicates the attribute's value, and the vertical axis indicates the number of data points with those values. Every attribute histogram plot presents a unique color histogram representing the range of values for each fluid class. Arrows and lines highlight significant observations presented in the results and discussion sections.

Cross plots of attributes

Although no single attribute exhibits distinct discrimination of the fluid classes in the histogram plots, successful fluid discrimination is possible after closely analyzing the attribute cross plots in Figures 1-9 and 1-10. The color-coded values of each fluid class are plotted to represent their distribution among two attributes. One axis represents the values of one attribute plotted against the values of the second attribute on the other axis.

The use of spectral shape attributes to discriminate hydrocarbon from non-hydrocarbon fluid classes is observed in Figure 1-9. Most cross plots (especially the ones highlighted in pink) show linear to parabolic relationships with a distinct transition from non-hydrocarbon classes to hydrocarbon classes. This fluid class transition usually starts with water data points and progresses, to non-reservoir, to HGS, to LGS, and ends with oil. Figure 1-9 confirms the need to analyze the cross plots of attributes with high covariance because the fluid classes' relationships can be observed when analyzing attributes together.

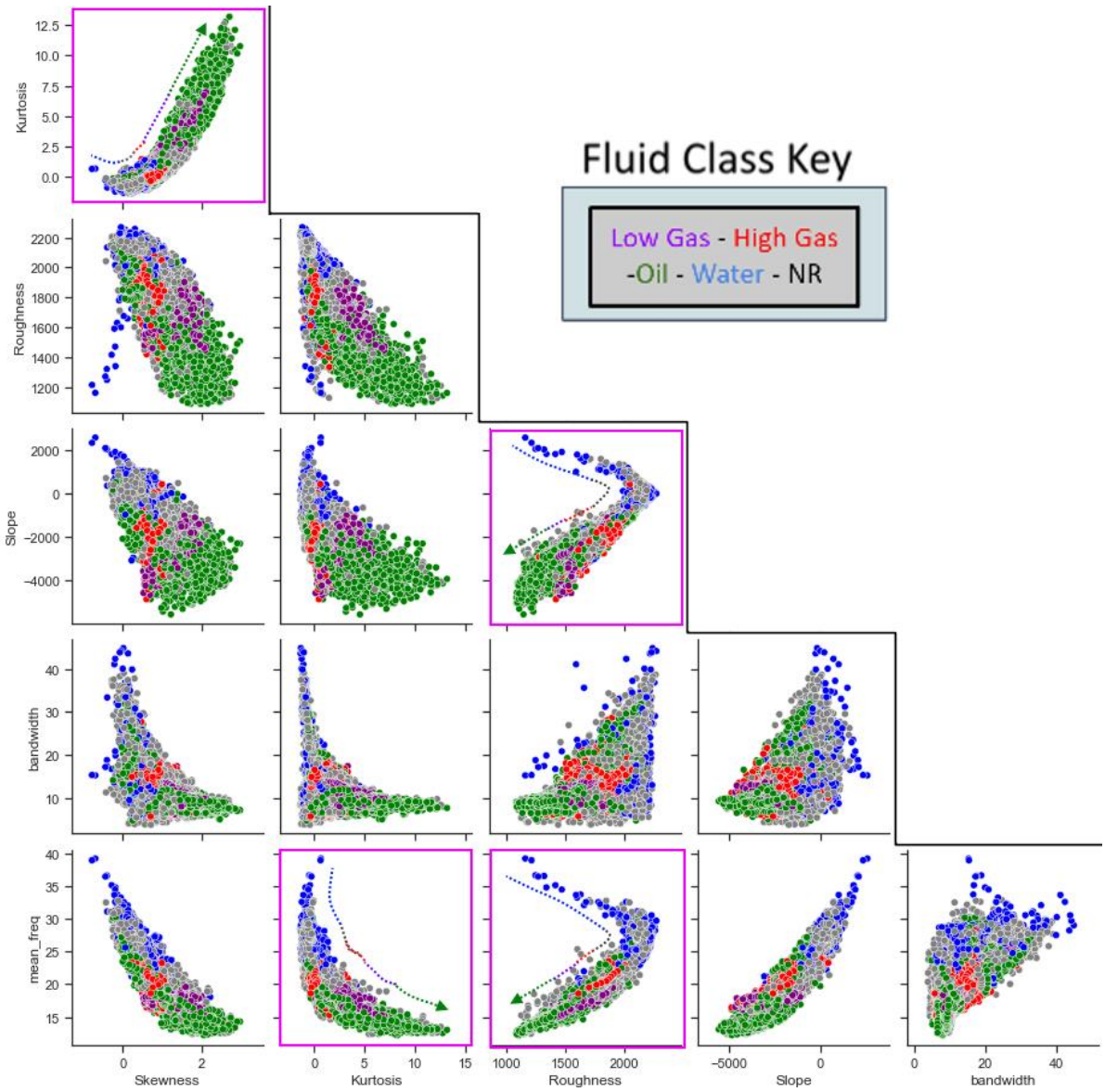

Figure 1-9: Cross-plot matrix of spectral shape, bandwidth, and mean frequency attributes. Horizontal and vertical axes show the full range of values for the two attributes used in each plot. Fluid class colored-coded data points values are present in each cross plot. Transitional colored arrows indicate the fluid class transition pattern that emerges when observing spectral shape attributes.

The discrimination of the hydrocarbon fluid classes is possible after the careful analysis of the 12 Hz frequency magnitude cross plots. Figure 1-10 cross plots the 12 Hz frequency magnitude versus the four spectral attributes, bandwidth, mean frequency, and the highest and lowest frequency magnitudes used in the investigation (50 Hz and 4 Hz, respectively). A distinct

separation of an oil cluster and LGS/HGS cluster is observed in the 12 Hz versus roughness cross plot. At magnitudes >400 for 12 Hz, the oil cluster is easily distinguished from the gas clusters due to the significantly lower roughness (<1750) in the oil data points.

Evidence to distinguish the LGS and HGS fluid classes is present in the 12 Hz versus 4 Hz cross plot of Figure 1-10. The high 12 Hz and low 4 Hz magnitudes present a distinguishable LGS cluster with significant separation from a HGS cluster. Although the HGS saturation cluster is mixed with oil data points, the previous roughness analysis allows the interpreter to isolate the oil fluid class.

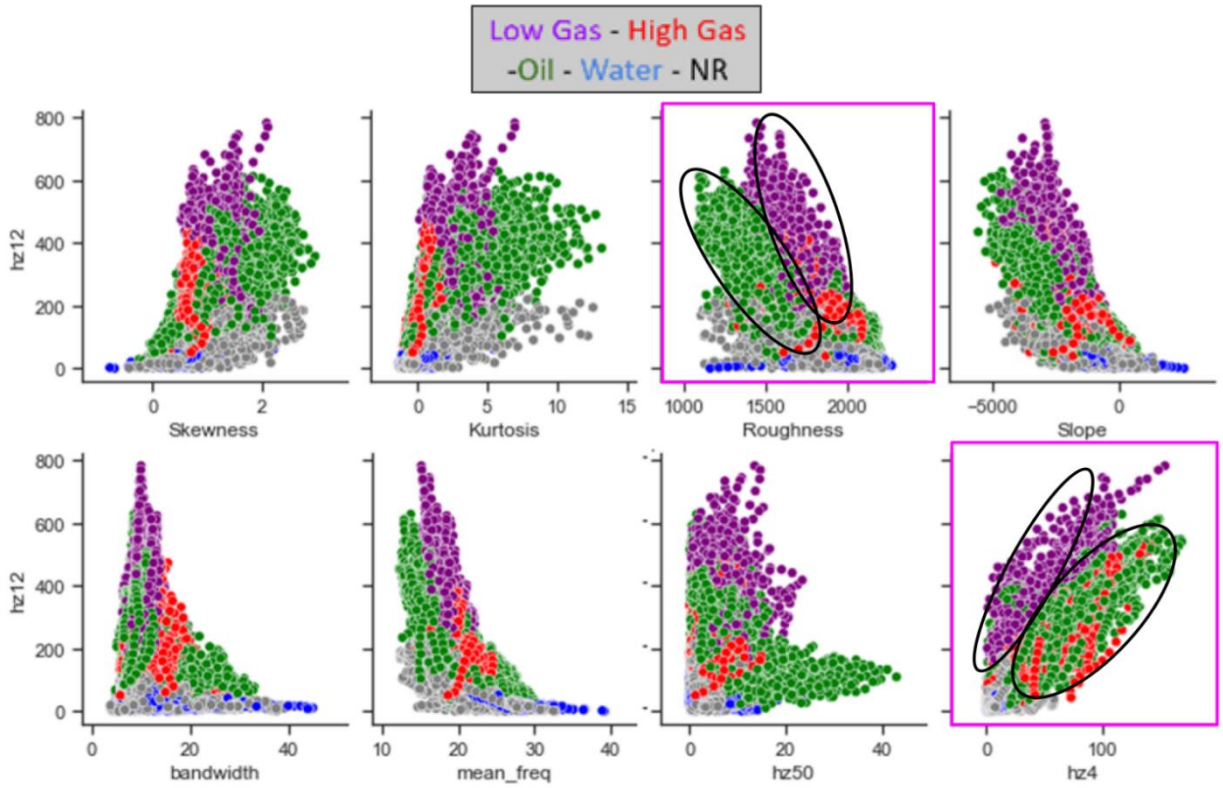

Figure 1-10: Cross-plot of the 12 Hz frequency magnitude against spectral shape attributes, highest frequency (50 Hz), and lowest frequency (4 Hz) magnitudes studied. Horizontal and vertical axes show the full range of values for the two attributes used in each plot. Fluid class colored-coded data points values are present in each cross plot. 12 Hz magnitude cross plots with roughness and 4 Hz illustrate the potential to discriminate hydrocarbon fluid classes. The black ovals indicate clusters that can be used to define the fluid classes.

DISCUSSION

The in-depth analysis of the attribute value ranges for each fluid class leads to a better understanding of the attenuation effects on the frequency spectrum. The saturation effects on the frequency spectrum are better documented using actual HGS and LGS reservoir responses. The analyses performed in the previous section indicate that fluid discrimination is possible with the frequency attribute suite. Although no single attribute can differentiate between the five fluid classes, analyzing attribute pairs can distinguish a fluid class at a time. The following section presents a series of interpretations of the fluid classes' effects on spectral shape attributes and individual frequency magnitudes across the studied spectrum.

Covariance

Interpreting the covariance (Figure 1-7) between the frequency suite aids in understanding the independent frequencies' relationship over the spectral shape attribute. The most important relationship is that the magnitude of frequencies <18 Hz largely dominates the values of the spectral shape attributes. This observation is intuitive with the slope and skewness attributes. The high magnitudes in the lower frequencies will lead to a more negative slope and positive skewness due to the energy imbalance. The non-intuitive realization is that strong magnitudes of <18 Hz frequencies lead to a very thin and smooth spectrum, as evidenced by decreased roughness and increased kurtosis. Considering that hydrocarbons tend to produce more substantial magnitudes in the lower frequencies, as the higher frequencies get attenuated, the observation of high skewness and kurtosis can lead to the successful identification of hydrocarbons in the subsurface. Low values of slope and roughness can also be interpreted as indicators for high attenuation, chiefly due to the magnitude decrease of the higher frequencies and the smoothing of the spectrum. The previous

interpretations would indicate that the spectral shape attributes could serve as alternative interpretation attributes to the discrete frequencies for detecting hydrocarbons in seismic data.

Distribution histogram plot of attributes

The distribution histograms for the attribute value ranges for each fluid class (Figure 1-8) allow for a series of interpretations that further expands our understanding of gas saturation and attenuation effects on seismic data. High attenuation will tend to reduce the higher frequencies more than the lower frequencies. Reduction of the higher frequencies would be represented as high skewness and kurtosis as the spectrum becomes more narrowed and skewed to the lower frequencies. Reducing the higher frequencies would also produce a more negative slope and low roughness as the energy smooths out into the lower frequencies. These observations of the spectral shape attributes can help us define the attenuation of the fluid classes.

The water and non-reservoir fluid classes should exhibit the lowest attenuation, representing the lowest density contrast against the background. The spectral shape attributes substantiate the lowest attenuation interpretation in the non-hydrocarbon classes by having the lowest skewness and kurtosis values and the highest roughness and slope values. Interpreting the oil attenuation is unachievable as it exhibits a range of values for all spectral shape attributes that exceed the maximum and minimum values of both HGS and LGS. These extreme ranges in the oil class are likely due to the inclusion of three oil reservoirs, compared to the single HGS and single LGS reservoirs in the study.

The generalized attenuation interpretation would indicate that LGS produces more attenuation than HGS as it exhibits higher skewness and kurtosis values, confirming Wu's models from 2014. The higher kurtosis in LGS would be interpreted as a shorter bandwidth, confirmed

with the bandwidth attribute, and reaffirms the observations from Moreno in 2009. The HGS and LGS reservoirs do present an unintuitive relationship. HGS has higher values of mean and average frequencies compared to LGS. This observation indicates that LGS exhibits more attenuation due to the reduction of higher frequencies. This observation would seem incompatible with the evidence that LGS consistently has higher magnitudes of all frequencies compared to HGS. The reduced magnitudes of the HGS frequencies would indicate higher attenuation.

Observing the full frequency suite that describes the spectrum, a unique relationship can be interpreted to distinguish varying amounts of gas saturations. Low gas saturation produces more attenuation resulting in higher skewness and kurtosis. However, as the saturation increases, the 12 Hz - 22 Hz frequency magnitudes decrease and transform into frequencies below 12 Hz and above 18 Hz, representing higher bandwidth and kurtosis. This interpreted relationship could explain why the amplitude responses from varying amounts of gas saturations are nearly identical, same cumulative frequency magnitudes but different distributions. More research needs to be performed with field data to understand better the gas saturation effects on attenuation and their effect on amplitudes.

Cross plots of attributes

The cross plots of Figures 1-9 and 1-10 substantiate using frequency attributes to discriminate fluid classes successfully. The spectral shape, bandwidth, and mean frequency cross plots in Figure 1-9 justify using the spectral shape as a hydrocarbon indicator. The prevalence of hydrocarbon classes to attenuate the higher frequencies produces significant slope and roughness reductions along with increased skewness and kurtosis. Although low magnitudes of higher frequencies also indicate non-hydrocarbon classes, spectral shape attributes can define the

attenuation effect that is more pronounced in the hydrocarbon classes. Spectral shape attributes should be further studied as they provide a straightforward method of measuring attenuation.

The 12 Hz discrete frequency magnitude cross plots in Figure 1-10 validate using the frequency suite as a discriminator of hydrocarbon classes. The different attenuating effects of the hydrocarbon classes observed in the histograms (Figure 1-8) produce distinguishable differences when carefully observing their entire frequency spectrum. The smoothing effects of the oil reservoirs present a distinguishable cluster when cross-plotting roughness against the 12 Hz frequency magnitudes. The LGS class also presents a distinct cluster when observing the 12 Hz vs. 4 Hz magnitudes cross plots, likely due to the shorter bandwidth of LGS that provide low values of the low frequency magnitudes. Although no discrete cluster was observed for HGS in any of the cross plots, the observations presented in this paragraph indicate that HGS can be separated with a combination of roughness, 12 Hz, and 4 Hz magnitudes.

CONCLUSION

The Ursa Field presents an excellent study area thanks to the low variability in reservoir properties. This study presented a highly detailed analysis of frequency attributes and their variability in the presence of various fluid classes in the Ursa Field reservoirs. Four distinct fluid classes (LGS, HGS, Oil, and Water) were identified across the length of the well using production data, removing the uncertainty present in seismic data. A study of the effects of each fluid class on the frequency spectrum was possible after careful extraction of attribute values around the proximity of the well. The addition of a shale section provided excellent contrast in the analyses, which helped frame the different fluid effects better.

Using spectral shape attributes to measure attenuation is intuitive and straightforward. Using the water and non-reservoir classes as a control for little to no attenuation indicates that attenuation increases as slope and roughness increase. Zero or negative skewness and kurtosis also indicate little attenuation effects as the frequency spectrum has higher magnitudes in the higher frequencies. This attenuation interpretation indicates that LGS produces more attenuation than HGS saturation. Although counterintuitive, this interpretation is consistent with Wu's synthetic models.

This chapter demonstrates that the frequency suite of attributes can define the fluids and gas saturations with post-stack seismic, but a clear physics model cannot be defined. The gas saturation relationship to the frequency spectrum remains inconclusive in this study. This conclusion is justified by the higher average and means frequencies in HGS but higher magnitudes of the full spectrum in LGS. Further work presented in the next chapter will demonstrate that using machine learning to learn from this chapters findings can lead to successful fluid class identification in multi-dimensional space that is not achievable as a human interpreter.

ACKNOWLEDGMENTS

I am immensely grateful to AASPI for their attribute creation software, which has been crucial in the extraction of important seismic attributes from my data. I would like to thank Python coding for its user-friendly and versatile nature, which has made the coding process efficient and enjoyable. Without Python, this project would not have been possible. I am also grateful to the Segio library for providing a comprehensive suite of tools for seismic data analysis, which has been integral to the analysis and interpretation of my research data. In addition, I would like to

extend my thanks to the Seaborn library, which has facilitated the visualization of complex data in an intuitive and visually appealing manner. Furthermore, I would like to thank the Pandas library for its powerful data manipulation capabilities, which have enabled me to efficiently clean and preprocess large datasets. Finally, I would like to express my deep appreciation to SLB for their generous donation of Petrel licenses to the University of Oklahoma. This donation has allowed me to perform sophisticated seismic interpretation and has greatly enhanced the quality and accuracy of my research.

REFERENCES

Batzle, Michael. "Seismic Evaluation of Hydrocarbon Saturation in Deep-Water Reservoirs." Colorado School of Mines, Golden, CO (United States), April 30, 2006. https://doi.org/10.2172/898116.

BOEM (Bureau of Ocean Energy Management). "Deepwater Gulf of Mexico December 31, 2019." OCS Report BOEM 2021-005, 2021.

Castagna, J.P., and S. Sun, 2006, "Comparison of spectral decomposition methods." *First Break*, 24, 75-79.

Elshahawi, Hani. "Deepwater Exploration and Production in the Gulf of Mexico - Challenges and Opportunities." *Petrophysics - The SPWLA Journal of Formation Evaluation and Reservoir Description* 55, no. 02 (April 1, 2014): 81–87.

Galloway, William E. "Chapter 15 Depositional Evolution of the Gulf of Mexico Sedimentary Basin." In *Sedimentary Basins of the World*, 5:505–49. Elsevier, 2008. https://doi.org/10.1016/S1874-5997(08)00015-4.

Galloway, William E. "Chapter 15 Depositional Evolution of the Gulf of Mexico Sedimentary Basin." In *Sedimentary Basins of the World*, 5:505–49. Elsevier, 2008. https://doi.org/10.1016/S1874-5997(08)00015-4.

Hilterman, Fred J.. "Seismic Amplitude Interpretation": Society of Exploration Geophysicists and European Association of Geoscientists and Engineers. *2001 SEG/EAGE Distinguished Instructor Short Course*, 2001.

Jin, Zhaoyu, Mark Chapman, Xiaoyang Wu, and Giorgos Papageorgiou. "Estimating Gas Saturation in a Thin Layer by Using Frequency-Dependent Amplitude versus Offset

Modelling." *Geophysical Prospecting* 65, no. 3 (2017): 747–65. https://doi.org/10.1111/1365-2478.12437.

Li, Fangyu, Sumit Verma, Huailai Zhou, Tao Zhao, and Kurt J. Marfurt. "Seismic Attenuation Attributes with Applications on Conventional and Unconventional Reservoirs." *Interpretation* 4, no. 1 (February 1, 2016): SB63–77. https://doi.org/10.1190/INT-2015-0105.1.

Liu, Jianlei, and Kurt J. Marfurt. "Instantaneous Spectral Attributes to Detect Channels." *GEOPHYSICS* 72, no. 2 (March 2007): P23–31. https://doi.org/10.1190/1.2428268.

Mallat, S.G., and Zhifeng Zhang. "Matching Pursuits with Time-Frequency Dictionaries." *IEEE Transactions on Signal Processing* 41, no. 12 (December 1993): 3397–3415. https://doi.org/10.1109/78.258082.

Moreno, Carlos, Maria A Perez, Jeff Meyer, Alan Huffman, Mohamad Etemadi, and Laszlo Benkovics. "Hydrocarbon Prospecting in Deepwater Trinidad Using AVO and Spectral Decomposition," n.d., 6.

O'Brien, John. "Seismic Amplitudes from Low Gas Saturation Sands." *The Leading Edge* 23, no. 12 (December 2004): 1236–43. https://doi.org/10.1190/leedff.23.1236_1.

Odebeatu, Emeka, Jinghua Zhang, Mark Chapman, Enru Liu, and Xiang-Yang Li. "Application of Spectral Decomposition to Detection of Dispersion Anomalies Associated with Gas Saturation." *The Leading Edge* 25, no. 2 (February 2006): 206–10. https://doi.org/10.1190/1.2172314.

Partyka, G., J. Gridley, and J. A. Lopez, 1999, "Interpretational applications of spectral decomposition in reservoir characterization." *The leading Edge*, 18, no. 3, 353-360.

Steeghs, Philippe, and Guy Drijkoningen. "Seismic Sequence Analysis and Attribute Extraction Using Quadratic Time-frequency Representations." *GEOPHYSICS* 66, no. 6 (November 2001): 1947–59. https://doi.org/10.1190/1.1487136.

Wu, Xiaoyang, Mark Chapman, Xiang-Yang Li, and Patrick Boston. "Quantitative Gas Saturation Estimation by Frequency-Dependent Amplitude-versus-Offset Analysis." *Geophysical Prospecting* 62, no. 6 (2014): 1224–37. https://doi.org/10.1111/1365-2478.12179.

Zhang, Kui., 2010, Seismic Attribute Analysis of Unconventional Reservoirs, and Stratigraphic Patterns: Ph.D. thesis, University of Oklahoma.

Zhang, Kui, Weiguo Li, and Fred Hilterman. "Gulf of Mexico Fizz and Gas Separation with Calibrated AVO Impedance." In *SEG Technical Program Expanded Abstracts 2007*, 1947–51. Society of Exploration Geophysicists, 2007. https://doi.org/10.1190/1.2792871.

Zhang, Kui, Kurt J. Marfurt, and Yanxia Guo. "Volumetric Application of Skewed Spectra." In *SEG Technical Program Expanded Abstracts 2008*, 919–23. Society of Exploration Geophysicists, 2008. https://doi.org/10.1190/1.3063789.

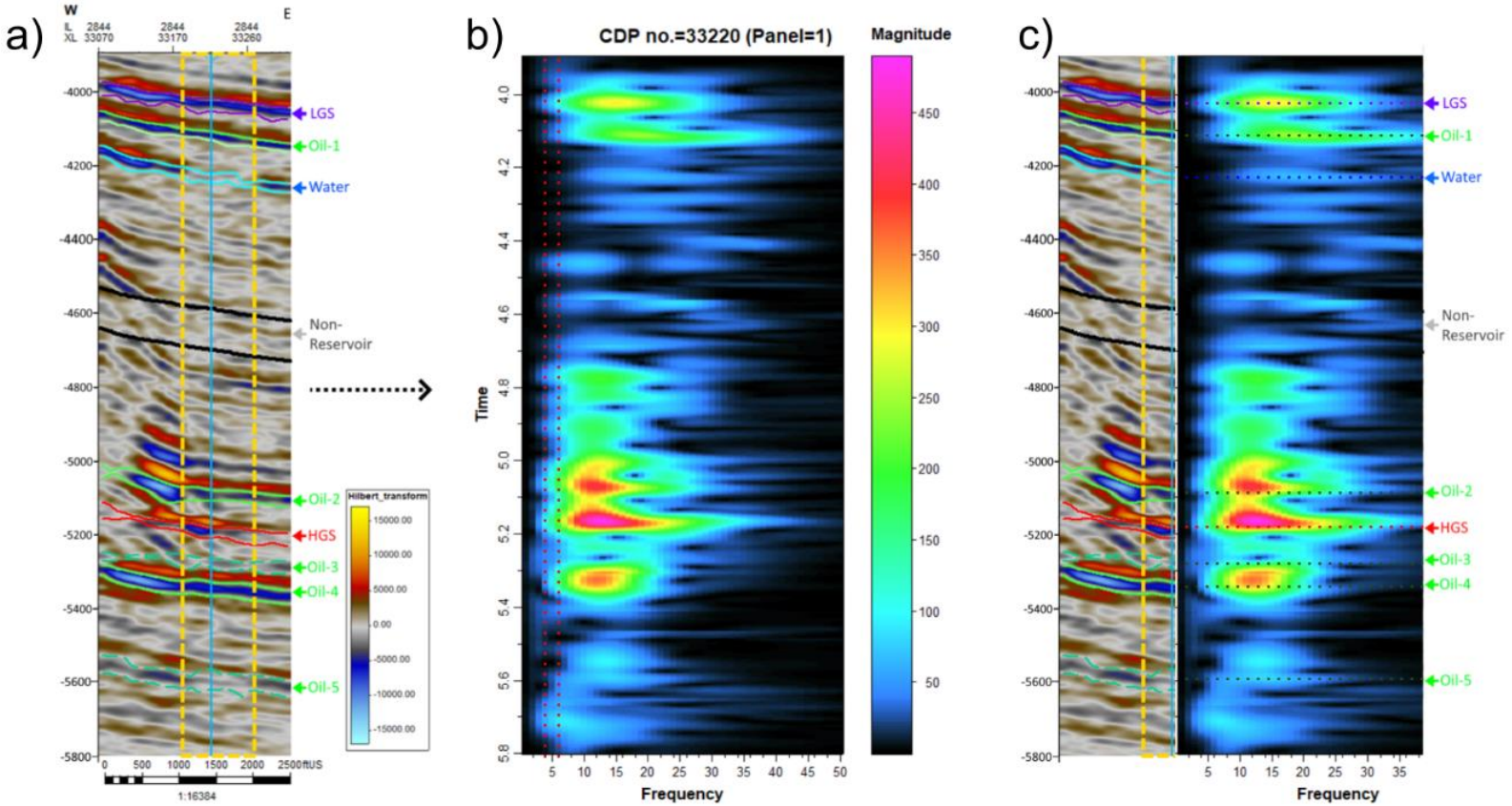

Appendix, Figure 1-1: a) The 90° phase rotated amplitude (Hilbert transform attribute) and mapped horizons for the top and bottom of the reservoirs. Light blue line representing the Ursa Well#1 path **b)** Frequency gather at the location of the well. Red dotted lines represent the two lowest frequencies used in the study (4 Hz and 6 Hz). **c)** Seismic volume and frequency gather side by side with dotted lines labeling the frequency magnitudes representative of each reservoir and fluid.

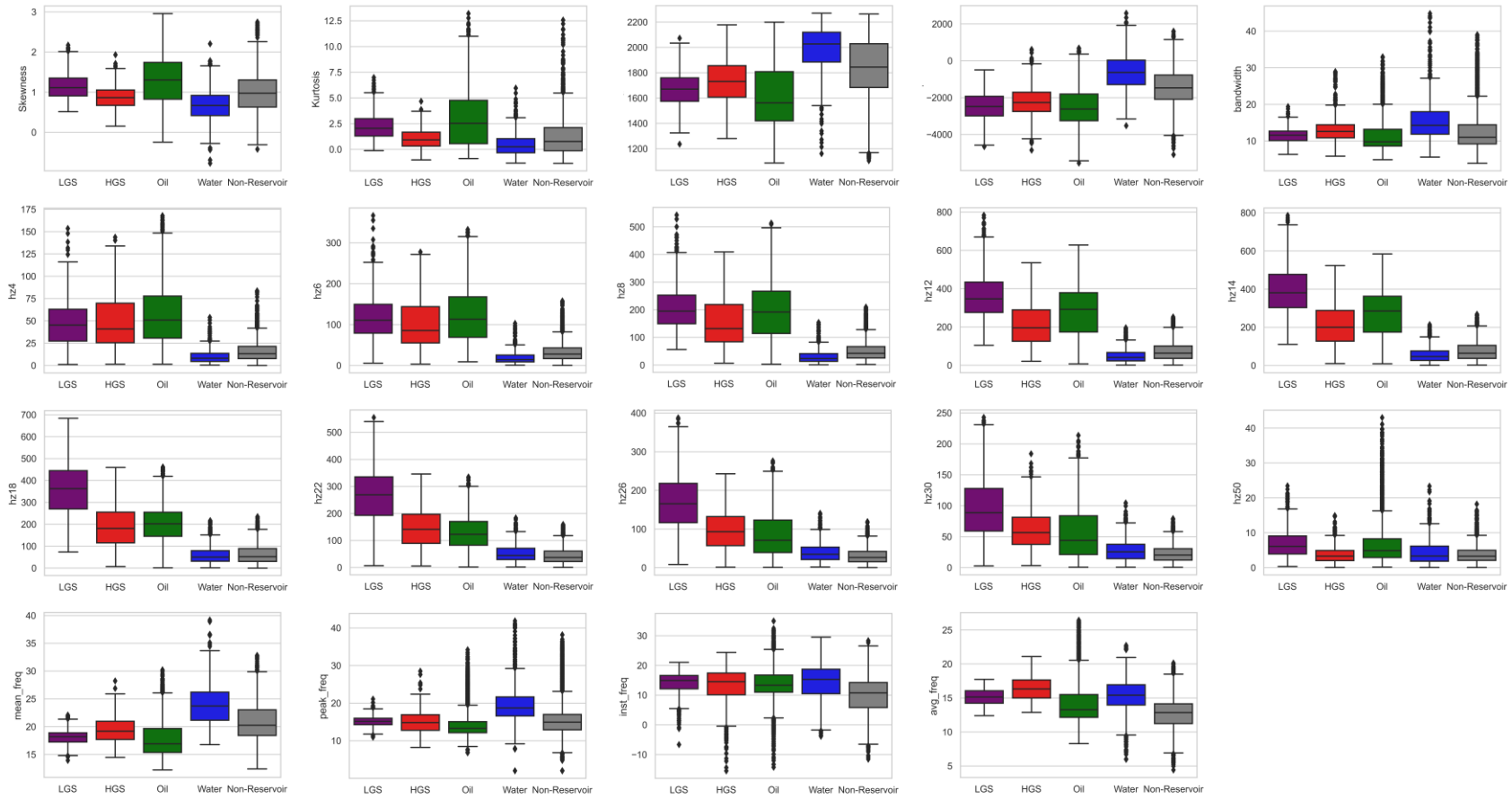

Appendix, Figure 1-2: Box plots representing the range of values for all attributes and color-coded by fluid class. The vertical axis indicates the attribute's value, and the horizontal axis depicts fluid class. The colored box itself represents 50% of the data (lower part is the 25th percentile and the upper part is the 75th percentile). The line in the box represents the median of the data. The whiskers extend above and below to represent 99% of the data. The dots represent the remaining 1%.

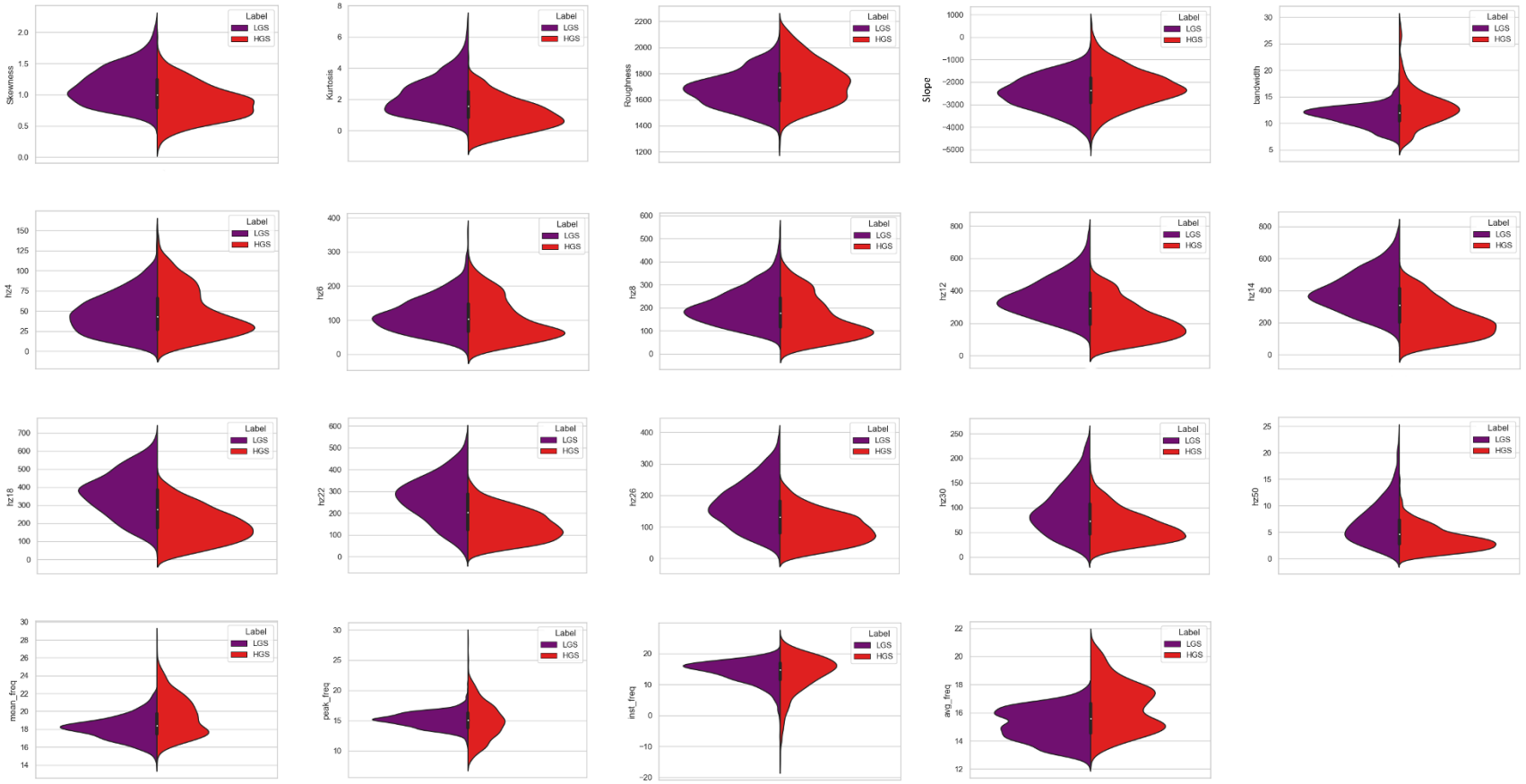

Appendix, Figure 1-3: Violin plot representing range of attribute values for LGS and HGS. The vertical axis represents the attribute value. Each gas saturation fluid class is represented by a violin shape, which is split in half along the vertical axis. The width of the violin at any given point represents the density of the data points at that value. The white dot in the center of the violin represents the median value of both classes.

CHAPTER 2: SUPERVISED MACHINE LEARNING METHODS TO DISCRIMINATE RESERVOIR FLUID PRESENCE AND SATURATION

ABSTRACT

This chapter explores the use of supervised machine learning algorithms to predict the presence of hydrocarbon fluids and their economic viability using frequency-related seismic attributes. Herein a new workflow is proposed that applies machine learning and the insights gained from the frequency-related multi-attribute analyses in Chapter 1 to predict water, oil, and high or low gas saturations within clastic reservoirs of the Miocene Gulf of Mexico. After data conditioning, the models are trained on labeled data from the Ursa Field dataset, where a blind test is performed along the perimeter of the well. The models are then validated on the King Kong and Lisa Anne Field dataset, where four distinct wells are present that contain oil and both high and low gas saturations. The k-nearest neighbors decision tree and random forest algorithms are tested on both datasets for their robustness in classifying the fluid types.

The explanative AI method SHAP is used on the trained random forest model to gather information on the importance of each attribute for the classification of each fluid class. The SHAP values analysis shows that high gas saturation is better identified with high magnitudes of the low frequencies (4 Hz – 8 Hz), high bandwidth, and lower skewness and kurtosis values. In contrast, low gas saturation is better identified with high magnitudes of the medium frequencies (12 Hz – 22 HZ), lower bandwidth, and higher skewness and kurtosis values.

The model predictions in the Ursa blind test provided excellent observations on the reliability of the models. All three models predict the extended reservoirs correctly, as verified from the fluids found in the well. Where fluid predictions differ, the correct fluid density

relationships are observed. Observing a gas-oil fluid contact flat spot and gas patches at the top of the oil reservoirs evidences this. These observations, although not fully validated due to lack of well data at those locations, bring confidence to the models' prediction capabilities. The validation tests in the King Kong and Lisa Anne Fields confirm the successful predicting abilities of the decision tree and random forest models. The models correctly predicted the fluid class in three out of four wells.

Supervised machine learning algorithms for reservoir fluid identification and saturation prediction show promising results. The K-nearest neighbors model is applicable when using the same dataset for training and prediction. In comparison, the decision tree and random forest models excelled at using the training data from the Ursa dataset and correctly predicting the reservoir fluids in the King Kong and Lisa Anne dataset. Correct predictions of reservoir fluids in a new field with no well data and post-stack seismic data would be impossible as a human interpreter. The study highlights the potential of machine learning to revolutionize the field of hydrocarbon exploration and production by providing a more robust way to risk prospects using exclusively post-stack seismic data and frequency attributes.

INTRODUCTION

Machine learning (ML) has emerged as a vital tool in the field of artificial intelligence (AI), enabling the development of algorithms that can learn from large datasets and make independent, predictive decisions. One of the significant benefits of machine learning is its ability to interpret complex relationships between multiple variables, which may not be immediately apparent to human interpreters restricted to observing data in three dimensions. Machine learning can be

broadly classified into supervised and unsupervised learning. Both have their strengths and weaknesses, and the choice of learning type will depend on the targeted objectives and the available data. Supervised learning is often used in cases where the target output is well-defined, and the labeled data is readily available.

On the other hand, unsupervised learning is often used in cases where the data is unlabeled, or the goal is to uncover hidden patterns or relationships in the dataset. One of the drawbacks of unsupervised machine learning is the lack of control over the desired results and the lack of immediate geologic interpretation. In this study, we explore using supervised machine learning algorithms to predict the presence of hydrocarbon fluids and their economic viability by using various post-stack seismic attributes focused on analyzing the frequency spectrum.

The gas saturation problem that creates uneconomical bright spots is not fully resolved today, even using AVO or inversion methods. As presented in Chapter 1, the frequency attributes suite analysis indicates that combining these attributes can discriminate between different fluids and gas saturations. To this end, we propose a new workflow that utilizes supervised machine learning algorithms to train a model capable of predicting the fluids and their economic feasibility within reservoirs. The machine learning model will use insights from the frequency suite multi-attribute analysis to predict: water, oil, high or low gas saturations (HGS and LGS, respectively), and non-reservoir classes. Furthermore, each attribute's importance in discriminating between classes will be analyzed using explainable AI called SHapley Additive exPlanations (SHAP).

Training a machine learning model to differentiate between fluid classes requires correct input attributes, appropriate labeling, and a robust algorithm. The optimal attributes highlight fluids' elastic properties and minimize geology's effects. The labels must be as accurate as possible and come from the actual observations in well data of those fluids within the reservoir. The first

Chapter of this research covered the attribute selection and the labeling of the training data. The algorithm must be robust enough to observe minimal differences within attributes and make correct classifications even in the presence of seismic noise. The algorithms tested are k-nearest neighbors (KNN), decision tree (DT), and random forest (RF).

Labeled data from the Ursa Field is used to train the machine learning models, as discussed in Chapter 1. To examine their predictive ability, the trained models predict a more extensive area around Ursa Well #1. The correct expected result is that most of the voxels in each reservoir should have fluid predictions representative of the fluid classes present at the location of the well. Fluid types can change along the reservoirs' dip direction or faults, and those alternative fluid predictions will be analyzed for geological accuracy.

Subsequently, the models will be validated on the King Kong and Lisa Anne fields, which have reservoir and geological properties similar to the Ursa Field. The King Kong and Lisa Anne Fields (KKLA) are ideal for validating the models and testing transfer learning because they contain proven high and low gas saturation reservoirs and an oil reservoir in an area with similar lithologies. The process of using a dataset for training and a separate dataset to validate the model is called transfer learning. This approach has significant implications for early exploration stages. This ML methodology allows for more accurate predictions and risk assessments of fluids and their economic potential without requiring pre-stack data, AVO analysis, inversion methods, or even wells in the exploration area. Ultimately, our study highlights the potential of machine learning to revolutionize the field of hydrocarbon exploration and production by providing a more robust way to risk prospects.

Previous machine learning for seismic facies and fluid characterization

Much of the machine learning research with seismic data has successfully identified geological facies with supervised and unsupervised methods (e.g., La Marca and Bedle, 2022; Lubo-Robles et al., 2021; Ao et al., 2019). Using SHAP in a supervised random forest classifier has proven successful in understanding attribute importance in seismic facies classification of salt domes and mass transport deposits (Lubo-Robles et al., 2020).

Unsupervised approaches like Self Organizing Maps (SOM) have been used to tackle the problem of correctly identifying gas saturation (Chenin and Bedle, 2022). Chenin's research successfully used a suite of amplitude and frequency attributes to differentiate between HGS and LGS reservoirs in Ursa Well #1 and in the KKLA Fields. The SOM unsupervised method requires that both HGS and LGS reservoirs be present and confirmed by wells so interpreters can recognize the cluster classifications to be further interpreted in an adjacent prospect. The method discussed is not applicable when the model is applied to a new basin where well log information may not exist, variability in the input attributes deviates, or geology differs.

The research presented in this Chapter builds upon the findings of Chenin and Bedle, who found that discrimination of gas saturation is possible with unsupervised machine learning and post-stack seismic attributes. The new supervised approach presented in this research trains a model in the Ursa seismic survey and is later applied to a different survey (KKLA) to classify hydrocarbon fluids, presenting a novel example of using transfer learning from one seismic dataset to another, for low gas saturation discrimination. This new methodology eliminates the need for well data to interpret clusters and allows its use in any seismic dataset of similar geological and geophysical properties.

Geologic setting

The geologic and production history of the Gulf of Mexico (GOM) was previously detailed in Chapter 1. The details of the Ursa Field, and more specifically, the reservoirs found in Ursa Well # 1, were also described in Chapter 1. In summary, the Gulf of Mexico is a prolific oil and gas basin covering 600,000 square miles and extends from the Texas coast to the western Florida coast. It began forming 200 million years ago through a rifting process. A key defining factor of GOM's stratigraphy is the prevalence of allochthonous salt throughout the basin that pierces kilometers thick of Cenozoic sediment (Galloway, 2008). Hydrocarbon migration occurs mainly along the faults and accumulates in the highly porous Cenozoic sands. The salt acts as one of the primary trapping mechanisms in the area, leading to many economic reservoirs being drilled at the flanks of the salt domes. Exploration of the GOM has been ongoing for nearly 100 years and has been driven by adopting newer seismic technologies. However, direct hydrocarbon indicators have limitations in accurately quantifying the level of gas saturations, leading to inaccurate hydrocarbon risking for prospects and thus resulting in potential monetary losses for companies. (Elshahawi, 2014; Galloway, 2008)

The King Kong and Lisa Anne Fields were selected as the ideal place to validate the models as they share many similarities with the Ursa Field. King Kong and Lisa Anne are located in the Green Canyon protraction areas, 84 miles southeast of the Ursa Field and around 160 miles south of New Orleans. The King Kong and Lisa Anne Fields are located in blocks 473 and 474, respectively, and Lisa Anne is 6 miles east of King Kong (Figure 2-1). Both fields lie on the flanks of a mini basin formed from the underlying salt bodies and are seismically characterized by two trough-peak doublets that define an upper and lower reservoir (O'Brien, 2004).

The targeted interval for the KKLA Fields is the trough-peak doublets of Plio-Pleistocene age reflectors at 11,750 ft subsea depth. The reservoirs are great quality sands with porosities averaging around 30% and stretching over three fault blocks and are described as deepwater deposits of sheet sands from a northerly source (O'Brien, 2004). The area around the King Kong and Lisa Anne Fields provided significant challenges to the operators relying on bright spots as direct hydrocarbon indicators. Multiple wells have perforated the Plio-Pleistocene age reflectors encountering a variety of fluids and saturations, resulting in a complex area for hydrocarbon risk assessment.

Eni was the initial operator in the area in 1991 when "Well B" was drilled in the down-dip southeast area of the bright spot of the King Kong Field (Figure 2-1). Despite drilling the highest amplitude bright spot in the investigation area, their excitement dissipated when they encountered a dry hole with low gas saturation. It took Eni nearly a decade before they decided to drill the King Kong Field again, and in 2001 they drilled further up-dip and northwest of their original well. This new "Well A" was highly economical as they found high saturations of gas and oil. This success from Eni allowed the drilling of two sidetracks to produce the reservoir thoroughly. Their success led Anadarko (now Occidental Petroleum) to drill "Well D" in 2002 in a moderately high amplitude six miles west, in what is now referred to as the Lisa Anne Field. Disappointedly, the well that perforated the Lisa Anne Field's target reservoir was considered uneconomical when they encountered gas in low saturations between 5% to 25% (O'Brien, 2004). The shortcomings of Anadarko did not stop Eni from continuing exploration in the area, and in 2008 they drilled "Well C." This final well in the KKLA Fields is located in a bright amplitude area across a fault southeast of the King Kong Field and proved productive with oil. A summary of all four wells, including API numbers, is presented in Table 2-1.

Name in Project	UWI (60-811)	Field	Amplitude	Reservoir Fluid
Well A	40273 (00-01-02)	King Kong	High	HGS + Oil
Well B	50081	King Kong	High	LGS
Well C	40516	King Kong Flank	Moderate-high	Oil
Well D	40334	Lisa Anne	Moderate	LGS

Table 1-1: Information on the four wells in the King Kong and Lisa Ann fields. Notice observed amplitudes and fluids present.

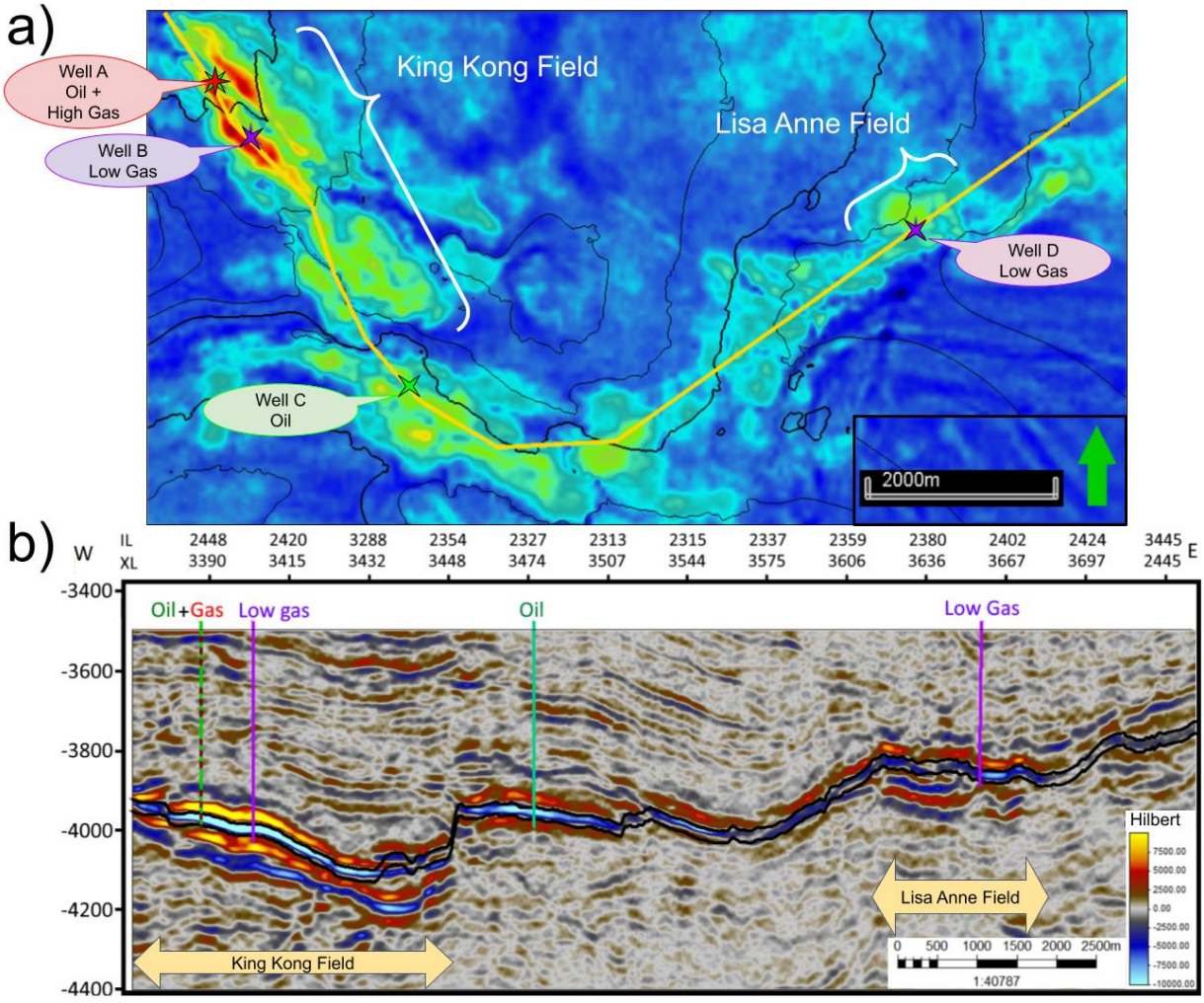

Figure 2-1: a) Most negative Hilbert transform amplitude map extracted between the top and base of the reservoir. Notice the yellow line showing the path of the arbitrary line shown below. **b)** Arbitrary line cross-section of Hilbert transform attribute crossing through King Kong and Lisa Ann fields. Notice the two black horizons mapping the top and base of the main top reservoir. Well paths are color coded to highlight the fluid present and their respective locations.

DATA

Several wells are analyzed, including Ursa Well #1 from the Ursa Field and Wells A, B, C, and D from the King Kong and Lisa Anne Fields (see Table 1). Well data includes the top and bottom hole locations, deviation surveys, checkshots, production history, and a full suite of logs; although producing intervals contained digital logs, while dry holes contained raster logs. The Enverus final reports, other well reports, and production history confirmed the lack of economic saturation in Well B and Well D in the KKLA area.

The King Kong and Lisa Anne Fields in the Green Canyon protraction are part of the 3D full-stack Green Canyon Phase II seismic survey collected in 1989. It is SEG positive polarity and has a bin spacing of 87.5 ft by 87.5 ft with a 4 ms sampling rate covering an area of 466 square miles (1208 km^2). This data cube representing 87.5 ft^2 of aerial extent and 4 ms of depth is defined as one voxel for the KKLA dataset. The voxel represents the location in the seismic volume and has one value for every attribute.

While it would be helpful to have access to angle stacks or gathers for our research, they are not publicly available. In their absence, we have developed a workflow that is just as valuable, if not more so. This workflow can be applied to full-stack seismic data, the most common seismic product available, making it a valuable tool for explorers and researchers. The presented methodology is comparable in usefulness to AVO analysis, considering it can differentiate between gas and oil during exploration. This tool allows researchers and interpreters to make significant strides without angle stacks or gathers. The methodology would also be even more successful with newer, higher resolution seismic data, and AVO attributes additionally included as training features.

METHODS

This Chapter aims to leverage the labeled data from the reservoirs in Ursa Well #1 and the attributes developed in Chapter 1 to design effective supervised machine learning models capable of accurately predicting fluid classes in an expanded area around Ursa Well #1 and the KKLA wells. Normalizing the amplitudes of both seismic surveys is crucial before creating attributes for the new KKLA survey. Additionally, the newly created attributes of KKLA must be normalized individually to ensure that they fall within the range of the Ursa survey attributes. A min-max scaler transformation is applied to all attributes in the two datasets, ensuring that the transfer learning process is appropriate and the datasets are comparable.

The workflow builds upon Chapter 1 and is illustrated in Figure 2-2. Three different ML algorithms are selected and given the Ursa dataset frequency attribute suite as the training input for the models. All three models have their hyperparameters selected using the grid-search cross-validation method and set to produce an accuracy score from 70% to 90%. The explanative AI method, SHAP, is then used on the trained RF model to obtain information on how important each attribute is for classifying each fluid class. Finally, the model from each algorithm is used to predict in an expanded radius of Ursa Well #1 as a blind test. All models then predict in the KKLA dataset, where we quantitatively validated the model thanks to the variety of fluid classes encountered within the four wells.

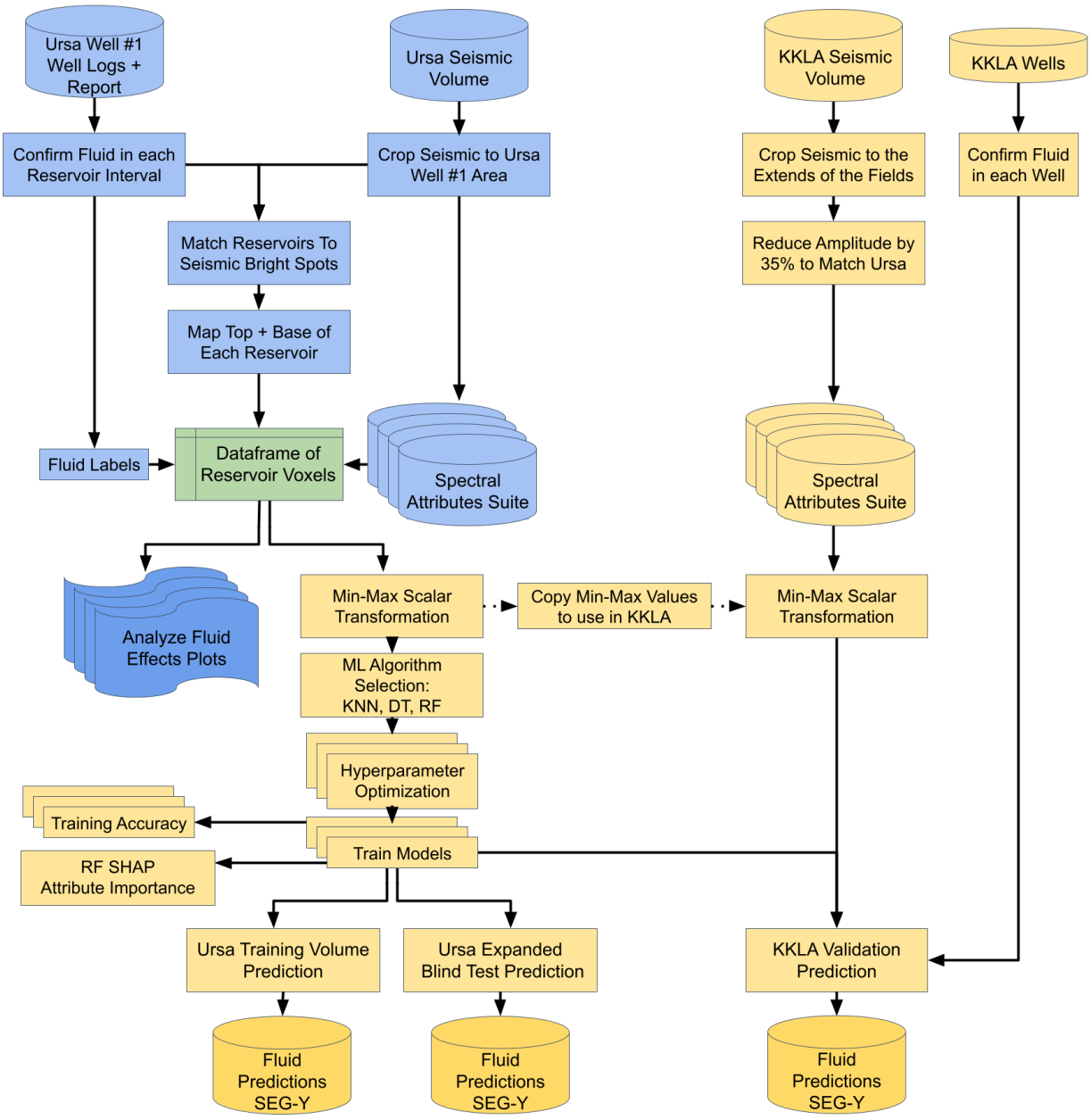

Figure 2-2: Workflow showing all the steps of this research. The uppermost left steps in blue are discussed in Chapter 1, where the fluid labels were used in the reservoirs of Ursa Well #1 to perform an in-depth attribute analysis. The sections in yellow are the new machine learning steps introduced in this chapter. The final output of this methodology is the fluid prediction results from the three algorithms in both the Ursa and KKLA datasets.

Step 1: Amplitude matching/normalization

The initial steps of this methodology attempt to make both datasets the most comparable to have successful results with the ML model predictions in the KKLA validation dataset. All frequency attributes are computed from the original seismic amplitude of the KKLA volume. This research found that the amplitude values of the reservoir bright spots in the KKLA dataset were almost twice as strong as those in the Ursa dataset. For this reason, the amplitudes must be normalized between the training and validation datasets. No perfect metric exists to directly compare the datasets because the positive and negative extreme amplitude values are typically disproportionate. This implies that perfectly matching the maximum amplitudes will create an imbalance in the minimum amplitudes and vice versa. The maximum and minimum values of the amplitudes in both datasets were similar enough when the amplitudes of the KKLA dataset were reduced by 35%, reducing the amplitude range difference in both datasets to a minimum. With this careful normalization, attribute creation for the KKLA dataset is completed following the workflow used for the Ursa seismic dataset.

Step 2: Attribute creation

From Chapter 1, it was interpreted that no single frequency attribute can distinguish the different fluids classes. The frequency suite analysis showed that every attribute could contribute to differentiating a fluid class or groups of fluid classes at a time. This observation proposes that the full suite of frequency attributes should be used to train the machine learning models. The same parameters were used in the KKLA dataset to produce the same frequency attributes already created for the Ursa dataset. As a quality check, each attribute's maximum and minimum values were compared to the Ursa datasets. Both dataset maximum and minimum values were observed

to be similar enough for comparison. Similar ranges were not observed when using the original KKLA amplitude volume for the attribute creation.

One benefit of using machine learning for this investigation is that there is seemingly no limitation on the number of attributes the algorithms can handle, as opposed to the limited use of three attribute comparisons in typical spectral decomposition analyses using the RGB display method. Some researchers might argue that using too many attributes can bring forth negative results as it might add analogous attributes that can bias the training and increase the runtime of the training and prediction steps. This research aims to test multiple algorithms and observe if any can of those algorithms overcome those limitations. Interpreters can only conjecture which attributes can be helpful in the prediction dataset during the transfer learning process. Finding an algorithm that does not require the reduction of attributes can significantly speed up the process and reduce uncertainty in attribute selection. This research also employs the explainable AI method, SHAP, to quantify the attribute importance of the entire frequency suite.

Step 3: Data conditioning

A crucial step of any machine learning workflow is data conditioning. Scaling the training data from 0 to 1 allows all attributes to exist in the same analytical space. The transformation function used here is a simple minimum-maximum "min-max" scalar. A common pitfall of this transformation is that it is highly susceptible to outliers. The erroneous outliers were removed in the Ursa training data set by limiting the voxels observed to those within the reservoir and near Ursa Well #1, reducing the possible interference from the salt contact.

The maximum and minimum values of the attributes in the KKLA dataset are not identical to those of the Ursa dataset. This imbalance implies that a min-max transformation of the KKLA dataset would make the ML algorithms "think" they are in the same analytical space. A transformed value of "1" in a particular attribute would represent different values in the two datasets. Modifying the min-max scalar transformation in the KKLA dataset controls the data scaling problem. The maximum and minimum values of the Ursa attributes are used as a new constraint for the value transformation in the KKLA dataset. The few newly transformed values below 0 and above 1 are clipped to be 0 and 1, respectively. This modification ensures that both datasets are now in the same analytical space.

Step 4: Algorithm selection

Multiple supervised machine learning algorithms can be trained to predict labels in a different dataset. Features are the variables used as input for the training and the predictions. The features in this research are the frequency attributes. The way the features are grouped to train the models depends on the ML algorithm selected. It is understood that as the accuracy and complexity of a particular algorithm increase, its interpretability decreases. The accuracy of three supervised machine learning algorithms will be tested in the Ursa Field before performing the validation predictions in the KKLA Field. The three algorithms to be tested are k-nearest neighbors (KNN), decision tree (DT), and random forest (RF). All three algorithms have a set of hyperparameters that will affect the model's training, and analyzing the training results help prove their fluid prediction reliability and sensitivity to noise.

The KNN model was created by Evelyn Fix and Joseph Hodges in 1951 for the US Air Force as a non-parametric classification method (Fix and Hodges, 1951). As the name implies, new data points are classified based on the majority labeled class in "K" neighboring points. Hyperparameters for KNN training include the number of neighboring points and the distance formula used. This research uses Euclidean distance; the only hyperparameter tested is the number of neighbors. In theory, the KNN model is the most likely to be affected by having too many features because an anomalous value of a single feature can change the prediction altogether. In practice, the KNN model should perform successfully if predicting in the same seismic survey as the training but has a higher chance of error in new seismic survey predictions.

The DT algorithm was introduced in 1963 by Morgan and Sonquistey, and it follows a top-down flowchart structure with multiple conditional "branches" with final classifications occurring at the bottom "leaves" (Morgan and Sonquistey, 1963). Compared to the KNN algorithm, there is a considerable increase in hyperparameters. Only the hyperparameters that have the most effect on the training will be tested within the scope of this research. The tested hyperparameters include the max depth of the tree, the minimum number of samples needed to split a "branch," and the minimum number of samples required for a final "leaf."

The RF algorithm was created by Leo Breiman when he added a bagging procedure to the DT algorithm (Breiman, 1996). Bagging involves running multiple iterations of DT with a randomized "bag" of features. Combining models from multiple iterations produces a very robust final RF model that is not entirely dependent on the "best" attributes and is less susceptible to overfitting. The hyperparameters in the RF model include those of the DT model. Extra hyperparameters are included that control the bagging. The bagging hyperparameters are the number of iterations, and the number of features and samples included per iteration. In theory, the

RF model should be less susceptible to the drawbacks of using many features. It learns by running multiple DT iterations with a subset of the features and samples per iteration. The final classification boundaries are the averaged boundaries from each iteration. The bagging procedure suggests that the trained model can make accurate predictions with a subset of the features and better compensate for noise or anomalous values.

Step 5: Grid search + cross-validation to train models

All three algorithms (KNN, DT, RF) underwent multiple iterations of grid search and cross-validation to fine-tune hyperparameters. Grid search is a technique where the model tests through multiple ranges of hyperparameters while only changing a single value at a time. This method is performed to find the optimal hyperparameters to create a robust model that avoids overfitting. Overfitting can occur if the hyperparameters become too optimal, resulting in "memorizing" rather than "learning" from the data. Overfitting in training would lead to high accuracy in the training dataset and unsatisfactory results in the expanded Ursa blind test and the KKLA validation test, where new data points are presented. A combination of hyperparameters that result in 70% - 90% accuracy is selected to avoid overfitting.

Cross-validation is the process of making a subset of the dataset to train and a subset to validate the model. While the training dataset might seem small because it only contains one instance of a LGS reservoir in the Ursa dataset, the reservoir is thick enough that the investigation area produces thousands of voxels used for the training. The number of samples still does not make it a vast dataset, so a 5-fold cross-validation is applied during training. Five-fold cross-validation sets aside 20% of the data points to validate, and this is repeated four times with the remaining

80% of data points. Cross-validation and grid search allow for the creation of a model with high accuracy that does not overfit while saving time in the otherwise manual task of fine-tuning the hyperparameters.

Step 6: SHAP

The explainable AI method, SHapley Additive exPlanations (SHAP), can increase the RF model's interpretability. It was created in 1951 for economic analysis and uses a game theory approach to give quantitative results on the importance of each feature (Shapley, 1951). The relative importance of each feature is measured by removing features one at a time and checking the model's accuracy. SHAP can be applied to the RF model since it already learns by removing attributes in every iteration. The added benefit of SHAP is that it can explain the training of the RF model and give an attribute importance list for each fluid classification. Furthermore, it can address if a specific attribute's high, low, or average values lead to the classification of each fluid class. This method allows the study to understand further which frequency suite attributes can differentiate gas saturations.

Step 7: Ursa blind test – model validation in KKLA

Based on previously mentioned constraints, the best model of each of the three algorithms is blind tested around an expanded area of Ursa Well #1 to check for accuracy and its potential to overcome seismic noise. The expected result is that the area of each expanded reservoir is mostly predicted as the same fluid the innermost area was labeled with during training. Misclassification is likely to occur where the salt body is present at the most western extent. Another expected result

of the Ursa blind test would be that fluid classification changes occur at possible fluid contacts and be perceived as flat spots. Credibility in the model would improve if flat spot observations coincided with correct fluid density stacking order, meaning oil lays below gas and above water.

The model from each algorithm is used to predict fluids in the KKLA dataset and validate our models with the four wells present in the area. A classification of "Oil" or "HGS" is expected for Well A, "LGS" for Well B, "Oil" for Well C, and "LGS" for Well D (Table 1). The "Water" and "Non-Reservoir" classifications are expected outside the reservoir horizon. Due to the nature of the training dataset, "Water" will likely be predicted in continuous reflectors of moderate amplitude, while "Non-Reservoir" would be shales and salt bodies. Images of the predicted results in an arbitrary line passing through all wells and a horizon map will be used to quantify the models' predicting ability.

RESULTS

The results section will cover the details of the training of the machine learning algorithms, including the quantity of data points per fluid class and hyperparameters for each model. The training predictions in the Ursa Field will be observed in perpendicular cross-sections through Ursa Well #1. The confusion matrix created from the training results quantifies how accurate each model is at predicting the correct fluid at each reservoir interval. The SHAP values for the RF model will quantify the importance of each attribute from the frequency suite (see Chapter 1) and measures its SHAP Value contribution to identifying each fluid class. The results of the blind test predictions in the expanded Ursa volume will illustrate how each model handles the uncertainty of the new data points further away from Ursa Well #1. Although no validation with well data is performed in the Ursa expanded volume blind test, various fluid relationships that provide confidence in the

ML models' ability to predict fluid changes within each reservoir can be observed. Finally, the validation of the three ML models is tested in the KKLA survey, matching the prediction results with the production data of the four wells. The successful identification of fluids within the reservoirs in the KKLA dataset brings validity to the use of supervised ML models, along with the frequency attribute suite, to be used in the derisking stage of prospects in the Gulf of Mexico.

Label distribution before training

An essential aspect of using supervised machine learning is diminishing bias during training. Bias is reduced by balancing the number of data points representing each class. The labeled reservoirs in the 9 by 14 lines area in the Ursa training volume yield an unbalanced number of data points per class, as shown in Figure 2-3. The initial dataset is represented in Figure 2-3a and exhibits an over-representation of oil data points, leading to the oil class being over-classified in previous validation tests. The removal of two oil horizons (Oil-3 and Oil-5) makes a more realistic distribution, as seen in Figure 2-3b. The non-reservoir data points in Figure 2-3b are the most represented class, which is expected to represent most of the classification results in the KKLA validation from a geologic standpoint.

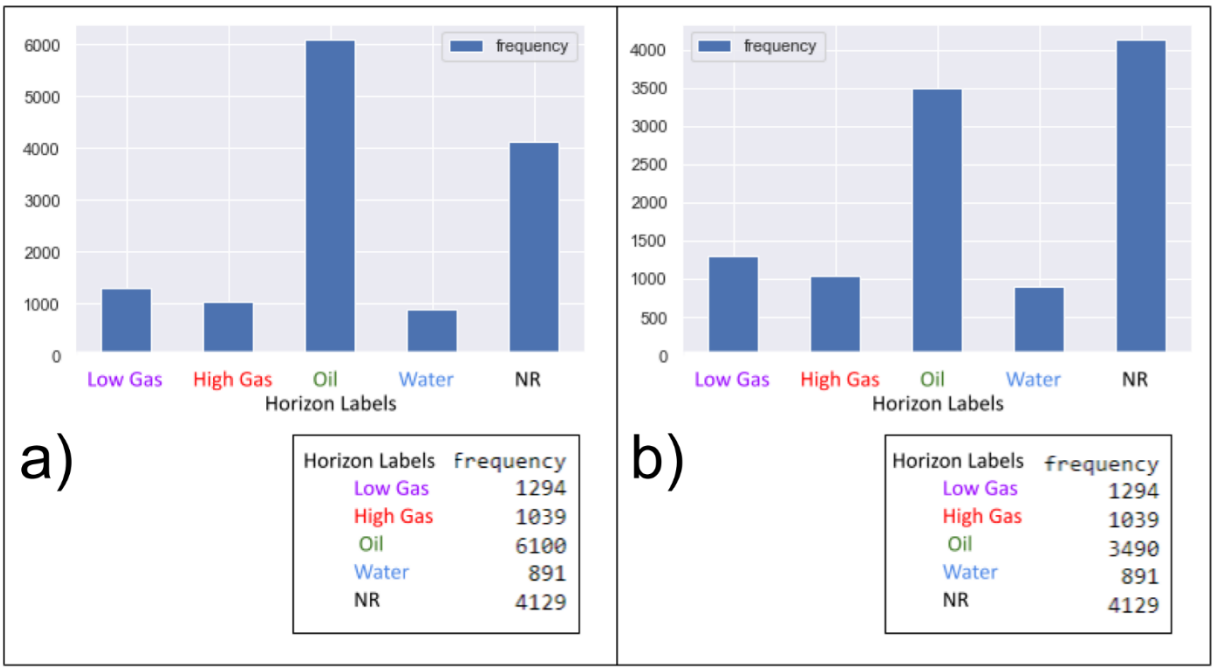

Figure 2-3: The histogram and voxel count (frequency) for each labeled fluid class in the Ursa dataset training volume. **a)** Original histogram using all the horizons in Ursa Well #1. Notice how the oil label is more representative of the whole volume than the non-reservoir facies. **b)** Histogram of the classes after removing the Oil-3 and Oil-5 horizons from the training data. It can be observed that the non-reservoir label is the predominant fluid class.

Hyperparameter selection and confusion matrix of training results

Hyperparameter selection can be one of the most time-consuming tasks while training a ML algorithm. The grid-search cross-validation method helped narrow down the search for ideal hyperparameters. Hyperparameters were fine-tuned to produce a model with higher than 70% macro average accuracy but not higher than 90% so as not to have an overfitted model. The final hyperparameters and training results of the final model of all three algorithms are summarized in Figure 2-4. The top row shows KNN, medium row DT, and RF in the bottom row. The left column displays the hyperparameters, the center column displays the confusion matrix, and the right column displays the classification report.

Observing the length of the hyperparameter list emphasizes each algorithm's complexity and indicates a longer processing time during the grid search cross-validation process. The confusion matrix in the middle column displays how each class was misclassified; the vertical axis indicates the true class, while the horizontal indicates the prediction. Misclassifications of one class can occur evenly across all other classes or into a particular class. The pattern of misclassification is similar in all three algorithms to varying degrees. Water and non-reservoir classes cross-misclassify each other, which is substantial for the water class in DT. HGS and LGS do not get misclassified with each other, but both tend to be misclassified as oil. Oil, to some degree, is misclassified into non-reservoir and less into the two gas classes.

The classification report on the rightmost column gives quantitative measurements representative of the confusion matrix. Precision measures the percentage of predicting the actual class against other classes, recall measures the correct predictions against the actual classification, and the F-1 score measures the weighted harmonic average of precision and recall percentages (Manning, 2008). The support column indicates how many data points were used in each class. The summaries at the bottom of the report measure the total accuracy, macro averages, and supporting data points for the entire training dataset. The accuracy measures the total amount of correct predictions, while the macro average weights the results based on the supporting data points of each fluid class. The macro average highlights a more reliable training score considering that not all classes have the same quantity of data points.

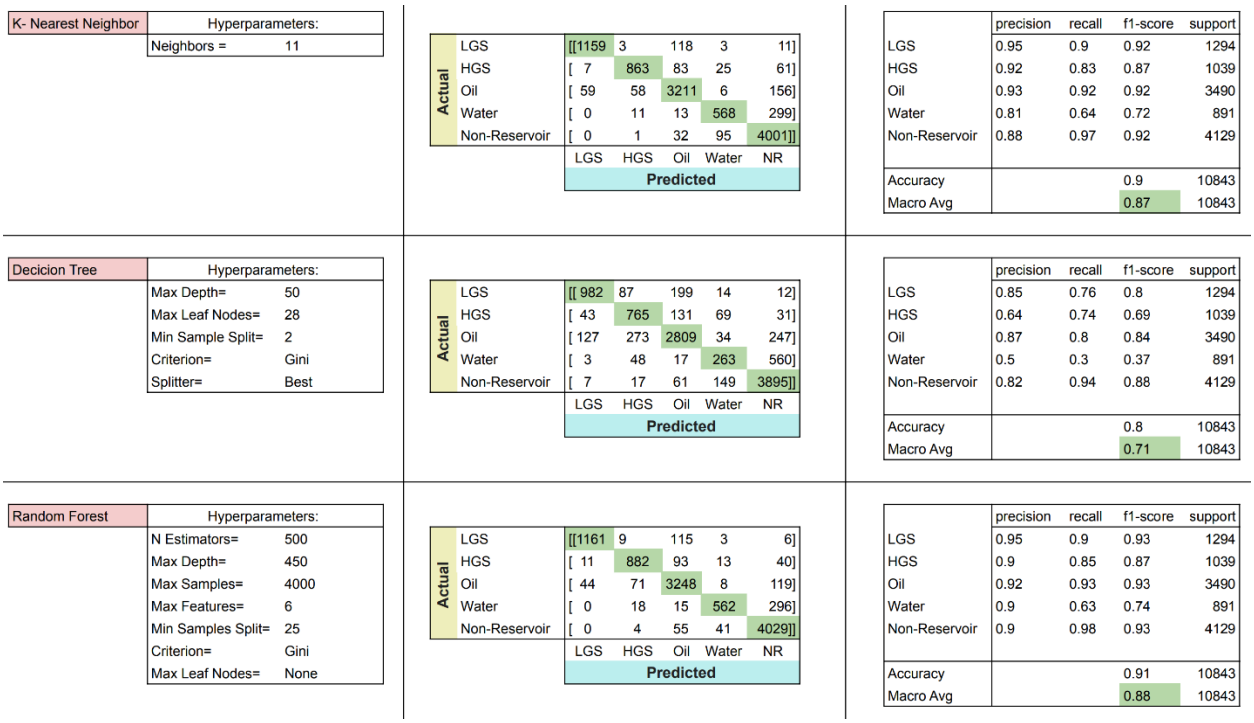

Figure 2-4: The hyperparameters and training results for the best model of each algorithm. The first row shows results for k-nearest neighbors, the second row shows decision tree, and the third row shows random forest. The first column shows hyperparameters, the second column the confusion matrix, and the third column shows the training report.

Random forest SHAP values

The relative attribute importance during training can be extracted when applying SHAP to the RF training model. SHAP measures contribution using a unique unit called SHAP Value. The general attribute importance is measured in Mean SHAP Value (MSV), and their ranking is presented in Figure 2-5. The attributes at the top of Figure 2-5 are the most effective at separating the different fluid classes in the Ursa dataset. The most critical attribute is average frequency at 0.3 MSV, followed by medium-low frequency magnitudes (8 Hz – 14 Hz) at ~0.19 MSV. The high (18 Hz - 30 Hz) and low (4 Hz and 6 Hz) frequency magnitudes have an average level of importance at ~0.075 MSV. Peak frequency, instantaneous frequency, and the 50 Hz frequency magnitude share similar importance at ~0.055 MSV. The remaining attributes of bandwidth, mean

frequency, kurtosis, skewness, roughness, and slope have continuously less importance with values from 0.045 to 0.02 MSV.

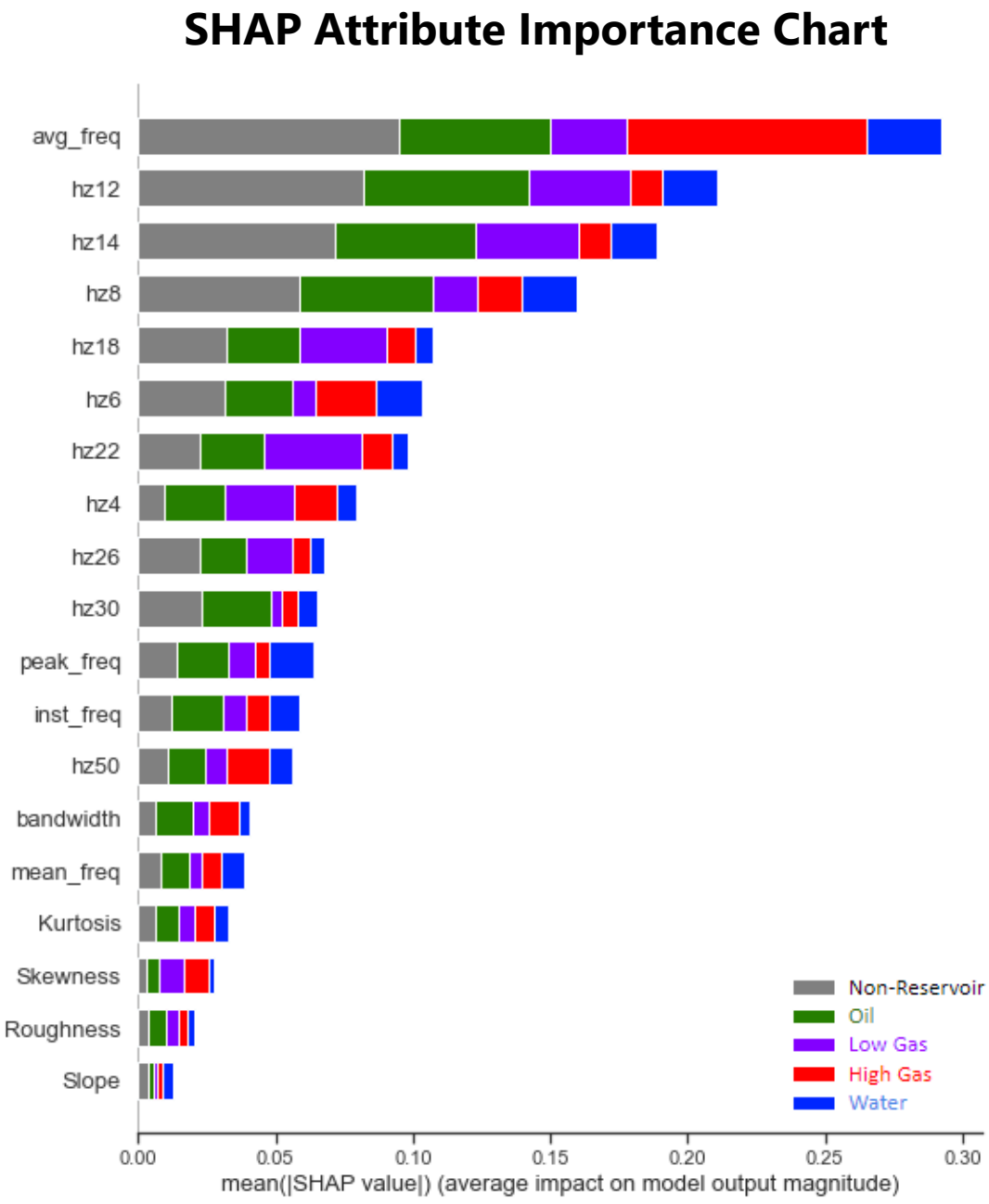

Figure 2-5: All attributes used for training the random forest model are sorted in relative importance from top to bottom according to Mean SHAP Values (MSV). The colors represent the percentage that each fluid class contributed to each attribute's total importance.

A more straightforward way to observe how each attribute contributes to the selection of each class can be seen in the "per class" SHAP values plots in Figure 2-6. Each graph in Figure 2-6 represents one class; the vertical axis breaks it down by attribute, and the horizontal axis indicates contribution potential in SHAP values. The color of the data points represents high and low attribute values (red and blue, respectively). The contribution potential is more favorable the more to the right the points are, and more unfavorable the more to the left the points are. For example, the red points located farther to the right in the plot indicate that high values of that attribute lead to the classification of that class. Attributes with a short spread of points indicate that they will have little contribution in the final choice for the classification regardless of high or low values in the said attribute.

Observing the HGS class in Figure 2-6 shows that high values of average frequency and low-frequencies magnitudes (4 Hz – 8 Hz) lead to a strong positive contribution. In contrast, low values of the highest frequency magnitude (50 Hz) lead to a strong negative contribution. Average bandwidth values lead to a medium positive contribution. Regarding spectral shape attributes, low skewness, kurtosis, and slope values lead to a weak positive contribution, while low values of roughness lead to a weak negative contribution.

Observing the LGS class shows that high values of medium-frequency magnitudes (12 Hz - 22 Hz) have a strong positive contribution, while low values of 4 Hz magnitude lead to a strong positive contribution. Medium values of 6 Hz and 8 Hz have a medium positive contribution, low bandwidth values lead to a medium-low positive contribution, and medium to high values of all four spectral shape attributes lead to a weak positive contribution.

The final hydrocarbon class to observe is oil, highlighted for its preference for high-frequency magnitudes. High values of high frequency magnitudes (26 Hz – 50 Hz) lead to strong

positive contributions. Medium values of the low frequencies (4 Hz – 12 Hz) lead to medium positive contributions. Low values of all four spectral shape attributes lead to a weak positive contribution. Bandwidth has a low contribution and no attribute value associated in any direction.

The water class has positive contributions for low magnitudes of all frequencies, with 50 Hz having the most substantial positive contribution with the low values. High bandwidth has low contributions in both negative and positive directions. High Instantaneous frequency values lead to a strong positive contribution, unlike gasses and non-reservoir classes. High slope and roughness values lead to a medium positive contribution, while positive skewness leads to a weak positive contribution. Average kurtosis values lead to weak positive contributions.

The non-reservoir class shows very similar results to the water class. Low magnitudes of all frequencies lead to a positive contribution except for 50 Hz, which leads to a strong negative contribution. Bandwidth is identical to water in that no value leads in a particular direction. Regarding spectral shape attributes, high skewness, roughness, and slope values lead to a weak negative contribution, while low values of roughness lead to an even weaker negative contribution.

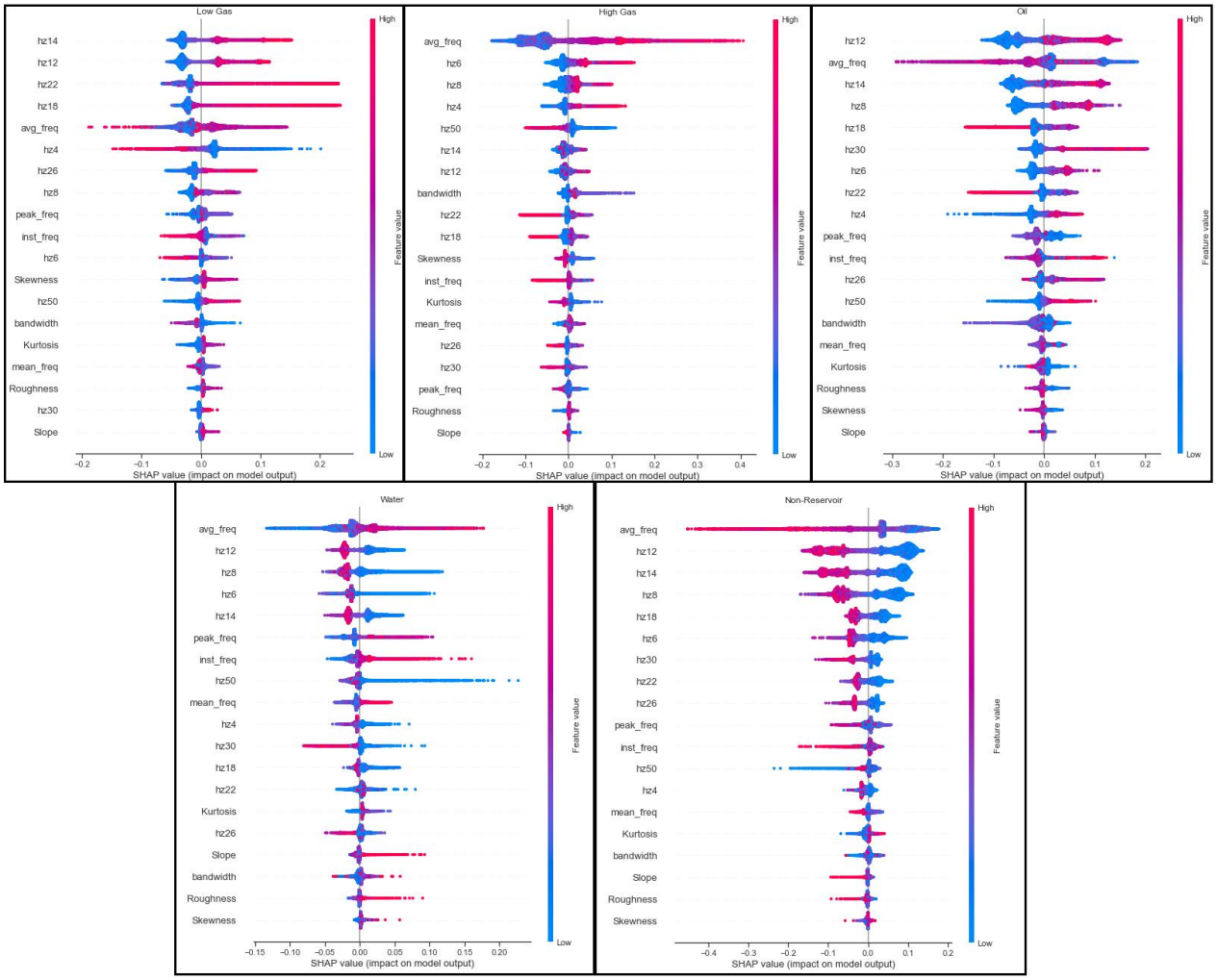

Figure 2-6: Attribute importance list based on SHAP values for each fluid class. The vertical axis for each graph lists the attribute importance in descending order from top to bottom. The horizontal axis indicates the SHAP values and is centered at zero. Positive SHAP values contribute positively to the classification, while negative SHAP values point to a negative contribution. Contributions become more significant the father away the SHAP value is from zero. The color bar assists in observing each attribute's high and low values and whether they have positive or negative SHAP values.

Ursa cross-sections of training results for each algorithm's model

Cross sections are used to observe the predictions' results in the Ursa training volume and the expanded Ursa blind test volume. A map view showing the path of the three cross-sections used is shown in Figure 2-7. Arbitrary Line 1 (AL1) represents a dip direction line passing through the training well, while Arbitrary Line 2 (AL2) represents the strike direction like passing through the well. A particular dip direction cross-section passing 600 feet north of the well that shows interesting results is presented in Arbitrary Line 3 (AL3).

The following images will show the training and expanded blind test results of the Ursa Field for all three algorithms (KNN on the left, DT in the middle, and RF on the right columns). The dip direction cross-section passing through Ursa Well #1 (AL1) displaying the prediction results in the training volume is shown in Figure 2-8. The predictions are similar for all three algorithms and highlight the training's high macro average accuracy (>70%). The KNN and RF predictions look nearly identical. In contrast, the DT predictions stand out by having a noticeable amount of mislabeled voxels within the orange boxes in the HGS, Non-Reservoir, and Oil-2 horizons that are not present in the other models' training results. A strike direction cross-section passing through Ursa Well #1 (AL2) in the same training volume is presented in Figure 2-9 with similar observations.

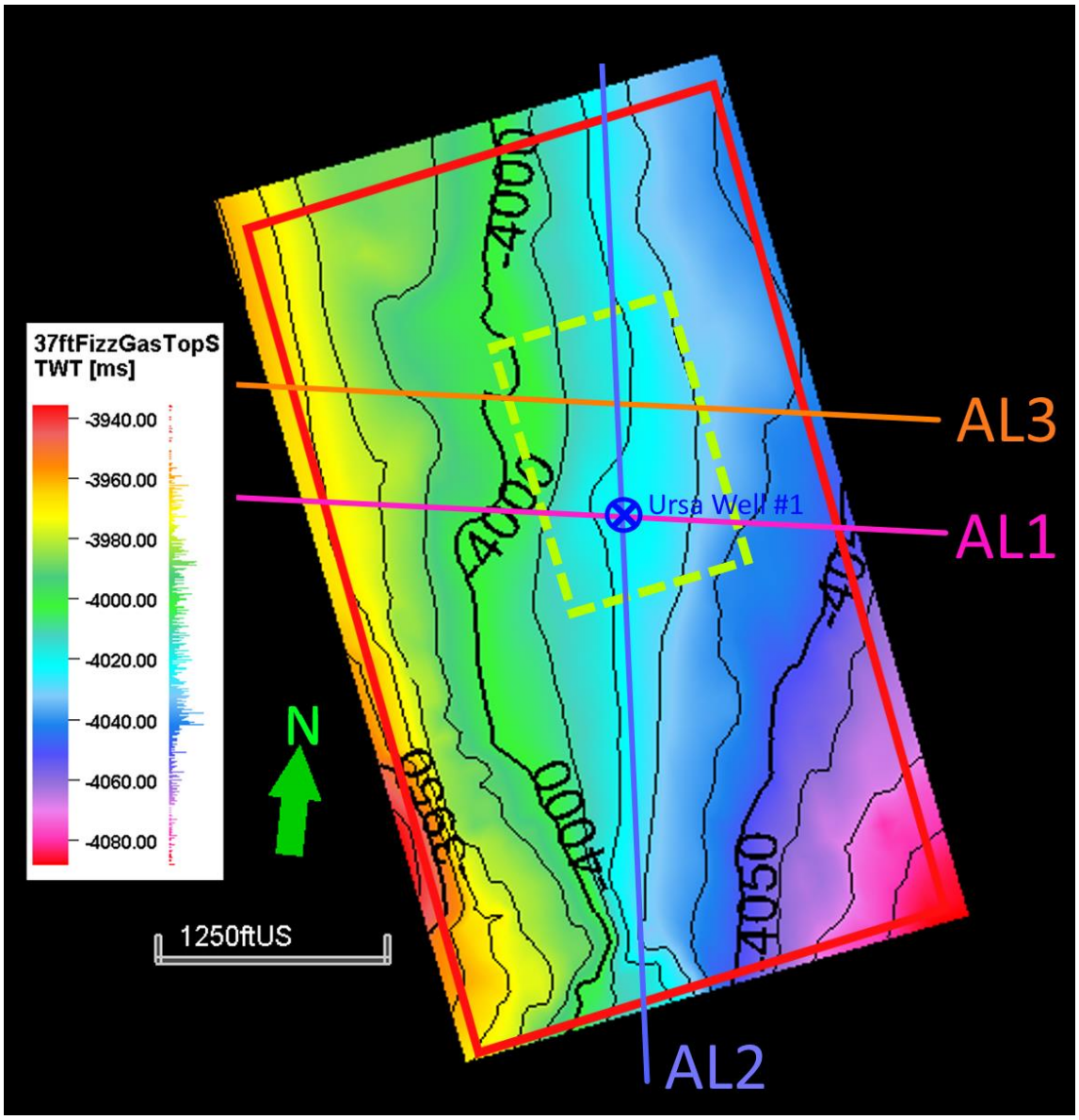

Figure 2-7: Structure contour map of the uppermost reservoir in Ursa Well #1, representing the LGS reservoir. The location of Ursa Well #1 is marked by a dark blue X. The yellow dashed box represents the extent of the training volume, while the red box represents the area of the expanded Ursa blind test volume. Notice how the training area in dashed yellow is centered on keeping the same time-depth. The three cross-sections shown in this study are highlighted as AL1 (Dip Direction), AL2 (Strike Direction), and AL3 for noteworthy observations in the dip direction.

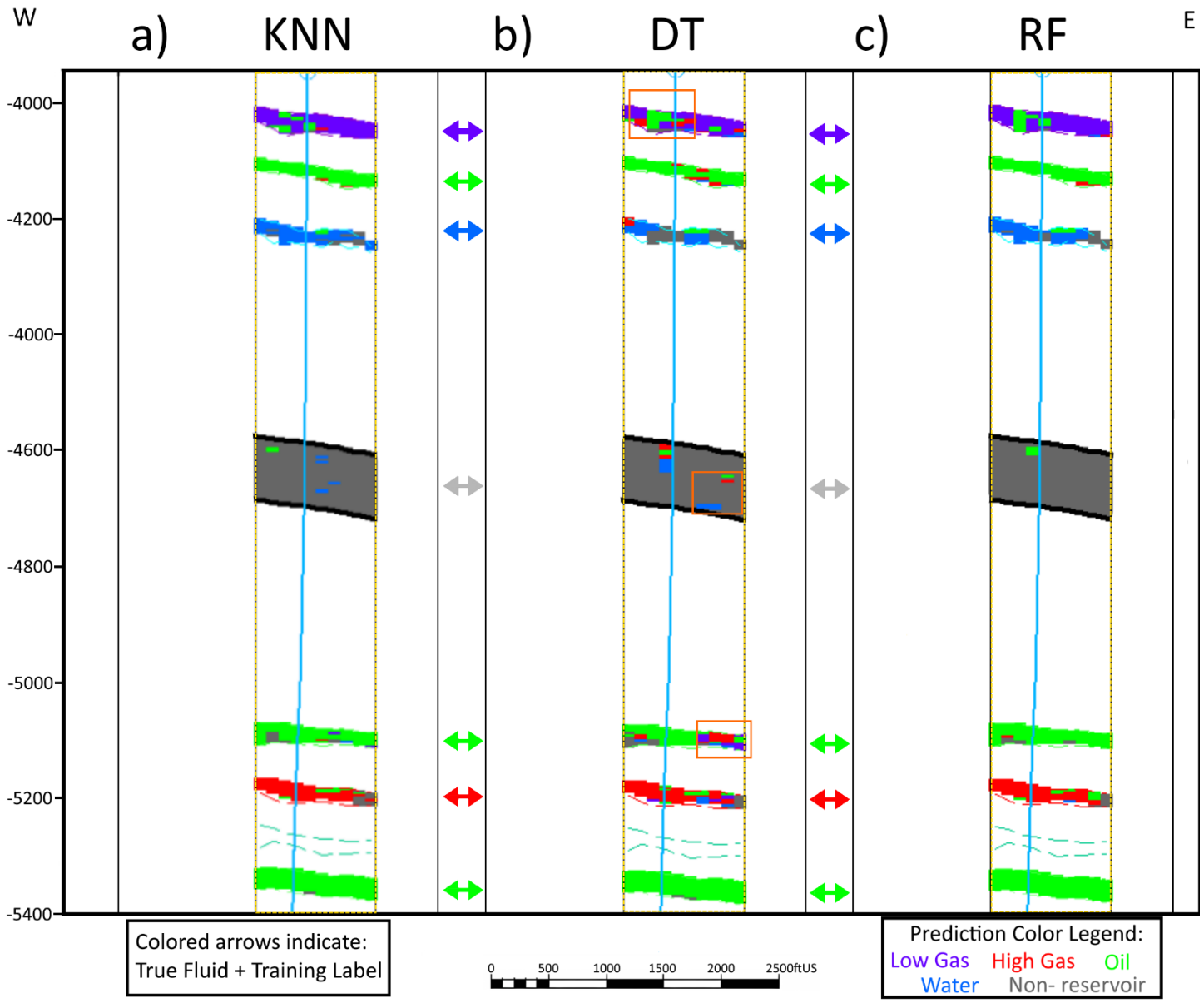

Figure 2-8: AL1 cross-section in the dip direction passing through Ursa Well #1 (light blue well path). Prediction results for the training volume are shown with the respective colors for each fluid class. Fluid class color-coded arrows indicate the fluid class each horizon was labeled with during training.

a) K-nearest neighbor model predictions.
b) Decision tree model predictions**.**
c) Random forest model predictions. Orange box points to misclassified voxels that are more prominent in the DT model than in other models.

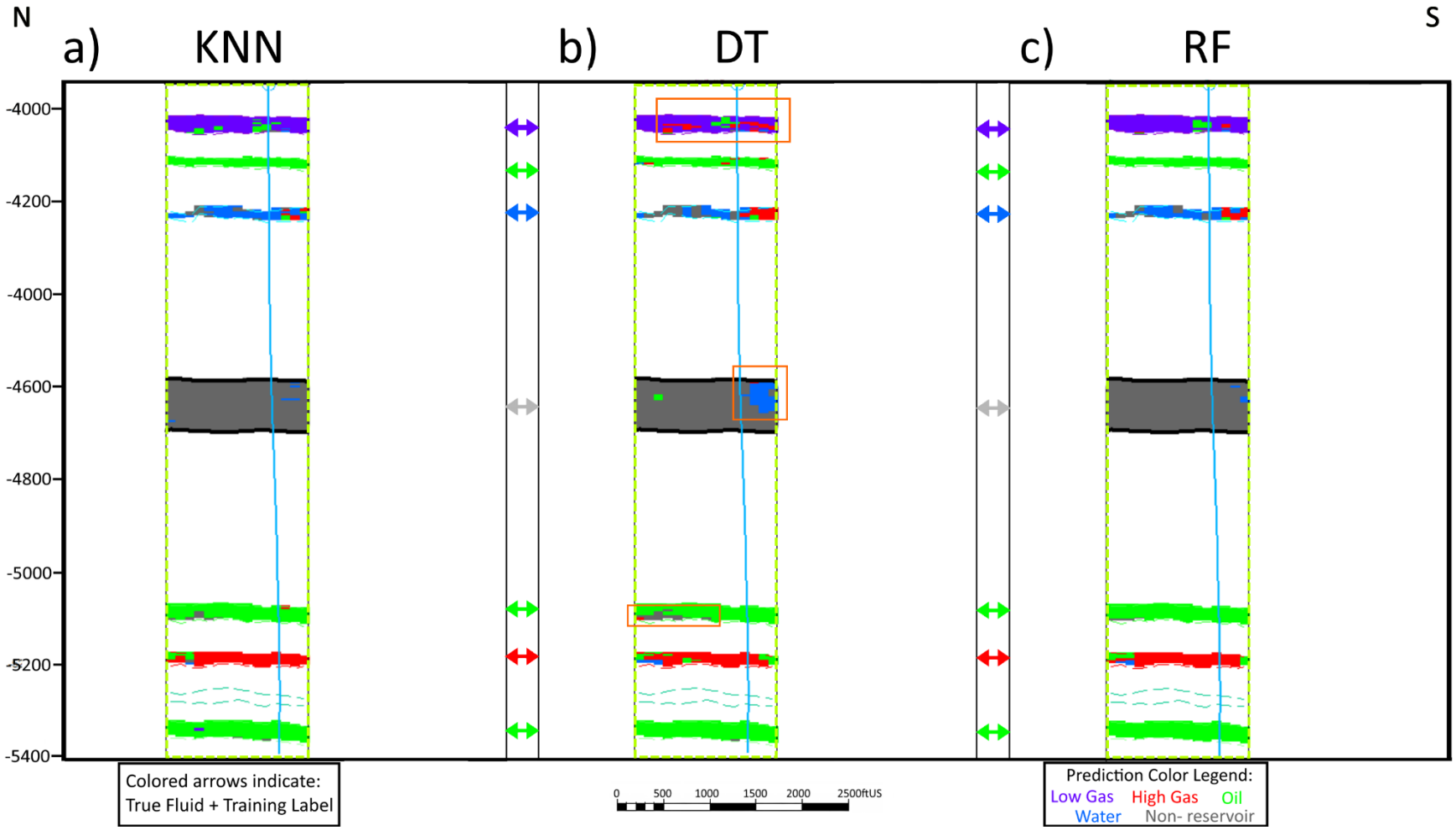

Figure 2-9: AL2 cross-section in the strike direction passing through Ursa Well #1 (light blue well path). Prediction results are shown with the respective colors for each fluid class. Fluid class color-coded arrows indicate the fluid class each horizon was labeled with during training. **a)** K-nearest neighbor model predictions. **b)** Decision tree model predictions. **c)** Random forest model predictions. Orange box points to misclassified voxels that are more prominent in the DT model than in other models.

Ursa cross-sections of expanded ursa blind test results for each algorithm's model

The blind test in the expanded Ursa volume that predicts outside of the training area can be seen in Figures 2-10 and 2-12, with the inscribed yellow dashed box representing the extent of the training volume. Correct fluid predictions matching the training data are observed for all three models along the well path in the dip direction cross-section (AL1) of Figure 2-10.

The highest error along the well path occurs at the LGS horizon, where some voxels are misclassified as HGS or oil for all three models (see orange arrows in Figure 2-10). The Oil-1 horizon is mainly predicted correctly for the three models and exhibits some gas classification closer to the top of the reservoir, both up-dip and down-dip from the well (see dark green arrows 1 in Figure 2-10). The water horizon is distinct as a minor fault is located to the east, creating a disconnection between its sand body (see dark blue arrows 1). The water horizon is predicted to have high gas saturation across the fault down-dip (blue arrows 2) and hydrocarbon presence above the water in the up-dip direction from the well (blue arrows 3). The Non-Reservoir horizon is classified mainly as non-reservoir and some water as expected, with hydrocarbon classification halfway up-dip (dark grey arrows). Oil-2 horizon has some classification of HGS down-dip to the east (dark green arrows 2) and LGS and non-reservoir up-dip to the west (dark green arrows 3). The HGS horizon is mostly classified correctly, with a few predictions of oil in both directions and a distinct water and non-reservoir classification at the most western extent (marron arrows). The final Oil-4 horizon is mostly classified correctly as oil, with a distinct classification of HGS up-dip to the west (dark green arrows 4). All previous observations are consistent among the three models, differing slightly in the extent of each fluid prediction.

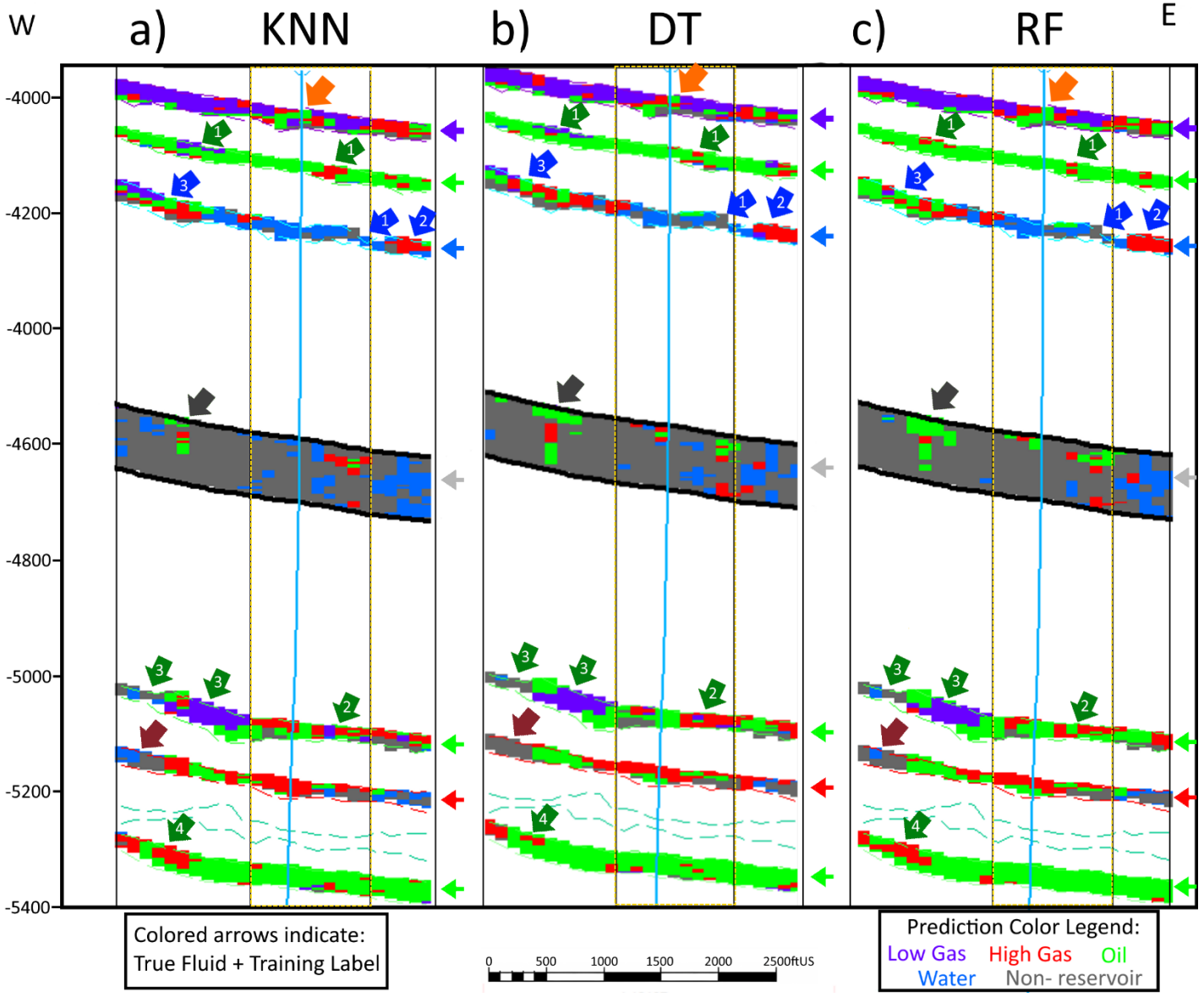

Figure 2-10: AL1 cross-section in the dip direction passing through Ursa Well #1 (light blue well path). Prediction results for the expanded blind test volume are shown with the respective colors for each fluid class. Fluid class color-coded arrows indicate the fluid class each horizon was labeled with during training. The yellow dashed box shows the extent of the training volume **a)** K-nearest neighbor model predictions. **b)** Decision tree model predictions. **c)** Random forest model predictions.

The strike direction cross-section through the well (AL2) for the previously described predictions in the expanded Ursa volume blind test is presented in Figure 2-11. The DT and RF predictions show a thin underlying layer of oil at the base of the reservoirs in both the LGS and HGS horizons (black arrows). Small patches classified as gas are observed at the top of the Oil-1 and Oil-4 horizons (marron arrows). From this perspective, it can be more easily observed that DT and RF models classify anomalies more homogeneously around an area (orange box). In contrast, KNN tends to have more heterogeneous predictions at the voxel scale (orange box).

A particular dip direction cross-section passing 600 feet north of the well (AL3) is shown in Figure 2-12. The well path is projected; therefore, the predicted fluids observed cannot be confirmed. A distinct flat and horizontal separation of LGS and oil is seen in the LGS horizon towards the east of the volume (orange box). This flat horizontal separation is easily seen in the DT and RF models. The water horizon shows the classification of HGS and oil across the minor fault in the down-dip direction (dark blue arrows 2) and some classification of HGS in the up-dip direction (dark blue arrows 3). The HGS horizon can be seen mainly classified as HGS with small areas classified as oil (black arrows 1) and a noticeable area of non-reservoir in the down-dip east edge of the volume (black arrows 2). The Oil-4 horizon is mainly classified as oil, but in the up-dip direction, all the algorithms predict a HGS patch with a nearly flat bottom (dark green arrows). The presence of the salt structure can be seen in the bottom three reservoirs towards the west, where portions are classified as non-reservoir (maroon arrows).

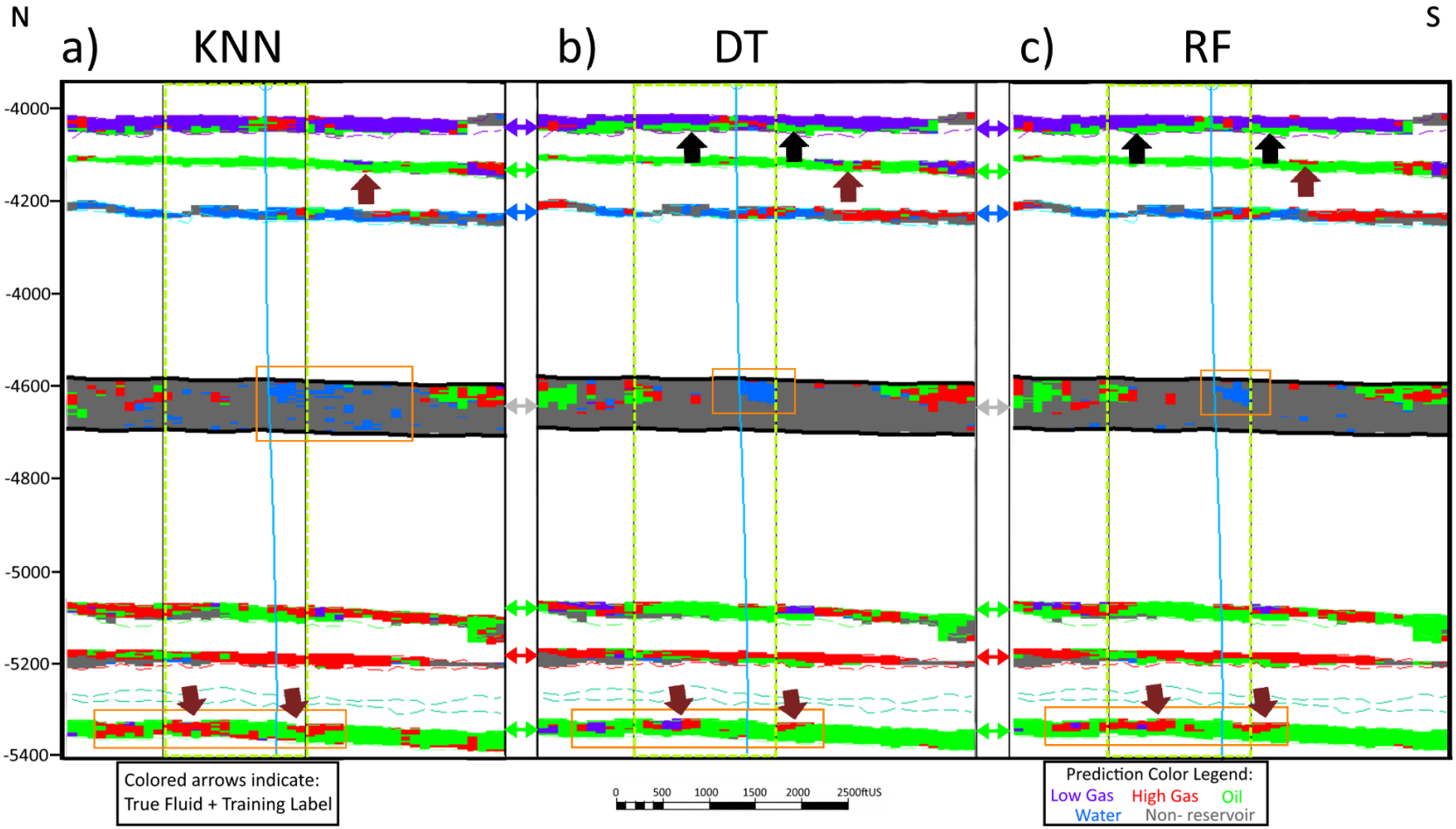

Figure 2-11: AL2 cross-section in the strike direction passing through Ursa Well #1 (light blue well path). Prediction results for the expanded blind test volume are shown with the respective colors for each fluid class. Fluid class color-coded arrows indicate the fluid class each horizon was labeled with during training. The yellow dashed box shows the extent of the training volume **a)** K-nearest neighbor model predictions. **b)** Decision tree model predictions. **c)** Random forest model predictions.

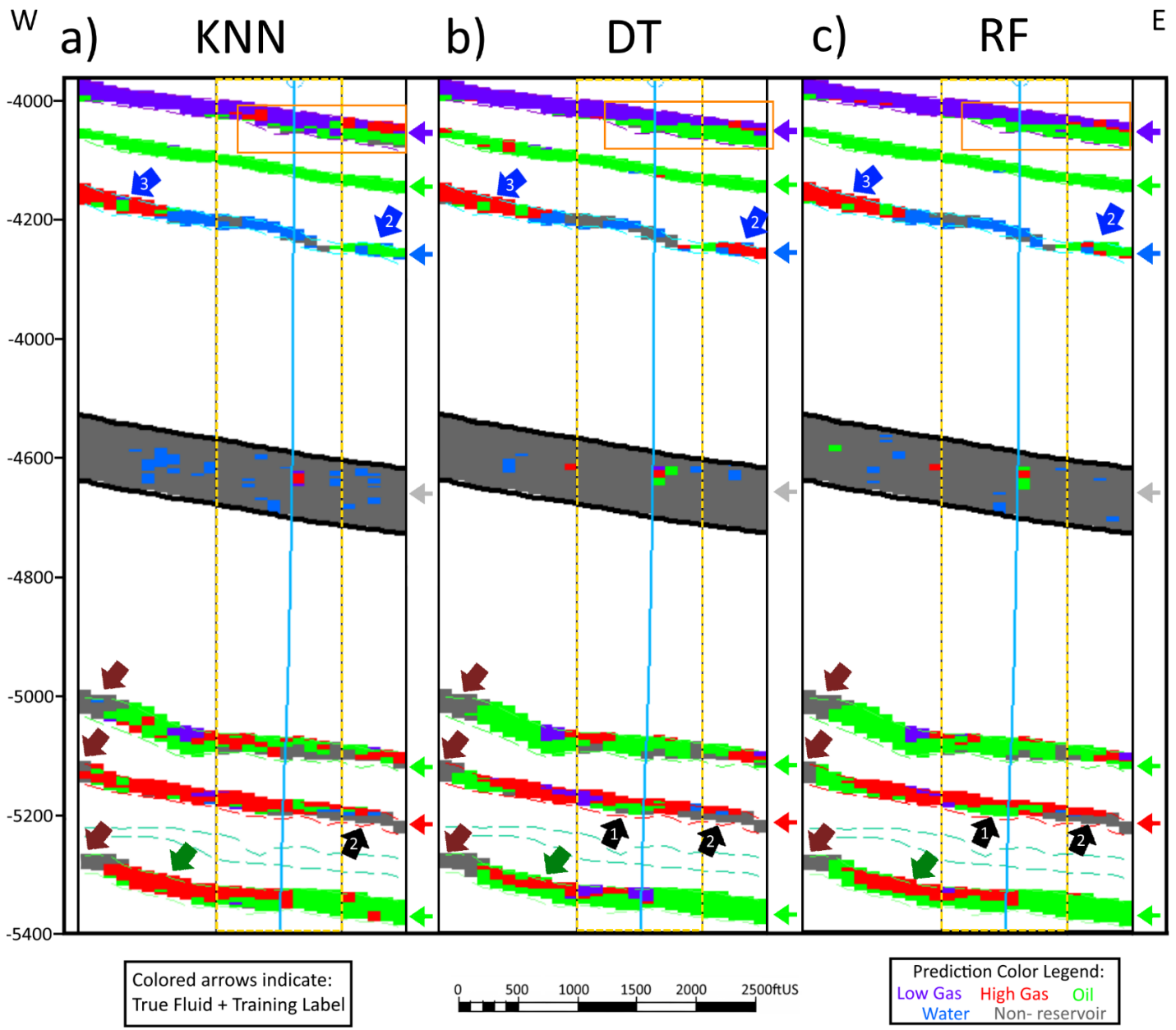

Figure 2-12: AL3 cross-section in the strike direction passing 600 feet north of Ursa Well #1 (projected - light blue well path). Prediction results for the expanded blind test volume are shown with the respective colors for each fluid class. Fluid class color-coded arrows indicate the fluid class each horizon was labeled with during training. The yellow dashed box shows the extent of the training volume **a)** K-nearest neighbor model predictions. **b)** Decision tree model predictions. **c)** Random forest model predictions.

3D Visualization of the Ursa expanded volume blind test predictions of each algorithm's model

A 3D view of the predictions from the Ursa expanded blind test volumes are shown in Figure 2-13 to remark on the algorithms' reliability within a geological context. Inline 2924 and crossline 33140 displaying the Hilbert transform of the volume are shown in the background to better frame the prediction results in Figure 2-13. The top set of reservoirs (LGS, Oil-1, and water) located around 12,000 feet sub-sea depth are shown in the top row(Figure 2-13 (1)). The second set of reservoirs (Oil-2, HGS, and Oil-4) located around 18,500 feet sub-sea depth are presented in the bottom row (Figure 2-13 (3)). The 100 ms thick shale section is shown in the center row (Figure 2-13 (2)). The northwest-facing view angle is sub-parallel to the dip direction of the reservoirs. A high-level observation for all three models is that the predictions through the well path are consistent with the fluid class used for the training of each reservoir. One can also observe that most of the predictions in each reservoir are consistent with the fluid class used for training each reservoir. Observations for each reservoir are presented in the following paragraphs, starting from the top reservoir and continuing deeper in sequence.

The flat spot transition from oil to LGS classification can be seen in all three models' LGS reservoir (Figure 2-13 (1)). A considerable amount of area is classified as water for the three models at the lowermost point of the LGS reservoir, just below the oil flat spot. A second area of water classification at the lowermost part of the reservoir can be seen for the Oil-1 reservoir, located right below the LGS reservoir (Figure 2-13 (1)). A significant difference between the models' predictions occurs in a gas patch southwest of the well within the Oil-1 reservoir. KNN and DT classify this gas patch as LGS (Figure 2-13 (1a-1b)), while RF classifies it as HGS (Figure 2-13 (1c)).

The water reservoir shows a fluid transition from water to HGS in the up-dip western direction for all three models (Figure 2-13 (1)). The KNN model shows the transition happening further up-dip and further west. The hydrocarbon classified area found on the south side of the minor fault in the water reservoir is also different for all three models. The KNN model classifies this area as oil (Figure 2-13 (1a)), while the DT model classifies it as HGS (Figure 2-13 (1b)). The RF model classifies this area as HGS to the south and oil to the north (Figure 2-13 (1c)). The non-reservoir shale section predictions are nearly identical for all three models (Figure 2-13 (2)). A key observation is that the KNN model has more heterogenous predictions of water along the interval (Figure 2-13 (2a)) compared to the DT and RF models (Figure 2-13 (2b – 2c)). All models show oil and HGS predictions to the western extent at the location of stronger amplitude reflections that would not be interpreted as shale in the original volume (Figure 2-13 (2)).

Continuing to the second set of deeper reservoirs observed by the well, one can observe nearly identical results from both the DT and RF models (Figure 2-13 (3b -3c)). The KNN model shows the more heterogeneous predictions (Figure 2-13 (3a)) described in the cross-section from Figure 2-11. The HGS predictions at the top of the Oil-2 reservoir previously observed in Figure 2-10 are seen from this perspective (Figure 2-13 (3)). This 3D view also shows the large anomalous prediction of LGS that occurs at the western extent of the Oil-2 reservoir that coincide with the strong anomalous reflections at the salt's edge (Figure 2-13 (3)). The HGS reservoir has nearly identical predictions for all three models, and the previously observed non-reservoir area from Figure 2-12 can be seen in the eastern extent. The deepest reservoir, Oil-4, shows predictions of HGS patches in all models. The two gas patches are more easily seen in the DT and RF models as they have a closely defined extent (Figure 2-13 (3b - 3c)). The KNN model exhibits HGS

predictions that occur as isolated voxels and obscure the observation of the two prominent patches (Figure 2-13 (3a)).

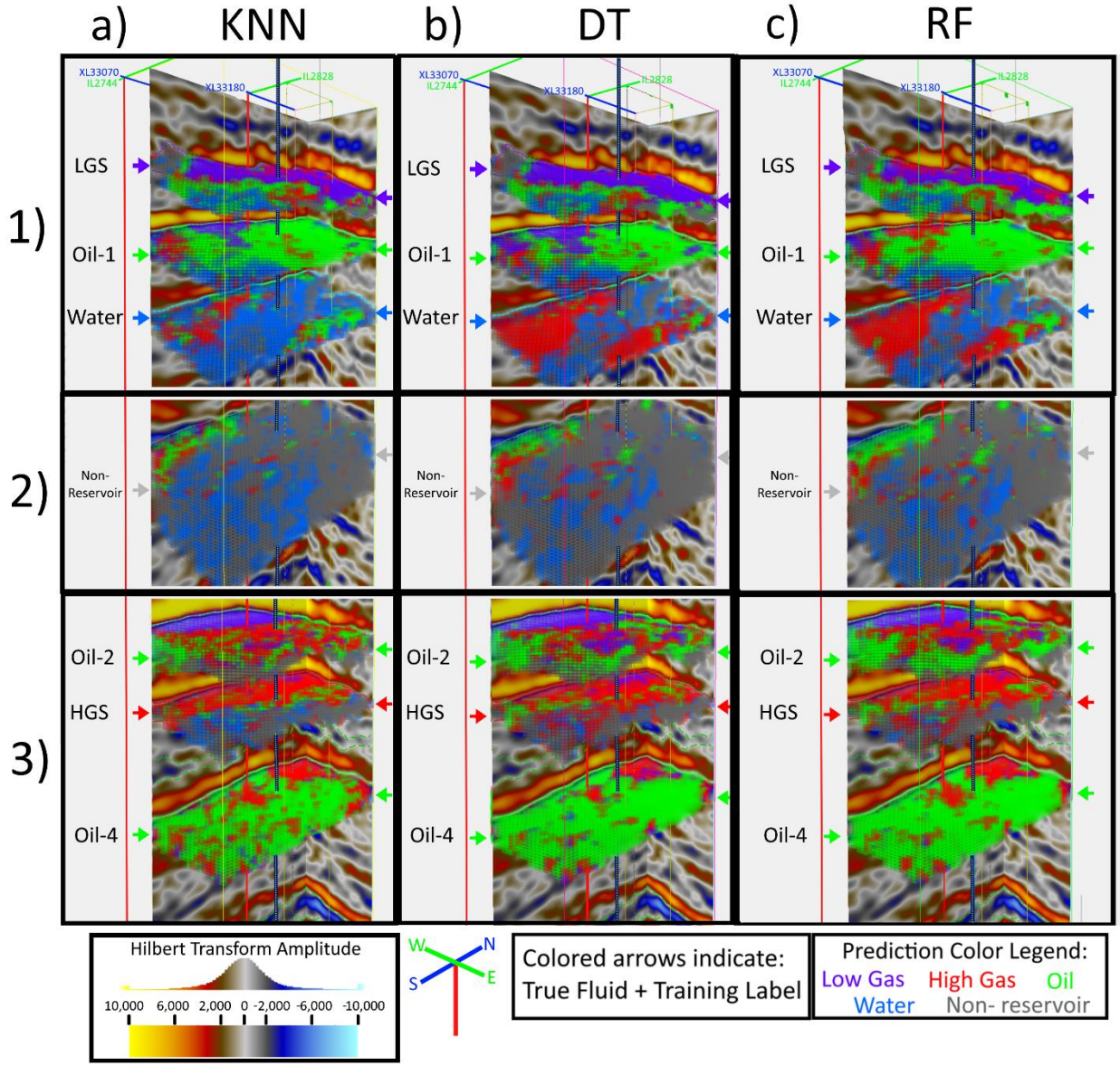

Figure 2-13: 3D view of the predictions from the Ursa expanded blind. The Hilbert transform of the seismic volume with inline 2924 and crossline 33140 are shown in the background to frame the predictions' results better. The top row (1) presents the LGS, Oil-1, and water reservoirs located at around 12,000 ft SSD. The center row (2) presents the 100 ms thick shale section. The bottom row (3) presents the Oil-2, HGS, and Oil-4 reservoirs located at around 18,500 ft SSD. **a)** K-nearest neighbors model predictions. **b)** Decision tree model predictions. **c)** Random forest model predictions.

Arbitrary line and horizon map of models' predictions in the KKLA validation volume

The results of the predictions of the three models in the KKLA volume (KKN top row, DT middle row, and RF bottom row) are presented in an arbitrary line cross-section passing through wells A-D in Figure 2-14 and map view in Figure 2-15. The KNN predictions in Figure 2-14a stand out from DT and RF predictions as they seem to lack meaningful classification of HGS in the target horizon, although minor traces of HGS are seen in Well A and Well B of the King Kong Field. The lack of HGS predictions in the reservoir becomes more concerning when multiple isolated voxels classified as HGS are observed in the upper part of the volume. The oil classifications from the KNN model, although present in higher quantities than expected, are only found within the reservoirs and are not being predicted elsewhere.

The DT (Figure 2-14b) and RF (Figure 2-14c) predictions are very similar. Both exhibit the correct fluid predictions for wells A through C, and debatably correct predictions for Well D. The true fluids encountered at Well A were a combination of oil and HGS, which DT and RF models successfully predict. Both models show a concentration of HGS and oil predictions at the crest of the King Kong structure. Both models show a smooth transition into LGS predictions down-dip. This LGS prediction occurs further east of the crest of the structure and coincides with the location of Well B, which was reported as a LGS well. These LGS predictions are considered a correct classification for the DT and RF models. A noticeable difference in the models is the extent of the LGS prediction, which is larger in the DT model. An important observation is the outline of oil classifications that occur roughly up to 50 ms above the King Kong reservoir. This phenomenon is more pronounced in the RF model than the DT model, and an interpretation of their existence is described in the discussion section of this research.

The classification results at the location of Well C are observed as a large homogeneous mass of oil voxels that span the entire length of the isolated reservoir for both the DT and RF models. This prediction is considered a successful classification because Well C was reported as producing only oil with no documented gas production. The prediction results at the location of Well D in the Lisa Anne Field were less successful as there is no classification of LGS as expected from the well history. The DT and RF models show classifications of non-reservoir along the Well D path. On the western side of the field, we see heterogeneous and isolated voxel predictions of oil and HGS that are considerably less defined compared to the predictions at the other wells. The practicality of the results at Well D could be argued since a well should not be drilled at a location predicted as non-reservoir or with an ambiguous classification of oil and HGS. The aerial extent of all the fluid predictions within the reservoir is observed on a map view in Figure 2-15.

The horizon of predictions from the center of the reservoir is presented in Figure 2-15, superimposed to colored structure contours and the original most negative amplitude with a grayscale color bar. As seen in the arbitrary line of Figure 2-14, the KNN model overpredicts oil and only predicts HGS outside of the high amplitude areas. As in the cross-section of Figure 2-14, predictions from the DT and RF models are nearly identical in Figure 2-15. Both the DT and RF models successfully predict a concentrated area of LGS at the location of Well B, and a mixture of HGS and oil predictions further up-dip at the location of Well A. The isolated reservoir amplitude of Well C is successfully predicted as pure oil with no trace of single voxel gas predictions from the DT and RF models.

The successful prediction of fluids in three out of four wells brings validity to the DT and RF ML models. Furthermore, the LGS Well D of the Lisa Anne Field shows faint oil and HGS predictions from the DT and RF models consistent with the well's uneconomical production.

Predictions of HGS and oil can be seen in two other undrilled high-amplitude areas of the King Kong and Lisa Anne Fields.

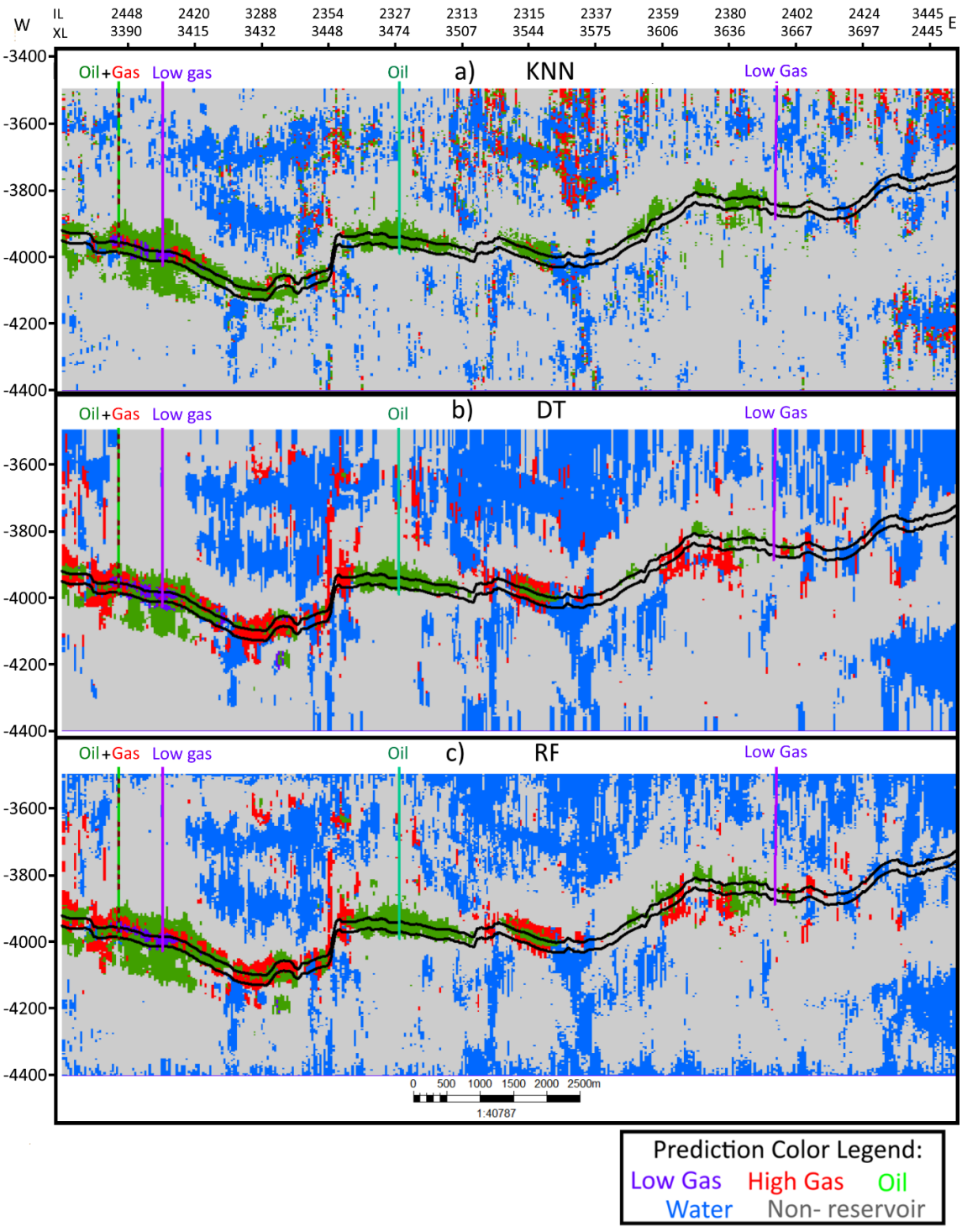

Figure 2-14: Arbitrary line cross-section passing through all the bright amplitude reflections extending from the King Kong field (west) to the Lisa Anne field (east), showing each model's color-coded prediction results. The black lines represent the top and base of the uppermost reservoir. The four wells in the area are presented with a color-coded well path representative of their production history. **a)** K-nearest neighbor model predictions. **b)** Decision tree model predictions. **c)** Random forest model predictions.

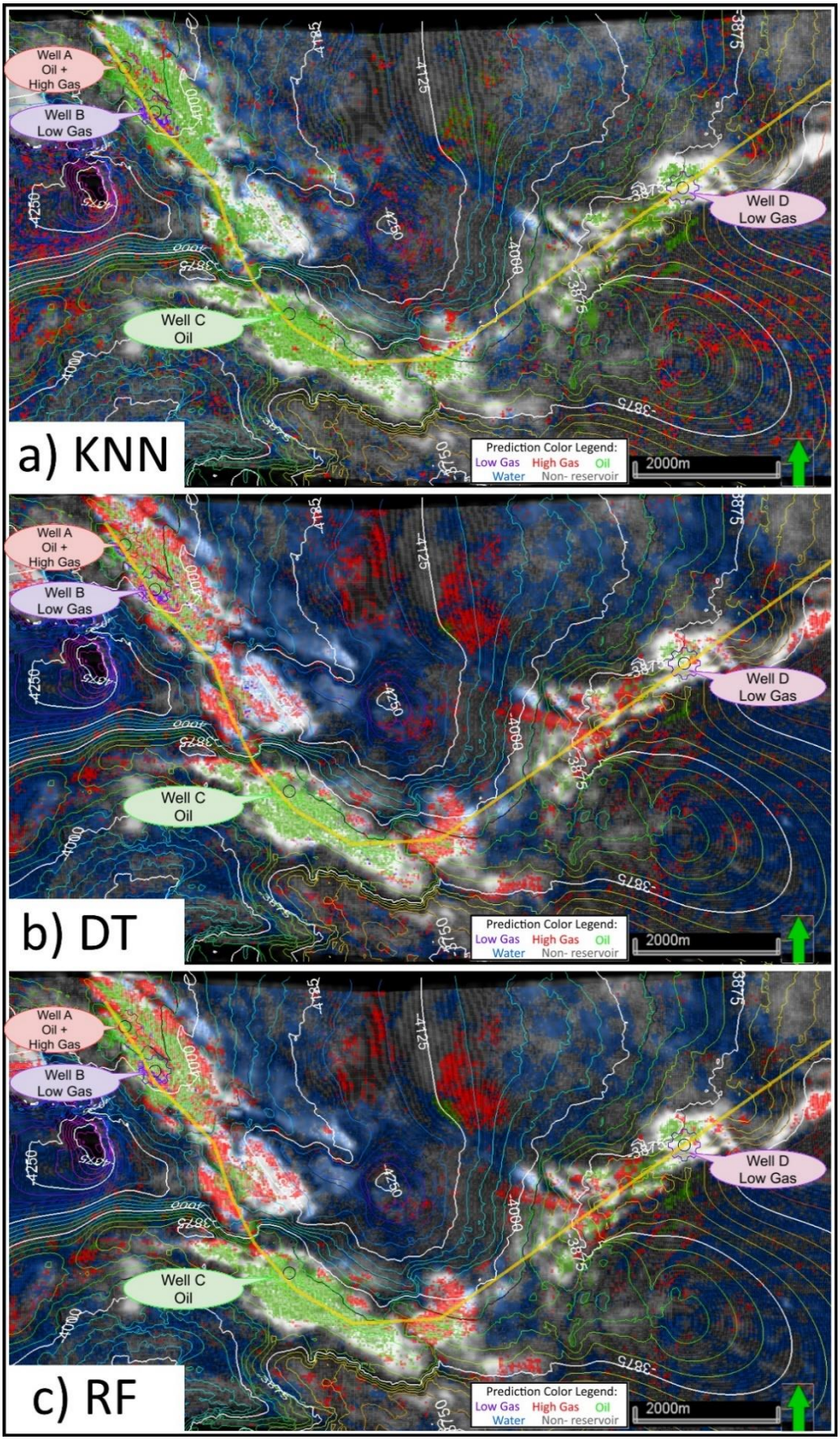

Figure 2-15: Horizon extraction of the ML model predictions in the KKLA survey. Voxels are color coded to the predictions for each model. Colored structure contours show time in ms. Most negative amplitude is shown in the background to highlight the locations of the bright spots as white. Wells A-D are labeled with their respective production history. The yellow line shows the location of the arbitrary line presented in Figure 2-13. **a)** K-nearest neighbor model predictions. **b)** Decision tree model predictions. **c)** Random forest model predictions.

DISCUSSION

The presented results show the success of implementing supervised machine learning models to aid in identifying fluids within reservoirs. ML predictions observed in the Ursa Field detect lateral fluid transitions, including fluid flat spots not witnessed in the original seismic volume. The validation test in the KKLA dataset shows that correctly training a ML model with the correct frequency attributes can yield successful fluid classification without using data from the second dataset as part of the training. The training results, blind test, and validation test for each of the three models are presented with variable success for each of the three models. The following section will discuss the models' validity and the interpretations that led to the success or failure of each.

Grid-search cross-validation for hyperparameter selection and confusion matrix of KNN, DT, and RF for training volume

The summary chart in Figure 2-4 aids the interpretation of the advantages and pitfalls of the model training for each of the three algorithms. The number of hyperparameters and the final macro average accuracy show a high-level view of the time it takes to train each algorithm appropriately. The KNN model is straightforward, with one hyperparameter, while the DT and RF models took considerably longer to fine-tune by having multiple hyperparameters.

This analysis demonstrates that training accuracy is not necessarily correlated to the model's effectiveness when predicting in a different dataset. The KNN and RF models, although similar in training macro average accuracy, exhibited variable quality in their predictions in both the expanded Ursa volume blind test and the KKLA validation. The DT and RF models had a 20%

difference in training macro average accuracy; however, their results were nearly identical in the expanded Ursa volume blind test and the KKLA validation test.

The confusion matrix confirms the hypothesis that the frequency attribute suite effectively differentiates between hydrocarbon and non-hydrocarbon classes. The biggest concern is that most misclassifications lean towards overestimating oil in the training volume. This overestimation of oil can be attributed to 32% of the training data points being labeled as oil (Figure 2-3b). Thus, the models expect the oil class to exist in high concentrations throughout the volume. The overestimation of oil was higher when the training volume consisted of 44% oil-labeled data points (Figure 2-3a) before removing the two low-amplitude oil reservoirs. Future models could mitigate this risk by having a distinct "low-saturation oil" class that could add quantitative uncertainty to the oil predictions.

Random forest SHAP

The SHAP attribute importance chart in Figure 2-5 confirms many of the observations presented in Chapter 1. The frequencies observed to have the highest separation in value ranges for HGS and LGS (12 Hz -22 Hz) ranked higher in the importance chart, followed by the lower frequencies (4 Hz – 8 Hz) with slightly less importance. Although meaningful relationships were analyzed from the spectral shape attributes in Chapter 1, the RF model gave little importance to them when compared to the discrete frequency magnitudes. Observing the individual fluid classes (Figure 2-6) shows that the high magnitude of the lower frequencies is a distinguishing factor of the HGS class. This affinity for the lower frequencies is attributed to the higher bandwidth range

in higher gas saturation, which diminishes as the saturation decreases. Inversely, the LGS class is primarily identified with the high magnitude of the medium frequencies.

The interpretation that LGS produces more attenuation than HGS from Chapter 1 is accentuated by observing the SHAP importance chart of both fluid classes. The SHAP values further support this interpretation by highlighting that low skewness and kurtosis and high bandwidth values are defining factors for classifying HGS in the RF model. The opposite of those attribute values defined the LGS classification. Thereby strengthening the case that LGS produces more attenuation than HGS.

The SHAP values also provide deeper insight into how to use the entire frequency spectrum and their spectral shape attributes to aid in identifying oil and water in reservoirs. SHAP values showed that high magnitudes of frequencies higher than 30 Hz could differentiate the presence of oil from other reservoir fluids. Compared to gas, the density of oil should produce less attenuating effects of the higher frequencies. Therefore, the higher frequency range can help with the differentiation of oil and gas without the use of AVO methods. The SHAP values also confirm that roughness and slope can significantly help identify water presence in anomalous high-amplitude reservoirs that lack oil or gas. High slope and roughness in the water reservoirs are interpreted to have highly variable frequency magnitudes across a large bandwidth of frequencies, which is expected of amplitudes lacking attenuation. Analyzing spectral shape attributes to interpret the frequency spectrum of each voxel in the reservoir exhibits potential as supporting attributes for fluid identification, especially when using ML algorithms that are sensitive to minor differences.

Ursa expanded blind test

Observing the results of the Ursa expanded volume blind test in Figures 2-10 and 2-12 helped to distinguish the model's reliability for each algorithm. It needs to be considered that there is no ground truth for the fluids in the reservoir located away from the borehole. The expected result is that most of the voxels in each reservoir will be classified as the same fluid class used for the training, in which all three models succeeded. The remaining predictions incongruent with the fluid class during training can be interpreted in various ways. The predicted classification can change depending on fluid differences, geological variability, or seismic noise.

Problems related to seismic noise are possibly the most pronounced in the KNN model's prediction due to the single voxel classifications that produce less homogeneous results than the DT and RF models (Figure 2-11). These abrupt changes are likely seismic noise that affects the attribute values and, subsequently, the classification of that voxel. The KNN algorithm is more likely to be affected because it gives equal importance to all attributes used, and a significant change in one can change the classification.

Changes in geology or fluid are expected to change the classification of an area at a discrete vertical or horizontal boundary, respectively. A distinct horizontal boundary is seen in the LGS reservoir, easily observed in the DT and RF model predictions (Figure 2-12). Having LGS over oil is consistent with the densities of the fluids. This observable flat spot of gas-oil contact occurs in an extensive area 600 feet east of Ursa Well #1, which would not have been observed in well logs or production data. Although the seismic volume is in time, the shallower part of the volume over the area of interest is uniform. No drastic velocity changes are expected to deform the time structures. No other explanation can be attributed to such a sharp, flat change in the predictions of the voxels. The evidence suggests that this is an actual oil-gas flat spot contact. This

flat spot in the LGS reservoir cannot be observed at the regular seismic resolution and highlights that multi-attribute machine learning analysis can enhance the seismic data's resolution, similar to inversion methods. All the other reservoirs show multiple fluids predicted in each, and all exhibit gas patches that lay over the oil (Figures 2-11 and 2-12). The absence of any observed errors in layers of higher-density fluids above lower-density ones, such as water over oil, indicates that the models accurately distinguish between different fluids below the reservoir scale.

In Figures 2-10 and 2-12, there was a consistent classification of non-reservoir at the western extent of the bottom set of reservoirs. All those predictions are interpreted to represent the salt dome at the flank of the Ursa Field. The bright amplitudes just slightly east of the salt in the Oil-2 reservoir are classified as LGS. One limitation of this research is that no well is present to validate the true fluid class present at that bright spot. This research interprets the bright amplitude as the salt contact due to a high increase in the reflector's dip caused by a velocity pull-up. The results suggest that the models might not be sufficiently trained to differentiate salt contact high amplitudes from hydrocarbon bright amplitudes correctly. Interpreting the lateral extent of salt bodies is a recurrent problem in the geophysics field. The results in this research lack sufficient evidence to suggest that the presented methodology can solve that problem. Despite this, the fluid prediction models are validated with the results in the KKLA volume.

KKLA validation volume

The predictions in KKLA volume (Figures 2-14 and 2-15) serve as a more comprehensive test of the models due to the availability of four wells that present production data containing our five fluid classes studied. The KNN model was quickly invalidated due to the over-prediction of

the oil class. This oil class overestimation is interpreted to be caused by the attribute variability of the KKLA dataset compared to the Ursa dataset. The KNN algorithm is less complex and was interpreted to be more affected by noise from the results in the Ursa dataset. This problem would be magnified once a new dataset is introduced for predictions. The KNN model is also likely being affected by using a large set of attributes, which we previously discussed that one attribute could highly affect the classification. This interpretation suggests that although the KNN algorithm is effective for fluid identification when trained and used in a single dataset, using it in two different datasets would lead to inaccurate identifications of fluids.

The correct results of the DT and RF models in three out of four wells validate the effectiveness of ML in predicting fluid classes and, more remarkably, their ability to predict correctly in a different dataset that is not used for the training of the models. The lower macro average accuracy score of the DT model did not seem to affect the results in the KKLA dataset when compared to the RF model.

The author believes the DT model performed marginally better than the RF model based on a couple of observations. The DT model predicted a more extensive area of HGS in Well A, LGS in Well B, and less oil and HGS prediction in Well D. The DT model also showed a lower height in the erroneous oil predictions that occurred 50 ms above the King Kong Field. The independent frequency magnitude volumes likely cause this erroneous prediction. Spectral decompositions methods are not perfect, and vertical smearing of energy occurs during the attribute creation prosses. The vertical smear of the energy implies a mixture of discrete frequency magnitude attributes with high enough values directly above the reservoirs, leading to the erroneous prediction of oil instead of the correct prediction of non-reservoir. These observations suggest that the DT model is more capable of compensating for this error than the RF model. These

further emphasize the need to limit predictions to the reservoir interval or create prediction maps at the reservoir interval to aid in interpreting the predictions.

The results at Well D stand out as the only well that did not have a correct prediction in the DT and RF model. The training of the models only included a LGS reservoir with extremely high amplitudes. This lack of a low amplitude LGS reservoir during the training suggests that the model can only correctly identify LGS when the amplitudes are high (like in Well B) but fail when the amplitudes are dimmer (Well D). The DT and RF models showed mild success by identifying Well D as non-reservoir with traces of oil and gas. In practice, a non-economical reservoir classified as non-reservoir or hydrocarbon class traces would still be beneficial during the risking of the prospect.

Although the validation of the models is qualitative, based on the size and distribution of the fluid class prediction around each well, quantitative results can be estimated using the RF model. The use of probability volumes for a particular fluid class can be used to determine the likelihood of a particular class prediction against the other classes. These volumes would add a quantifiable value to aid in the interpretation of the associated risk when compared to other reservoirs in the exploration stageCONCLUSION

Successful identification of reservoir fluids and gas saturations is possible using spectral shape attributes and independent frequency magnitudes as inputs for training in a supervised machine learning model. Although similar results can be obtained with AVO, supervised machine learning is successful without needing a pre-stack seismic dataset. This finding is significant for research and exploration because post-stack data is the most widely available seismic data type.

The three algorithms have different reliability depending on whether the predictions are performed in the same or different dataset as the training. All three algorithms also require varying amounts of time to train a successful model. The KNN algorithm is a simple model to train and performs excellently during training but tends to have isolated voxel predictions in the Ursa

expanded volume blind test, which obscures the results. The fluid prediction results still show high reliability, and it could be used as a first-pass model if used in the same dataset used for the training. The results of the KNN model in the KKLA volume suggest that KNN is not suited for the transfer learning task. Further tests should be performed with fewer attributes to confirm the hypothesis that KNN is better used with a limited number of input features.

The DT algorithm followed in increasing complexity, and it was challenging to achieve high accuracy scores during the training that did not overfit. The hypothesis that it would be the least effective at fluid characterization was disproven upon observing the results in the Ursa expanded volume blind test and the KKLA validation volume. It had nearly identical results in the blind test and validation as the RF model and arguably better since it had a higher volume of correct prediction for the gas saturations in Wells A and B. Validation testing of the model would be recommended to avoid spending time with the training accuracy as they did not seem to affect the results. Overall, the DT model was successful at the fluid identification task and showed high potential for future research.

The RF model is the most complex to train, requiring an extra hyperparameter set to control the bagging. Despite being nearly equally effective at fluid identification as the DT model, this research suggests being used in every scenario. Using SHAP to quantify attribute importance can serve during the initial stages to reduce attributes that contribute the least to the final predictions. The use of SHAP in this research was also helpful in understanding which attributes help in identifying each fluid class and substantiated many interpretations presented in Chapter 1.

In conclusion, using supervised machine learning models, specifically the KNN, DT, and RF algorithms, for reservoir fluid identification and saturation prediction shows promising results. Spectral shape attributes and independent frequency magnitudes proved to be effective inputs for

training these models. While the KNN algorithm is simple and performs well during training, it is unsuitable for transfer learning processes. The DT algorithm is very effective and has nearly identical results to the RF model. The RF model is recommended for use in every scenario due to its ability to use SHAP to quantify attribute importance, despite being the most complex to train. The success of the DT and RF model with the limitation of one training well and post-stack data proves machine learning can provide meaningful results with limited datasets. Overall, the methodology can be easily adapted to any basin and quantity of training data available to provide valuable insights for future studies in reservoir fluid characterization and prospect risking.

ACKNOWLEDGMENTS

would like to reiterate my appreciation to AASPI, Python and SLB for their invaluable tools used throughout my research project. In addition, I would also like to thank scikit-learn for their machine learning library, which has been integral to the development of predictive models in my research. The scikit-learn library has provided me with a comprehensive set of tools for machine learning tasks, including data preprocessing, feature selection, and model evaluation. Without the scikit-learn library, my research would not have been possible.

REFERENCES

Breiman, Leo. "Bagging Predictors." *Machine Learning* 24, no. 2 (August 1996): 123–40. https://doi.org/10.1007/BF00058655.

Chenin, Julian, and Heather Bedle. "Unsupervised Machine Learning, Multi-Attribute Analysis for Identifying Low Saturation Gas Reservoirs within the Deepwater Gulf of Mexico, and Offshore Australia." *Geosciences* 12, no. 3 (March 14, 2022): 132. https://doi.org/10.3390/geosciences12030132.

Elshahawi, Hani. "Deepwater Exploration and Production in the Gulf of Mexico - Challenges and Opportunities." *Petrophysics - The SPWLA Journal of Formation Evaluation and Reservoir Description* 55, no. 02 (April 1, 2014): 81–87.

Fix, Evelyn; Hodges, Joseph L. (1951). "Discriminatory Analysis. Nonparametric Discrimination: Consistency Properties" (PDF) (Report). USAF School of Aviation Medicine, Randolph Field, Texas. Archived (PDF) from the original on September 26, 2020.

Galloway, William E. "Chapter 15 Depositional Evolution of the Gulf of Mexico Sedimentary Basin." In *Sedimentary Basins of the World*, 5:505–49. Elsevier, 2008. https://doi.org/10.1016/S1874-5997(08)00015-4.

La Marca, Karelia, and Heather Bedle. "Deepwater Seismic Facies and Architectural Element Interpretation Aided with Unsupervised Machine Learning Techniques: Taranaki Basin, New Zealand." *Marine and Petroleum Geology* 136 (February 2022): 105427. https://doi.org/10.1016/j.marpetgeo.2021.105427.

Lubo-Robles, David, Thang Ha, Sivaramakrishnan Lakshmivarahan, Kurt J. Marfurt, and Matthew J. Pranter. "Exhaustive Probabilistic Neural Network for Attribute Selection and Supervised Seismic Facies Classification." *Interpretation* 9, no. 2 (May 1, 2021): T421–41. https://doi.org/10.1190/INT-2020-0102.1.

Manning, Christopher D., Prabhakar Raghavan, H Hinrich Schütze, "Introduction to Information Retrieval", 2008.

Morgan, James N., and John A. Sonquist. "Problems in the Analysis of Survey Data, and a Proposal." *Journal of the American Statistical Association* 58, no. 302 (June 1963): 415–34. https://doi.org/10.1080/01621459.1963.10500855.

O'Brien, John. "Seismic Amplitudes from Low Gas Saturation Sands." *The Leading Edge* 23, no. 12 (December 2004): 1236–43. https://doi.org/10.1190/leedff.23.1236_1.

Pedregosa, Fabian, Gaël Varoquaux, Alexandre Gramfort, Vincent Michel, Bertrand Thirion, Olivier Grisel, Mathieu Blondel, et al. "Scikit-Learn: Machine Learning in Python." Journal of Machine Learning Research 12, no. 85 (2011): 2825–30.

Shapley, L. S., 1951, "Notes on the N-person Game": Rand Corporation.

APPENDIX

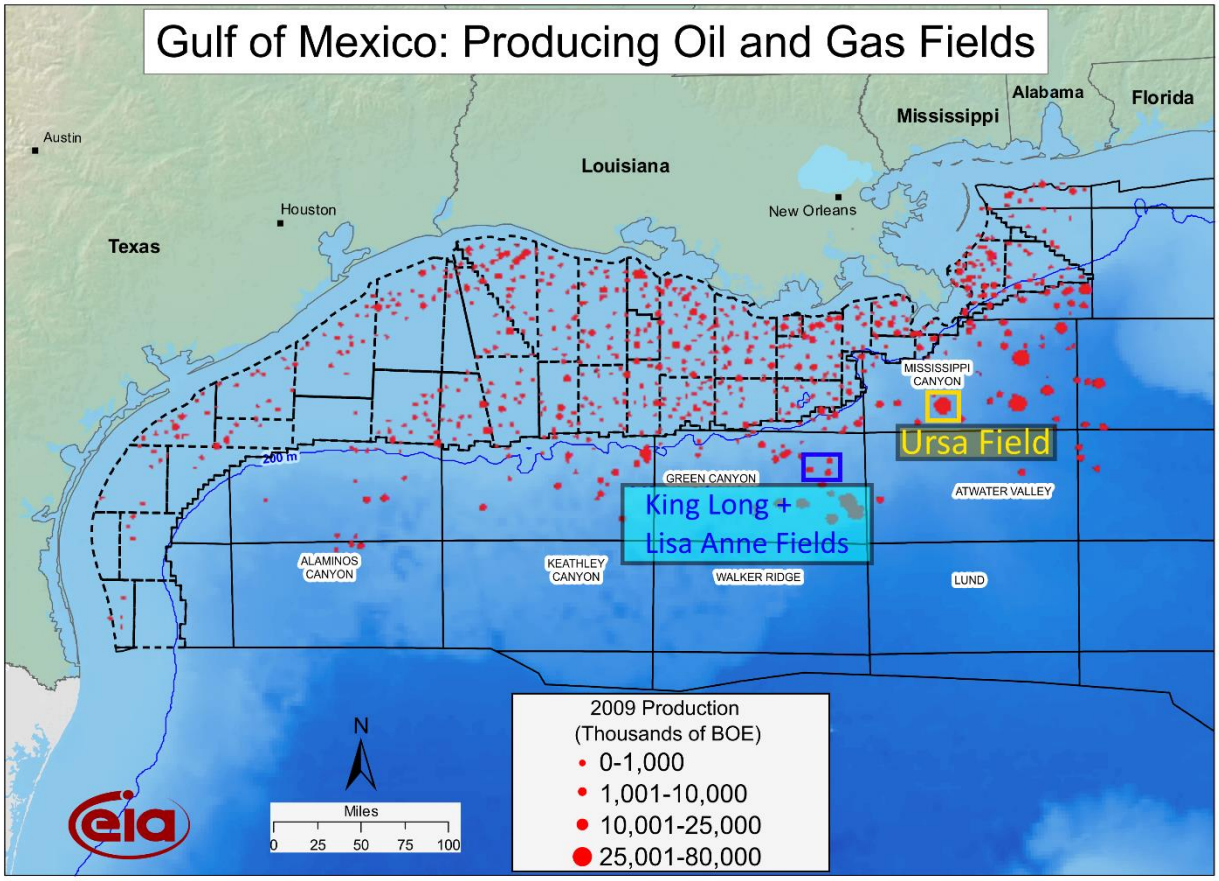

Source: Energy Information Administration based on data from MMS, HPDI, CA Dept of Oil , Gas & Geothermal
Updated: April 8, 2009

Appendix, Figure 2-1: Gulf of Mexico cumulative production map. The yellow box indicates the location of the Ursa Field and Survey, blue box indicates the locations of the King Kong and Lisa Anne Fields and survey. Modified from U.S Energy Information Administration and Elshahawi, 2014.

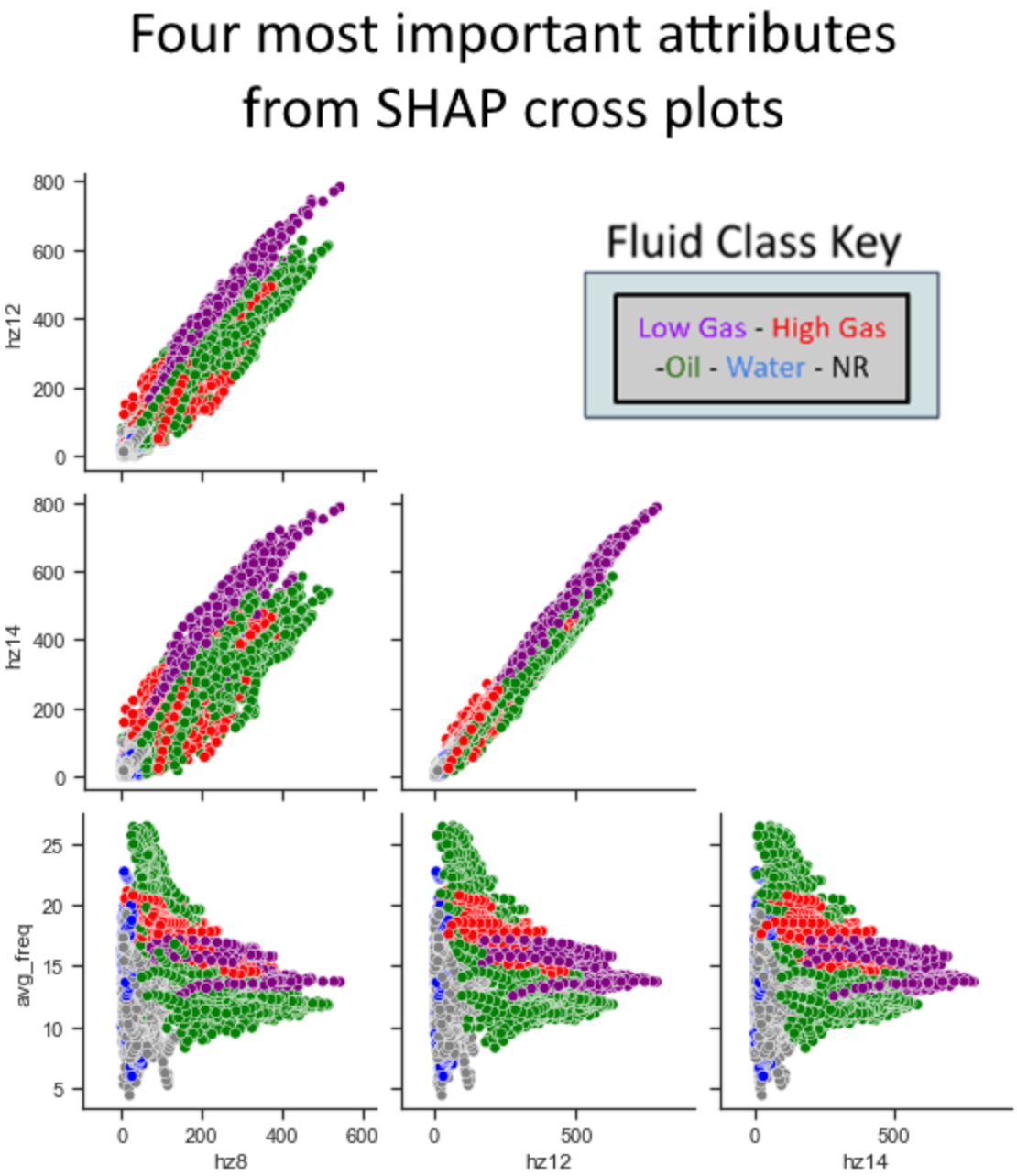

Appendix, Figure 2-2: Cross-plot matrix of the four most important attributes as rated by the SHAP values in Figure 2-5. Horizontal and vertical axes show the full range of values for the two attributes used in each plot. Fluid class colored-coded data points values are present in each cross plot.

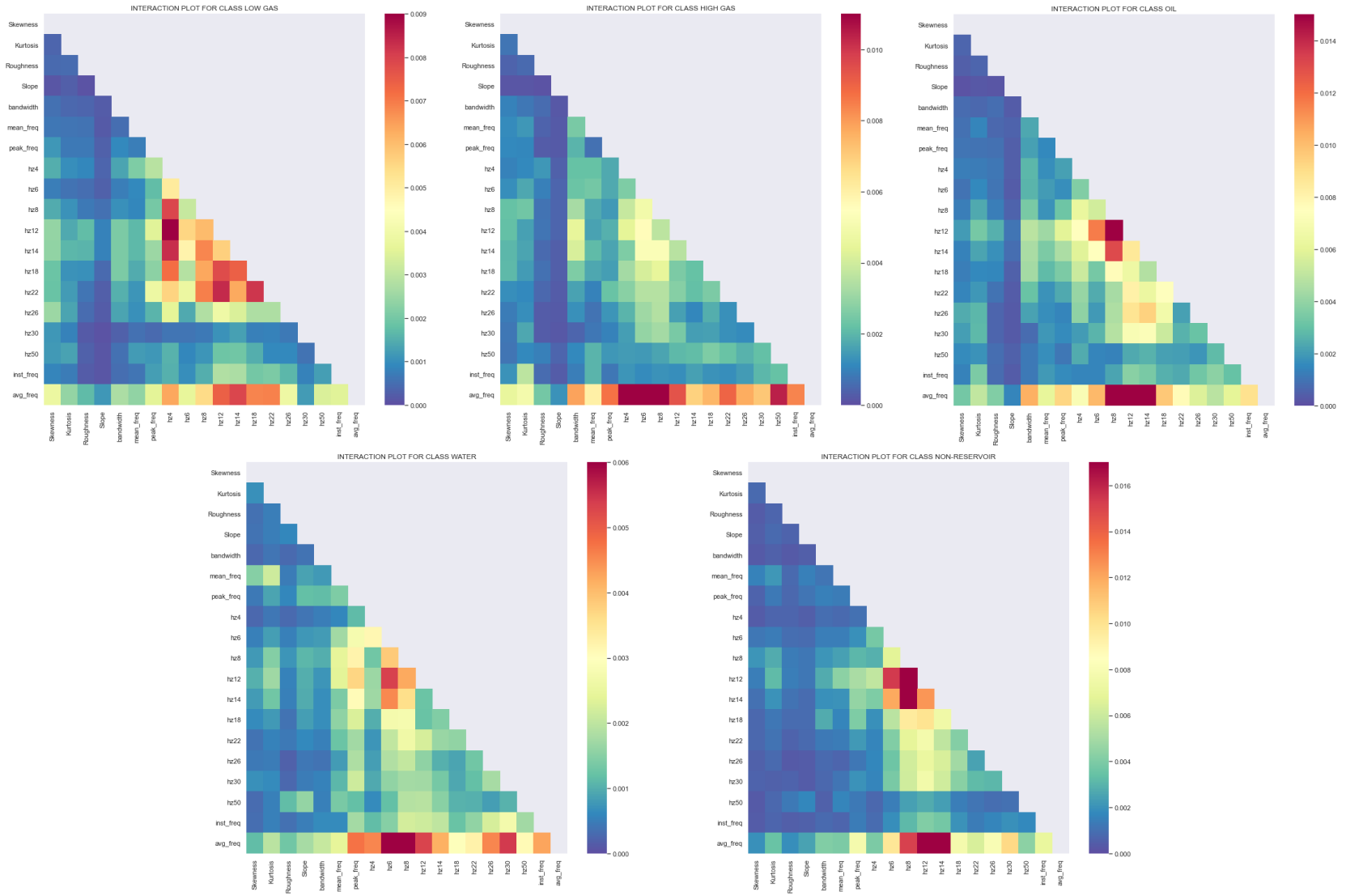

Appendix, Figure 2-3: Mean SHAP interaction value matrices for the five fluid classes. SHAP interaction values measure the contribution of two features to the prediction made by the random forest model. Warm colors indicate the highest interaction while cool colors denote the lowest interaction. The four highest interactions for each fluid class are shown in Appendix Figure 2-4 as partial dependence plots.

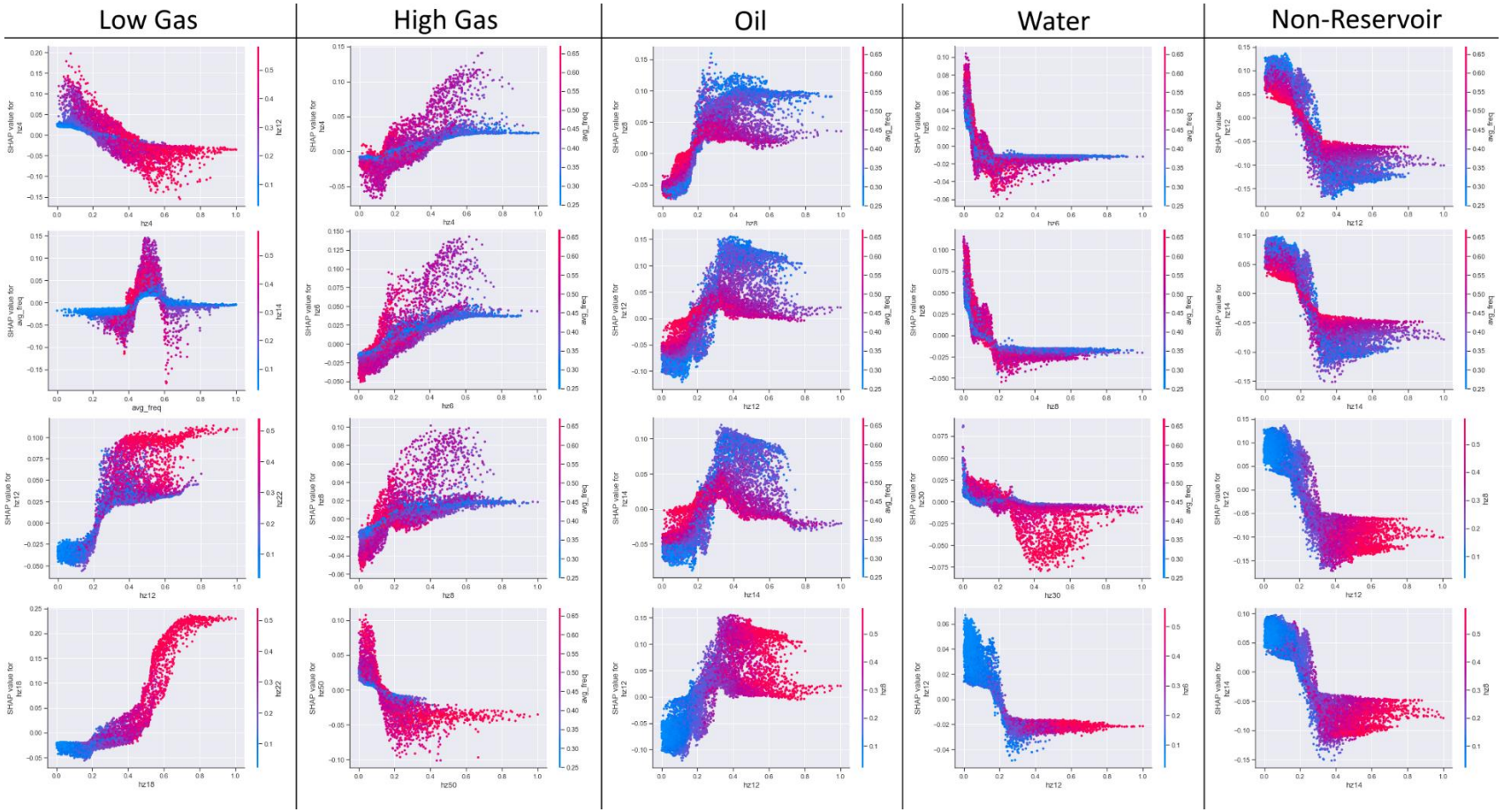

Appendix, Figure 2-3: Partial dependence plots for the four highest SHAP interaction values for each fluid class. The partial dependence plots show the effect of a feature on the predicted outcome of the random forest model while holding all other features at a constant value. The plot is created by varying the value of one feature over its range and calculating the predicted outcome of the model at each point. The resulting plot shows how the predicted outcome changes as the value of the feature changes while holding all other features constant. The attribute on the vertical and horizontal axis is the feature held constant, with the horizontal axis representing the scaled attribute values and the vertical axis plotting the SHAP values. The added benefit of this plot is that the color represents the scaled values of a second attribute with which the first attribute has high interaction.